

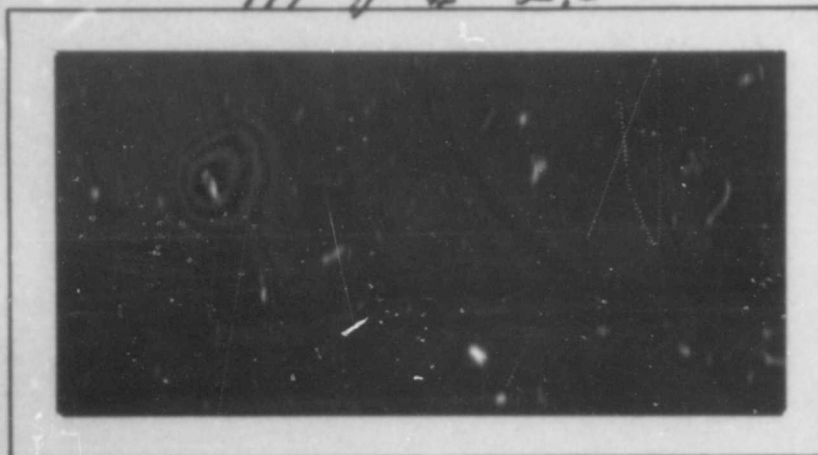
600730

# AIR FORCE INSTITUTE OF TECHNOLOGY



AIR UNIVERSITY  
UNITED STATES AIR FORCE

*111-P # 2.50*



## SCHOOL OF ENGINEERING

WRIGHT-PATTERSON AIR FORCE BASE, OHIO

DDC  
RECEIVED  
JUN 5 1964  
TISIA E

AN INVESTIGATION OF A  
LASER/INTERFEROMETER  
ATTITUDE MONITORING DEVICE

Capt. Henry A. Olender, USAF

GE/EE/62-17

**BLANK PAGE**

AN INVESTIGATION OF A  
LASER/INTERFEROMETER  
ATTITUDE MONITORING DEVICE

THESIS

presented to the Faculty of the School of Engineering of  
The Air Force Institute of Technology  
Air University  
in Partial Fulfillment of the  
Requirements for the  
Master of Science Degree  
in Electrical Engineering

by

Henry Adam Olender, BAE

Captain USAF

GE 62

December 1962

Acknowledgements

The author wishes to express his appreciation to Prof. Jerzy Lubelfeld, faculty thesis advisor, for his guidance and encouragement during the course of this investigation. He also wishes to thank the personnel of the Advanced Methods Branch of the Guidance and Control Division at Holloman AFB for their assistance in completing the work required for this investigation. In particular Capt. Mackey J. Real, Jr., thesis sponsor and project officer on Project 5177-14, Laser Calibration Techniques, under which this work was done, was most helpful in the conception and analysis of the angle sensing interferometer.

Acknowledgement is also made to Dr. Paul D. Jose of the Office of Research Analyses, OAR, for his invaluable guidance and assistance.

The author wishes to thank Pat Friel who typed this thesis for her fine work and assistance in working out the format of this report.

Special appreciation is expressed to his wife, Margaret, for her forbearance during the course of this work which required many hours away, either physically or mentally, from her and from their son, Eric.

Contents

	Page
Acknowledgements . . . . .	ii
List of Figures. . . . .	v
List of Tables . . . . .	vii
Abstract . . . . .	viii
I. Introduction . . . . .	1
II. The Attitude Monitoring Problem . . . . .	2
Scope of Investigation . . . . .	5
Alternate Angle Sensing Techniques . . . . .	5
Roll Axis Polarization Sensor . . . . .	7
Pitch/Yaw Refractosyn Sensor . . . . .	8
Pitch/Yaw Interferometer Sensor . . . . .	10
Comparison of Angle Sensing Techniques . . . . .	12
III. Theoretical Aspects of the Angle Sensing Interferometer . . . . .	15
Beam Divergence, Surface Flatness and Parallelism . . . . .	15
Optical Path Difference. . . . .	18
Angular Sensitivity . . . . .	22
Beam Separation . . . . .	24
Beam Reflection and Transmission . . . . .	27
Interference Intensity . . . . .	28
Maximum Range Considerations. . . . .	32
Combined Pitch and Yaw Effects . . . . .	35
Direction Sensing . . . . .	38
Angle Sensing Interferometer Design . . . . .	40
IV. Experimental Investigation of an Angle Sensing Interferometer. . . . .	49
Experimental Approach . . . . .	49
Description of Apparatus . . . . .	49
Laser Light Source . . . . .	49
Rotation Platform . . . . .	51
Autocollimating Telescope . . . . .	53
Interferometers . . . . .	53
Optical Sensor . . . . .	59

Contents

	Page
Experimental Setup . . . . .	60
Experimental Technique . . . . .	64
Experimental Results . . . . .	69
Interference Pattern . . . . .	70
Interference Intensity Signal . . . . .	70
Fringe Shift Effect . . . . .	72
Calibration Results . . . . .	77
Sensitivity Results . . . . .	80
V. Summary of Results and Conclusions . . . . .	83
VI. Recommendations for Continued Research . . . . .	86
Bibliography . . . . .	87
Appendix A: Derivation of Refractosyn Equations . . . . .	88
Appendix B: Derivation of Interferometer Equations . . . . .	93
Appendix C: Derivation of Interference Intensity Equations . . . . .	98
Vita . . . . .	101

List of Figures

Figure	Page
1 Track Curvature . . . . .	3
2 Polarization Sensor System . . . . .	7
3 Refractosyn Sensor Schematic . . . . .	9
4 Plane-Parallel Interferometer . . . . .	11
5 Range-Sensitivity Curves . . . . .	13
6 Optical Path Geometry . . . . .	19
7 Fringe Count Versus Angle . . . . .	20
8 Sensitivity Versus Angle . . . . .	24
9 Beam Separation Schematic . . . . .	25
10 Interferometer Gap/Angle Trade-Off . . . . .	26
11 Interfering Ray Components . . . . .	29
12 Intensity Versus Distance . . . . .	34
13 Pitch/Yaw Angle Schematic . . . . .	36
14 Direction Reversal Effect on a Sinusoidal Signal . . . . .	39
15 Theoretical Angle Sensing Interferometer Design. . . . .	42
16 Quarter Wave Retarding Plate Position . . . . .	47
17 Helium-Neon Laser. . . . .	50
18 Spectrometer Rotation Table and Autocollimating Telescope .	52
19 Solid Gap Interferometer . . . . .	55
20 Air Gap Interferometer (Wood Construction). . . . .	57
21 Air Gap Interferometer (Aluminum Construction). . . . .	58
22 Experimental Setup Schematic . . . . .	60
23 Test Apparatus . . . . .	62
24 Overall View of Experimental Setup. . . . .	63

List of Figures

Figure		Page
25	Normal Incidence Interference/Intensity Trace . . . . .	67
26	Interference Signal Traces . . . . .	71
27	Near Normal Incidence Traces . . . . .	73
28	Refractosyn Schematic . . . . .	89
29	Ray Path Through Refractosyn . . . . .	89
30	Ray Path Geometry . . . . .	94

List of Tables

Table		Page
I	Interferometer Design Specifications . . . . .	48
II	Calibration Results . . . . .	78
III	Corrected Calibration Results . . . . .	81
IV	Sensitivity Results . . . . .	82

Abstract

A laser beam referenced, Fabry-Perot type, angle sensing interferometer for precise inertial platform attitude monitoring was designed, analyzed and tested. Analysis indicated an angular sensitivity of 0.1758 fringes per arc second with an estimated accuracy of  $\pm 0.285$  arc seconds. The non-optimized device tested was satisfactory with respect to full field interference quality and signal characteristics. Angular sensitivity data showed good agreement with theory. Calibration data deviations from theory were greater than the estimated experimental accuracy. The probable cause of the poor agreement was the phase shift effect observed but not investigated. Several possible causes of this effect were discussed.

AN INVESTIGATION OF A  
LASER/INTERFEROMETER  
ATTITUDE MONITORING DEVICE

I. Introduction

The research work reported herein was concurrently done in support of Air Force Project 5177-14, Laser Calibration Techniques, and to fulfill my thesis research requirement. Project 5177-14 is concerned with the development of laser techniques for precise inertial platform attitude monitoring of rocket sled borne inertial guidance systems.

This thesis is concerned with the design, analysis, and testing of an angle sensing interferometer device using a coherent laser light beam as a reference, and having an accuracy significantly less than one arc sec. Such a device would be used in the inertial platform attitude monitoring application. This particular angle sensing application of the interference principle and the coherent nature of the laser beam has not been previously investigated to the knowledge of the author.

This report presents the results of this research and is organized in the following manner. First a discussion of the angle sensing problem is presented. Next various theoretical aspects of the angle sensing interferometer are presented and utilized in the analysis of an angle sensing interferometer design. Finally the experimental work is described and the results presented. After a summary of the results and conclusions, several topics for continued research are presented.

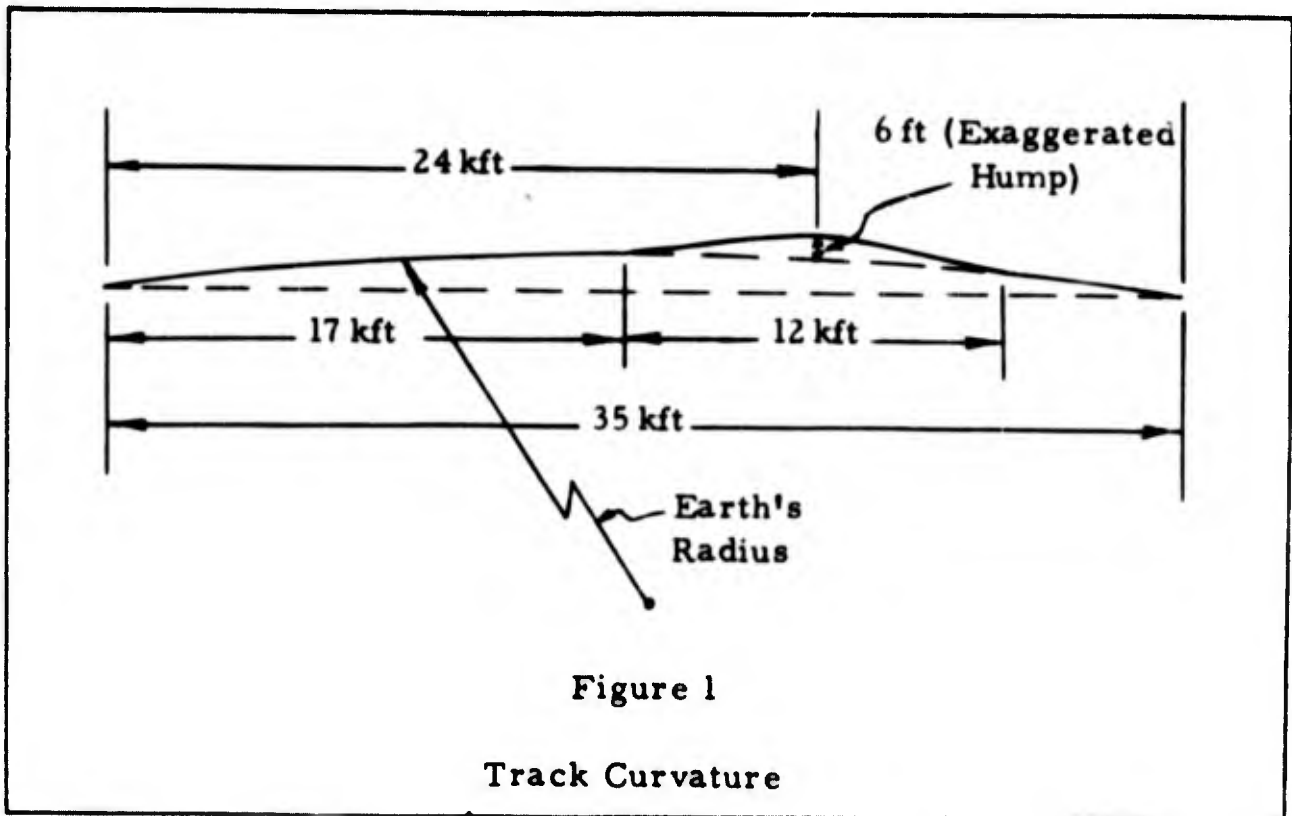
## II. The Attitude Monitoring Problem

One requirement of the inertial platform attitude monitoring application is that attitude changes be measured with respect to a prerun platform alignment with the local gravity vector. This essentially requires that all components of the sensing system which actually sense attitude variations (not necessarily those which may be required to sense reference intensities or to process the signal) be mounted on the inertial platform. This in turn, imposes size and weight limitations on the sensing apparatus. Other requirements are that the attitude be monitored continuously and all three axes be monitored simultaneously. Angular accuracy, range, and rate requirements are  $\pm 0.1$  arc sec.,  $\pm 5$  arc min., and up to 200 cps, respectively.

Continuous attitude information provided by such a system can then be utilized to test various advanced inertial guidance systems under acceleration conditions simulated with rocket sled runs. Other applications can be found wherever precise attitude alignment or attitude control is required.

The specification of accuracy to within  $\pm 0.1$  arc sec. is quite stringent. This requirement is based on the criterion of designing the test equipment to be one order of magnitude more accurate than the specified accuracy of systems to be tested. Since the accuracies of advanced inertial systems are on the order of  $\pm 1$  arc sec., at a minimum, sensors more accurate than  $\pm 1$  arc sec. will be required.

The track located at Holloman AFB is approximately 35 kft long. Typical sled runs cover from 20 to 30 kft of the track from start to finish. The track rails are parallel to within 0.015 inches and straight to within 0.03 inches in the earth's surface plane. However, in a



plane normal to the earth's surface and intersecting the center line of the track, the track generally follows the earth's curvature except for a hump described in Figure 1.

Because of the accuracy requirement optical methods of angle sensing will probably be required, and thus a light beam would be utilized as a reference. For continuous angle sensing the sensor must be within the light beam continuously throughout a typical sled run of up to 30 kft. One way of accomplishing this is to station the light beam so that it is coaxial with the path traversed by the sensor (i.e., centered on the track, at the proper height above the track, and parallel to the track). However, the earth's curvature and the hump in the track make it impossible for any light beam to be exactly parallel to the track and suggests the requirement for more than one light source to give complete coverage of the track.

Given a reference light beam, the atmosphere and earth's magnetic field act on the beam between the light source and the sled-borne sensor. Atmospheric effects will undoubtedly be aggravated due to thermal gradients and wind turbulence near the ground. Some of the possibly significant atmospheric effects are listed below.

1. Attenuation - primarily due to water vapor in the air
2. Scattering - due to particles in the air
3. Heat Shimmer - fluctuation of the air density close to the ground resulting from thermal differences and air currents which cause fluctuations in intensity of light received by the sensor.
4. Mirage Effect - the reflection and refraction of light in the atmosphere characteristic in high ambient temperature areas near the ground which cause a bending of the light beam.
5. Shock Waves - at speeds in excess of Mach 1, the extreme variations of air density across a shock cause a bending of the light beam.

The presence of the earth's magnetic field has an effect on polarized light known as the Faraday Effect. The Faraday Effect is a rotation of the plane of polarization of an electric field due to the presence of a magnetic field.

All or some of the above effects may introduce errors into any given angle sensing system unless their effects are calibrated or compensated.

### Scope of Investigation

The system outlined has four main areas of investigation associated with it.

1. Light source characteristics and light beam alignment, shaping, and positioning.
2. Effects of atmosphere and earth's magnetic field on transmitted light.
3. Design and development of angle sensing device
4. Signal processing.

The investigation of all of these areas covers a wide scope and would require a large effort and an extended period of time to accomplish. In order to limit the scope of this thesis research problem, the primary concern will be with the design, analysis and testing of the angle sensing device. An interferometric technique is suggested to achieve the accuracy required.

The objective of the research work reported below is to design and analyze an interferometer angle sensing device for the inertial guidance platform attitude monitoring application, and to perform laboratory tests to demonstrate the feasibility of such a device. The primary requirements are that the system have an angular accuracy significantly less than  $\pm 1$  arc sec., a range of  $\pm 5$  arc min. and a capability of measuring rates up to 200 cps.

### Alternate Angle Sensing Techniques

The characteristics of the light sources available can have a significant effect on the possible techniques of angle sensing which can be utilized. The development of the laser has made available a light

source having several unique properties. (Reference 6 is an excellent monograph on the laser field.) The laser light is monochromatic and spatially and temporally coherent to a degree not previously available. The light is also highly collimated or directional. One drawback is the fact that the continuous wave lasers presently available are limited in power output. For example, continuous lasers operate in the milliwatt to watt region while pulsed solid state lasers peak in the kilowatt to megawatt region (Ref 7 : 4). Conventional high power arc sources can operate at fairly high power but do not have the narrow frequency band, coherence and directional properties of the laser. The laser has a sort of " by-product" property which can be quite useful. This property is its plane polarization due to the Brewster angle windows used primarily to reduce transmission losses. Conventional light sources must utilize additional and external optics to produce polarized light. Although the continuous laser power output is restricted, its very low beam divergence partly compensates this disadvantage. Also, as in the case of any new art, it is almost certain that power outputs of continuous wave lasers will improve. The property of coherence is of special importance since it opens up the possibility of using interferometric techniques for angle sensing.

Due to the above considerations and the physical availability of a He-Ne laser, the laser was selected for use as a light source. The wavelength of this laser is  $6328 \text{ \AA}$ .

Initially three possible techniques of angle sensing were considered. One technique would be applicable to roll axis monitoring; the others, to either pitch or yaw axis monitoring. Each of these techniques will be described briefly and qualitative comparisons made between each.

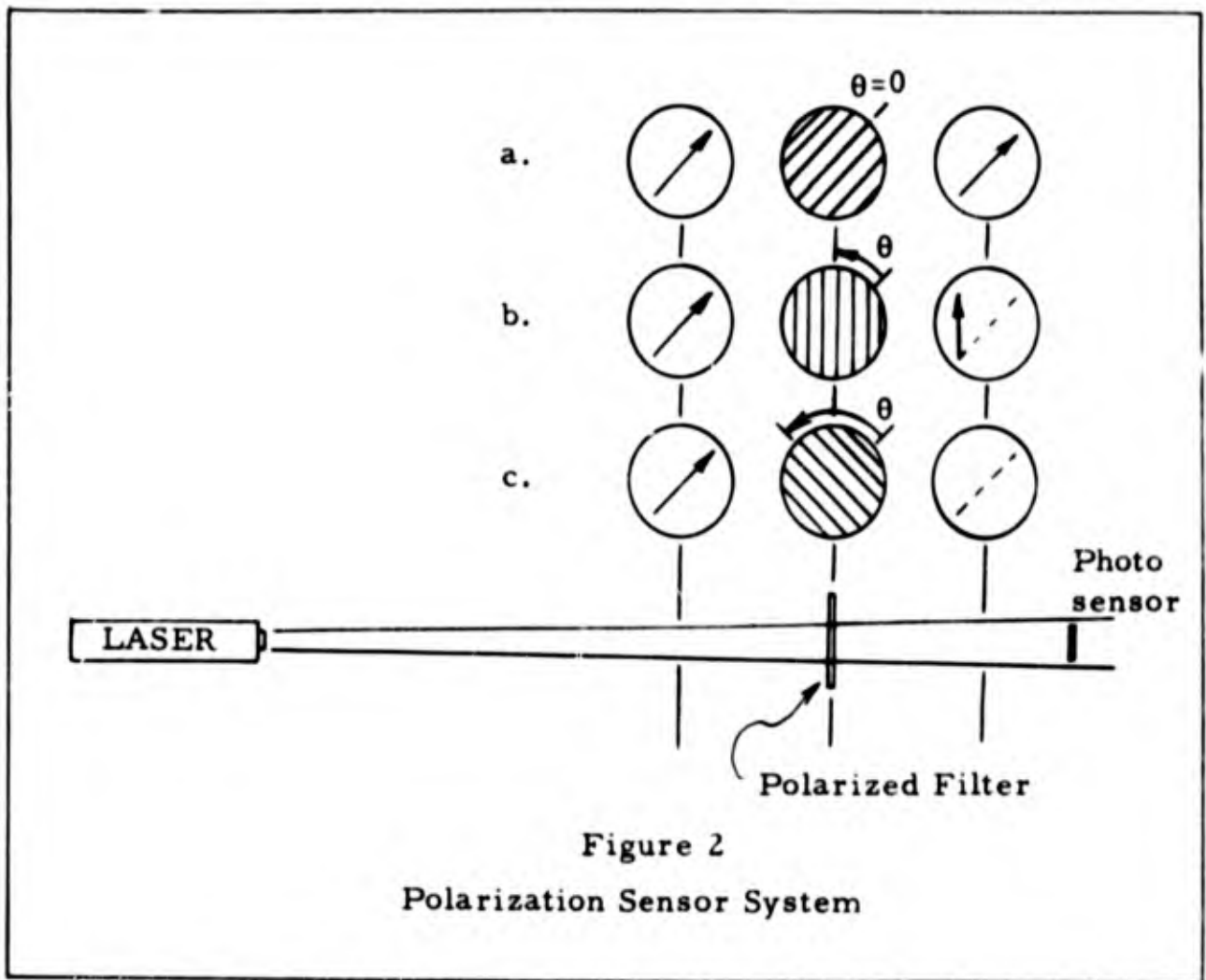


Figure 2  
Polarization Sensor System

Roll Axis Polarization Sensor. The first technique which will be discussed is a fairly simple and straightforward method of utilizing the polarization of the laser beam as a reference. Since the polarization plane is normal to the beam axis, this reference would lend itself to roll angle determination.

Consider a light beam of electric field polarization and magnitude indicated by the direction and magnitude of the arrow in Figure 2a, incident on a polarized filter with polarization direction indicated by the crosshatched lines. If the polarization direction of the incident light and of the polarized filter are parallel, then the light is transmitted (except for attenuation and reflection losses) with no loss in intensity. If the polarized filter is rotated through an angle  $\theta$ , the incident radiation

polarization is no longer parallel to the filter polarization and only that component of the electric field vector parallel to the filter polarization will be transmitted as shown in Figure 2b. At  $\theta$  equal to  $90^\circ$  there will be no component of the electric field vector parallel to the filter polarization and no light will be detected by the photocell as shown in Figure 2c. At  $\theta$  equal to  $180^\circ$ , the intensity detected is again maximum. Thus, if both the polarized filter and photocell sensor were rigidly attached to the inertial platform, any rotation of the inertial platform would cause a periodic modulation of the intensity transmitted and detected at a frequency twice the rotation rate.

Still assuming idealized conditions the intensity at the photocell sensor is governed by (Ref 5 : 495)

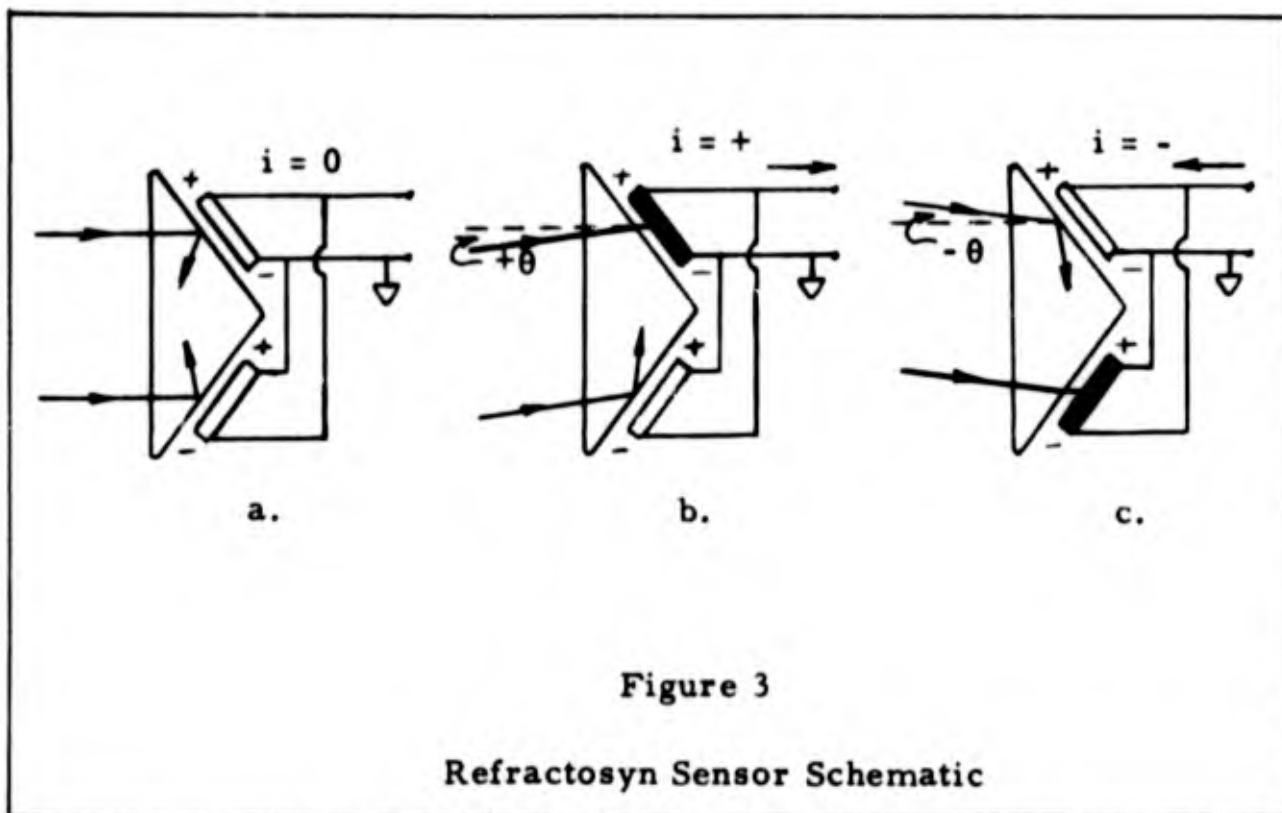
$$I = I_0 \cos^2 \theta \quad (1)$$

where  $I_0$  is the intensity incident on the polarized filter.

The rate of change of the intensity with angle is given by

$$\frac{dI}{d\theta} = - I_0 \sin 2\theta \quad (2)$$

Pitch/Yaw Refractosyn Sensor. This technique employs a commercially available angle sensing device called the Refractosyn. The Refractosyn sensor consists of two photocells and an isosceles prism cut at the critical angle. This angle can be optimized for any wavelength desired. At null position when incident light rays are normal to the base of the isosceles prism (See Figure 3), the rays are totally reflected and the current at the output is essentially zero. Rotation of the Refractosyn to the left or right with respect to the incident light beam causes abrupt refraction of light onto one or the other of the two opposing photocells, generating either a plus or minus signal as shown in Figure 3.



Here again the angular rotation modulates the amplitude of the light intensity. Such a device mounted rigidly on an inertial platform could be used to sense either pitch or yaw angular rotation.

The effective intensity at one sensor neglecting absorption and reflection losses through the prism is given approximately by

$$I \cong I_o \left( \frac{2}{n_g} \right)^{\frac{1}{2}} (n_g^2 - 1)^{\frac{1}{2}} (\sin \theta)^{\frac{1}{2}} \quad (3)$$

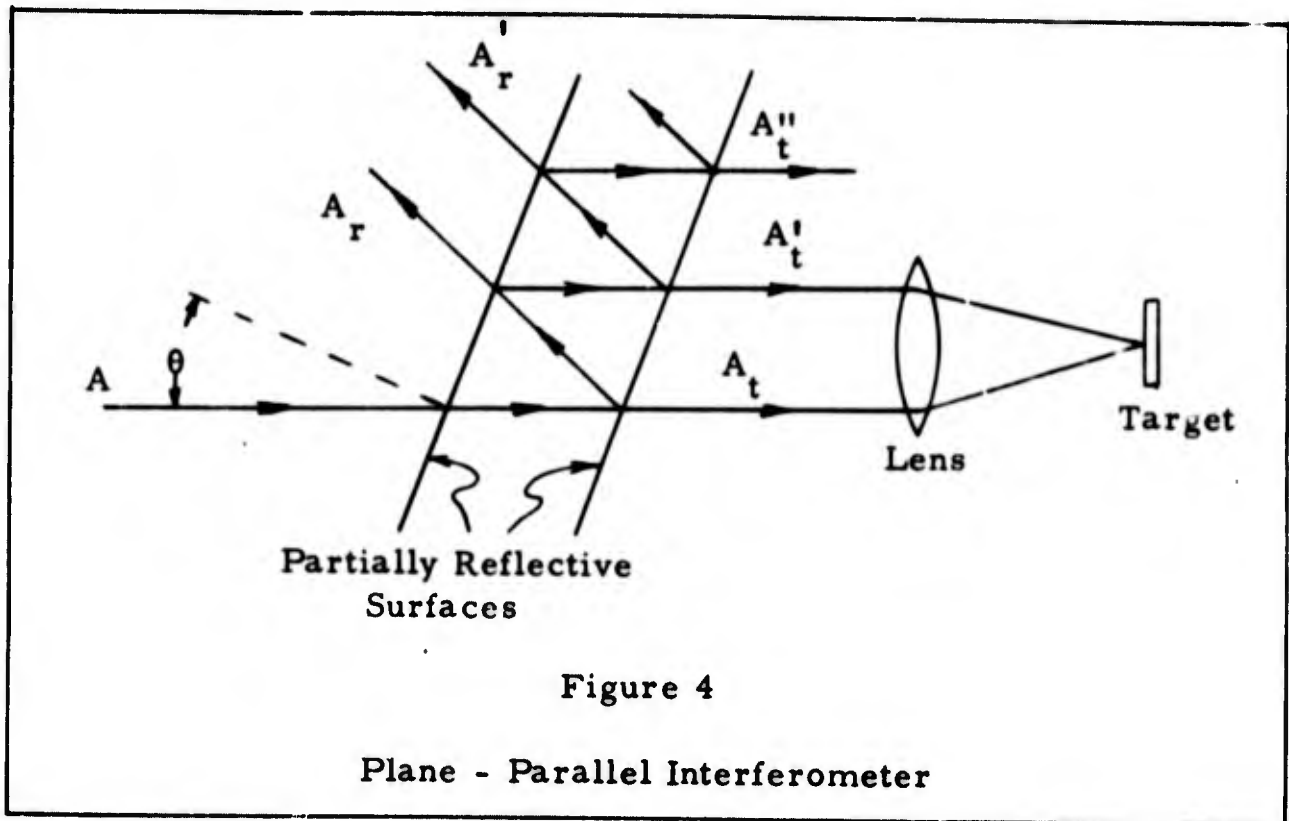
where  $n_g$  equals the index of refraction of the glass prism. This equation is developed in Appendix A and utilizes the assumption that  $\theta$  is very small. The sensitivity of this sensor,  $\frac{dI}{d\theta}$ , is given by

$$\frac{dI}{d\theta} \cong \frac{I_o}{2} \left( \frac{2}{n_g} \right)^{\frac{1}{2}} (n_g^2 - 1)^{\frac{1}{2}} \frac{\cos \theta}{\sqrt{\sin \theta}} \quad (4)$$

Equations (3) and (4) hold so long as no reflected light from the opposite side of the prism hits the activated photocell. At small angles this reflected light exceeds the critical angle of both sides of the prism and thus will not activate either sensor. At larger incidence angles, the reflected light from the opposite prism side will be incident on the prism side under consideration at an angle less than the critical angle, and thus, will begin to introduce additional light on the photocell under consideration. The incidence angle at which this occurs is about  $13^{\circ}$ . At this point a new expression must be derived to account for the additional light. However, since we are only concerned with measuring a small range of angles at the most sensitive region of the device and since the most sensitive region is at small angles, equations (3) and (4) will suffice.

Equation (4) indicates that the maximum instantaneous angle sensitivity is at zero degrees and is infinite. Aside from practical problems which will prevent achieving this sensitivity, as soon as the angle starts to increase slightly the instantaneous sensitivity will become finite and the average sensitivity between 0 and any small finite angle will always be finite. Practically, however, the sensitivity at zero angle also depends on the sensitivity of the photocell to grazing incidence light and the abruptness of the transition from totally reflected light to partially refracted light at the critical angle. Thus, equations (3) and (4) undoubtedly do not hold for angles very close to zero.

Pitch/Yaw Interferometer Sensor. This technique employs two plane-parallel reflective surfaces which form a Fabry-Perot type interferometer. The two reflective surfaces act as beam splitters and split incoming rays so that one set of rays travels a different optical path than the other set of rays. When these rays are brought



together again they will, in general, be out of phase and will interfere. Figure 4 shows a schematic of the beam splitting action on a ray of light from a monochromatic but not necessarily coherent source. A lens is shown to bring the rays together at the focus.

As illustrated, ray A is split into two sets of parallel rays.  $A_t, A_t', A_t'',$  and so forth, and  $A_r, A_r', A_r'',$  and so forth. The intensity of each ray decreases at each subsequent reflection. Consider for the moment only rays  $A_t$  and  $A_t'$ . If these two rays are now passed through a lens, they will be brought together at a point in the focal plane of the lens. Since  $A_t'$  has traveled a greater optical path than  $A_t$ , we will observe interference between  $A_t$  and  $A_t'$ . For a given angle of incidence,  $\theta$ , the optical path difference will be constant. However, as  $\theta$  varies, the path difference varies and thus the intensity of the focused spot will vary periodically. The angle is related to the number of cycles of intensity variations counted. Such a device can obviously be used to measure pitch or yaw angle.

The optical path difference  $\Delta$  can be shown to be

$$\Delta = 2 d \cos \theta \quad (5)$$

where  $d$  is the normal distance between the two reflective surfaces and  $\theta$  is the angle of incidence (Ref 5 : 247). The number of wavelengths within the distance  $\Delta$  is

$$m = \frac{\Delta}{\lambda} = \frac{2 d}{\lambda} \cos \theta \quad (6)$$

Whenever  $m$  is an integer, the intensity of the interference region is maximum, and when  $m$  is an integer plus one half, it is a minimum.

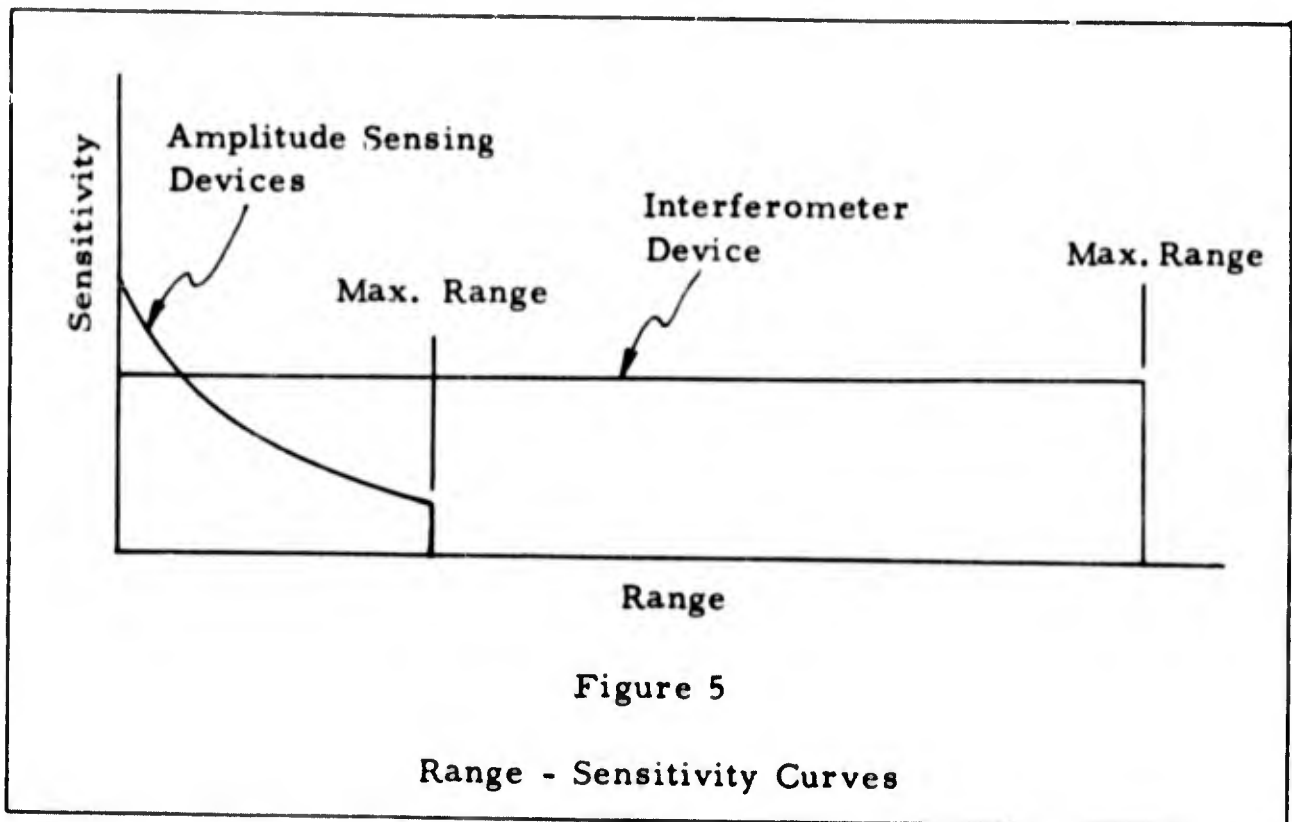
The sensitivity can be defined as  $\left| \frac{dm}{d\theta} \right|$  which is given by

$$\left| \frac{dm}{d\theta} \right| = \frac{2d}{\lambda} \left| \sin \theta \right| \quad (7)$$

Sensitivity increases with  $d$  and  $\theta$  as shown in Equation (7). However, practical considerations will limit the magnitudes of  $d$  and  $\theta$ . It should be noted that the sensitivity is not a function of intensity.

Comparison of Angle Sensing Techniques. The basic difference between the interferometer angle sensor and the Refractosyn and polarization sensors, is that the sensitivity of the interferometer is a function of the frequency of the resulting signal while the sensitivities of each of the other two devices are functions of the amplitude of the signal. Thus, for monitoring of angular position over large distances the interferometer has an inherent advantage in that its sensitivity does not degrade with range.

The Refractosyn and polarization sensors are limited in range primarily by sensitivity requirements. For example, if a given change in angle causes a fractional change in the detected intensity,  $f I (R)$ , then the range of the system is determined by the range



at which  $fI(R)$  can be detected. The higher the desired accuracy, the smaller the fraction  $f$ . In the case of the interferometer the range is not determined at all by sensitivity considerations. Instead the range is determined by the minimum detectable peak-to-peak signal which can even be larger than  $I(R)$  as will be shown in Section II. Thus, the interferometer enjoys an appreciable advantage over the amplitude detection devices from the standpoint of range and sensitivity. Qualitatively this effect can be demonstrated by Figure 5.

Referring to the two curves in Figure 5 we can see that although the amplitude sensing devices may possibly have a higher sensitivity at short distances, their sensitivity will in general drop below the interferometer sensitivity at some point. Meanwhile the interferometer angle sensing device shows no degradation in sensitivity with range and has a much larger limiting range.

The interferometer device also enjoys some advantage in that it is not as susceptible to noise in the light beam. As the level of intensity shifts in the light beam, the amplitude sensing devices cannot distinguish these shifts from intensity shifts caused by angular changes. The interferometer, on the other hand, will not sense these intensity shifts as angular changes unless these shifts occur at about the same frequency as the phase shifts in the interferometer. This is unlikely since the phase shifts occur at a much higher rate than the periodic angular changes. However, in both cases the light beam noise can be monitored prior to incidence on the sensors and correlated out of the resulting signals so that the noise advantage may not be as significant an advantage for the interferometer as the sensitivity and range advantages discussed above.

All devices discussed above are of course susceptible to angular changes in the incident beam caused by refraction in the atmosphere or refraction through shock waves. Refraction due to shock waves can probably be predicted quite accurately as a function of Mach number. The atmospheric refraction effects are not very predictable due to their random nature. The severity of this effect has not as yet been investigated and is considered beyond the scope of this study.

Based on the considerations discussed above the interferometric approach to the angle sensing problem was chosen as the subject of investigation for the research reported herein.

### III. Theoretical Aspects of the Angle Sensing Interferometer

The Fabry-Perot type interferometer can be constructed of two optical flats with one surface of each coated with a reflective coating, or of a solid piece of optical glass with two surfaces ground flat and parallel to each other and properly coated.

If the two optical flats configuration is used the parallel adjustment is quite critical, and it is unlikely that parallelism can be maintained under the accelerations and vibrations of a typical sled run. The solid configuration once properly ground and polished would require no adjustment and would be a much more rigid structure.

Since the solid configuration is more applicable to the problem at hand, all subsequent theoretical considerations will refer to the solid configuration.

#### Beam Divergence, Surface Flatness and Parallelism

Before proceeding to the discussion of the analytical equations governing the behavior of the interferometer, the qualitative effects of beam divergence, surface flatness, and parallelism of the two surfaces will be discussed.

The area of interference will be uniform in intensity level provided the beam is parallel and the surfaces are flat and parallel, since in this case the optical path difference is not a function of the position of a ray in the interferometer field. This type of interference is called full field interference. Deviation of any one of these specifications from the ideal can have significant effects on the interference pattern.

Consider first the effects of lack of parallelism. Should the two reflective surfaces be out of parallel, the gap between them will no longer be uniform, but, in fact will be wedge-shaped. In this case, the straight-through rays will not be parallel to the twice reflected rays and in general the optical path difference for rays split at various points on the reflective surfaces will not be equal. In the direction parallel to the intersection of the wedge surfaces there will be no variation in optical path difference, while normal to this direction there will be a linear variation in optical path difference. Thus the interference area will exhibit alternating lines of dark and bright aligned in a direction parallel to the intersection of the wedge surfaces. The spacing of these lines or fringes will be inversely proportional to the wedge angle.

Consider next the effect of beam divergence. A beam of given divergence consists of rays at various angles with respect to the centerline of the beam. If such a beam is incident normal to the interferometer, the optical path difference of each ray will not be uniform but will depend on the angle any given ray makes with the center of the beam and the interferometer. In a uniformly divergent beam, the locus of all rays of equal angle with respect to the center of the beams consists of a cone with centerline coincident with the beam centerline. In any cross section of the beam, the locus is a circle. Thus, there will be no optical path difference variation along circles whose centers are coincident with the beam center. Optical path variations will be observed in all radial directions. Thus, the interference pattern will consist of concentric alternating bright and dark rings. If the interferometer is tilted the interference pattern will still consist of concentric rings, but their

center will no longer be coincident with the center of the beam. In fact, if the interferometer is tilted enough, the center of the rings will move out of the field of view and the interference pattern will consist of concentric arcs.

If the surface is not flat to a very high degree, the interferometer gap will not be uniform. Effectively this situation can be considered equivalent to many segments of wedges assembled in a complex manner depending on the contour of the surface. The resulting fringe pattern is unpredictable in general except that the pattern will be irregular in shape.

For any given interferometer, the interference pattern will be a combination of the three patterns discussed above depending on the extent to which each specification deviates from the ideal.

Full field interference is desirable so that maximum signal can be obtained when utilizing a light sensor to detect and count fringe shifts. (Full field interference can be considered as consisting of a fringe pattern whose fringe thicknesses are much larger than the dimension of the field.) Since a typical light sensor is a spatial integrating device which gives a signal proportional to the total radiant flux incident on it, maximum signal or contrast is obtained when the sensor is illuminated with a full field interference pattern. In fact, if any equal number of bright and dark fringes are incident on a sensor essentially no contrast or signal will be observed as fringes shift since each dark fringe will counterbalance each bright fringe. It is only possible for a sensor to detect fringe shifts if an odd number of fringes are incident on it. However, given an odd number of fringes, the larger the number, the lower the contrast or signal.

Optical Path Difference

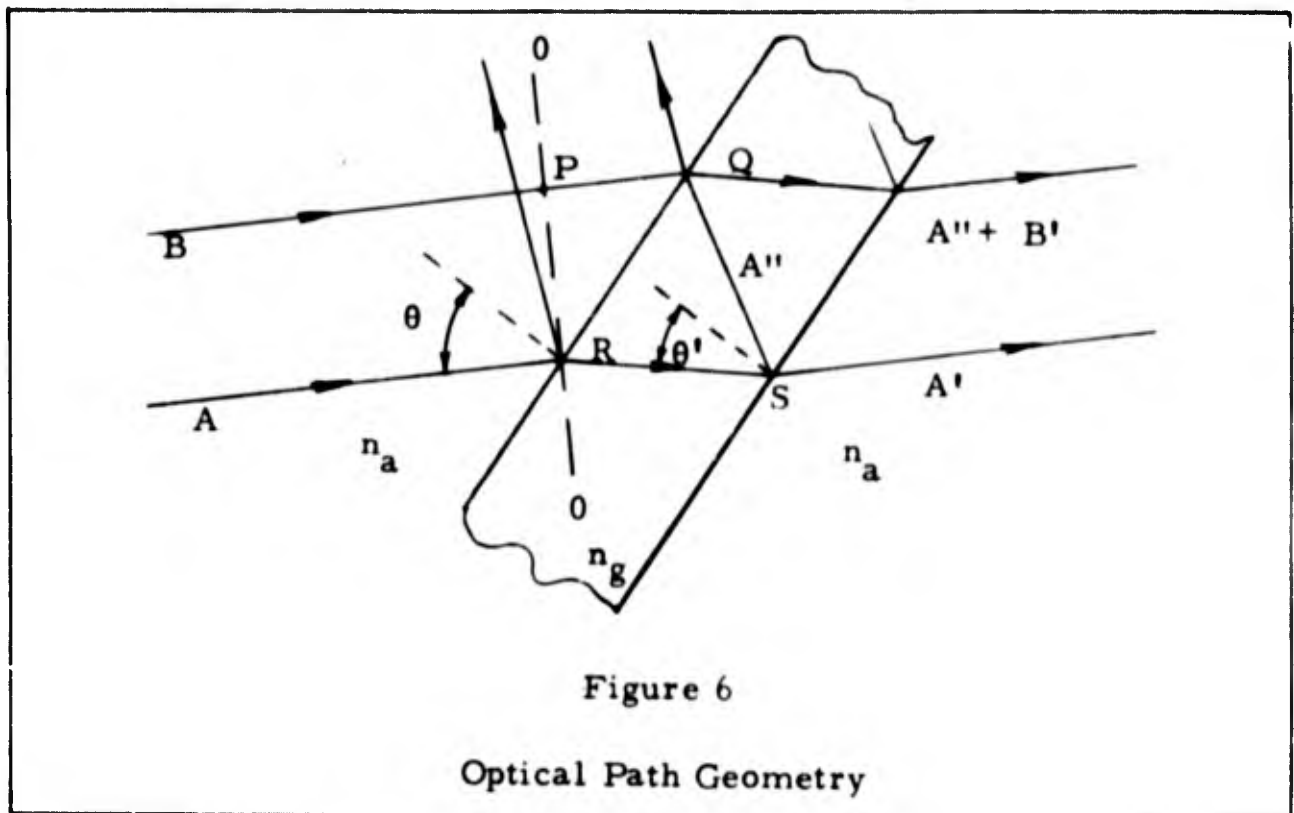
Since we would like to obtain full field interference, we will take the approach of assuming that the required specifications for the full field effect are met and develop the necessary equations on this assumption. Subsequently we can make approximate calculations to see how closely these specifications must be met and then experimentally determine whether they can be met.

The basic equation governing the interferometer as an angle sensing device is the equation relating the optical path difference to the angle of the interferometer,  $\theta$ . Figure 6 shows the geometry of the optical path difference introduced by the plane-parallel interferometer. With a coherent light source such as the laser, it is not necessary that ray A'' be made to interfere with ray A'. Any coincident ray such as ray B' can interfere with A''. As shown in Appendix B, the following equations are applicable to both the cases where B' or A' interferes with A''.

Until the wavefront of rays A and B arrive at plane 00, both rays travel the identical optical paths. While ray A'' continues on to travel the path RS + SQ, ray B' travels the path PQ. From the point Q on, both rays travel the same optical paths again. The optical path difference between B' and A'' is the difference between  $n_g (RS + SQ)$  and  $n_a (PQ)$ , where  $n_g$  and  $n_a$  are the indices of refraction of the glass and air, respectively. The following equations are derived in Appendix B.

If the distance between the two surfaces is  $d$  then the optical path difference  $\Delta$  is

$$\Delta = 2d \sqrt{n_g^2 - n_a^2 \sin^2 \theta} \quad (8)$$



The number of wavelengths  $m$  in the optical distance  $\Delta$  is

$$m = \frac{\Delta}{\lambda_0} = \frac{2d}{\lambda_0} \sqrt{n_g^2 - n_a^2 \sin^2 \theta} \quad (9)$$

where  $\lambda_0$  is the vacuum wavelength of the light. From Equation (9) it is obvious that  $m$  is not zero at zero angle and as the angle increases,  $m$  decreases. Thus  $m$  can be written as

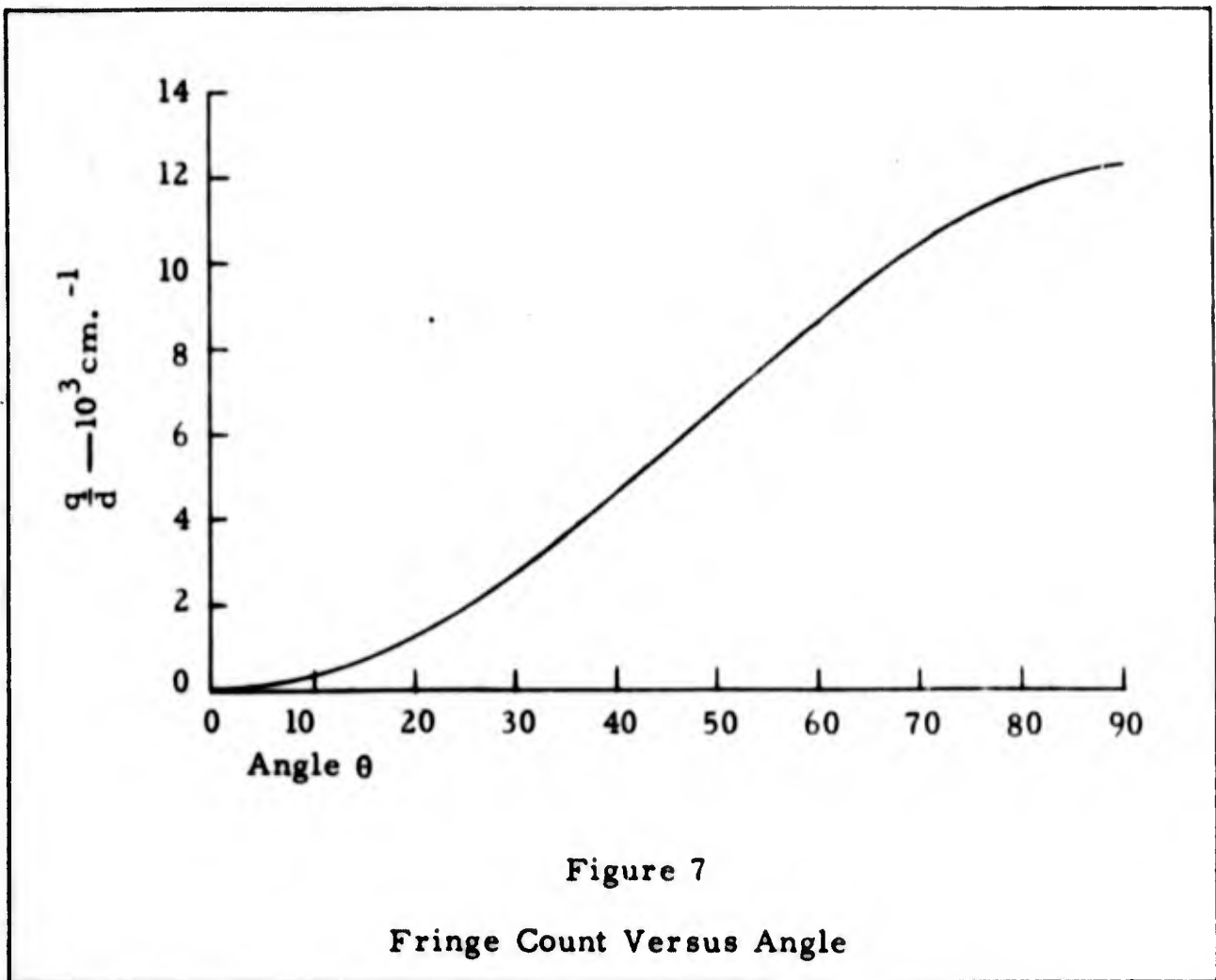
$$m = m_0 - q, \quad (10)$$

where  $m_0$  is the value of  $m$  at zero angle,

$$m_0 = \frac{2dn_g}{\lambda_0} \quad (11)$$

The fringe count from the normal is represented by  $q$  and is given by

$$q = \frac{2d}{\lambda_0} \left[ n_g - \sqrt{n_g^2 - n_a^2 \sin^2 \theta} \right] \quad (12)$$



The angle  $\theta$  is given by the following equation.

$$\sin \theta = \frac{1}{2n_a} \sqrt{\frac{q\lambda_o}{d} (4n_g - \frac{q\lambda_o}{d})} \quad (13)$$

A plot of  $\theta$  versus  $\frac{q}{d}$  is shown in Figure 7. The parameter  $\frac{q}{d}$  is essentially the fringe count per unit thickness of the interferometer.

We are now in a position to make some order of magnitude calculations on surface parallelism and flatness and beam divergence specifications required for effective full field interference.

For a wedge-shaped interferometer, the phase shift index  $m$  will vary from point-to-point across the field of the beam. At the thicker end of the wedge  $m$  will be greater than at the thinner end of the wedge. The difference in phase shift index across the field will be given by

$$\Delta m = \frac{2\Delta d}{\lambda_0} \sqrt{n_g^2 - n_a^2 \sin^2 \theta} \quad (14)$$

where  $\Delta d = d_2 - d_1$  and  $d_2$  and  $d_1$  are the thicknesses of the wedge at the thicker and thinner ends of the wedge, respectively. Solving for  $\Delta d/\lambda_0$  gives

$$\frac{\Delta d}{\lambda_0} = \frac{\Delta m}{2} \left[ n_g^2 - n_a^2 \sin^2 \theta \right]^{-\frac{1}{2}} \quad (15)$$

Thus, for a given specification of  $\Delta m$ , a  $\Delta d$  can be calculated which can be specified as the maximum allowable  $\Delta d$ . This maximum allowable  $\Delta d$  must be the minimum  $\Delta d$  which can be calculated from Equation (15) for various angles. Minimum  $\Delta d$  occurs at  $\theta = 0$ .

For full field interference  $\Delta m$  must be equal to zero which requires  $\Delta d = 0$  as expected. However, from practical considerations, if a  $\Delta m$  of about 0.5 over the diameter of the field can be tolerated, then the maximum allowable  $\Delta d/\lambda_0$  is calculated to be equal to 1/6 of a wavelength. Over a 2 inch diameter field and at the laser wavelength of  $6328\text{\AA}$ , this corresponds to a wedge angle of about 0.44 arc sec. The specification of a maximum allowable phase difference from one edge of the field to the other of 0.5 means that the field will be within one half of a fringe from edge-to-edge. The width of a fringe as used here refers to the distance between successive maxima or minima.

Similarly, we can specify a phase tolerance limit across the diameter of the interferometer due to beam divergence, and calculate an allowable beam divergence angle using Equation (13). Again for

this calculation a  $\Delta q$  of 0.5 is specified. At normal incidence and for  $n_a = 1$ ,  $n_g = 1.5$  and  $d = 3$  cm., the beam angle is calculated to be 820 arc sec. It is also interesting to make the same type of calculation at a large angle of incidence such as  $45^\circ$  to see how sensitive this specification is to angle. At  $45^\circ$  the beam angle corresponding to  $\Delta q = 0.5$ , is 2.7 arc sec.

At normal incidence this specification is easily met with the laser used which has a nominal beam divergence of 80 arc sec. At  $45^\circ$  the laser beam should be collimated down to less than 2.7 arc sec. The laser beam can probably be collimated down to this range with suitable optics.

The  $\Delta d$  calculated above also specifies the flatness required if the phase difference between any two points in the field is to be no greater than 0.5 wavelengths. Thus, a flatness to less than  $1/6$  wavelength should be adequate. Higher degrees of flatness can be readily obtained.

### Angular Sensitivity

The angular sensitivity of the plane-parallel interferometer can be defined as either the rate of change of  $q$  with respect to  $\theta$  or the rate of change of  $\theta$  with respect to  $q$ .

If  $\frac{dq}{d\theta}$  defines the sensitivity, an increase in  $\frac{dq}{d\theta}$  corresponds to an increase in sensitivity. If  $\frac{d\theta}{dq}$  defines the sensitivity, a decrease in  $\frac{d\theta}{dq}$  corresponds to an increase in sensitivity. The first definition,  $\frac{dq}{d\theta}$ , will be utilized in this paper.

The sensitivity in terms of  $m$  is derived in detail in Appendix B. Since  $m = m_0 - q$ ,  $\frac{dq}{d\theta} = -\frac{dm}{d\theta}$ ,

$$\frac{dq}{d\theta} = \frac{d}{\lambda_0} n_a^2 \sin 2\theta \left[ n_g^2 - n_a^2 \sin^2 \theta \right]^{-\frac{1}{2}} \quad (16)$$

We see that the sensitivity is a function of  $d$ ,  $n_g$ ,  $\lambda_0$ , and  $\theta$ .

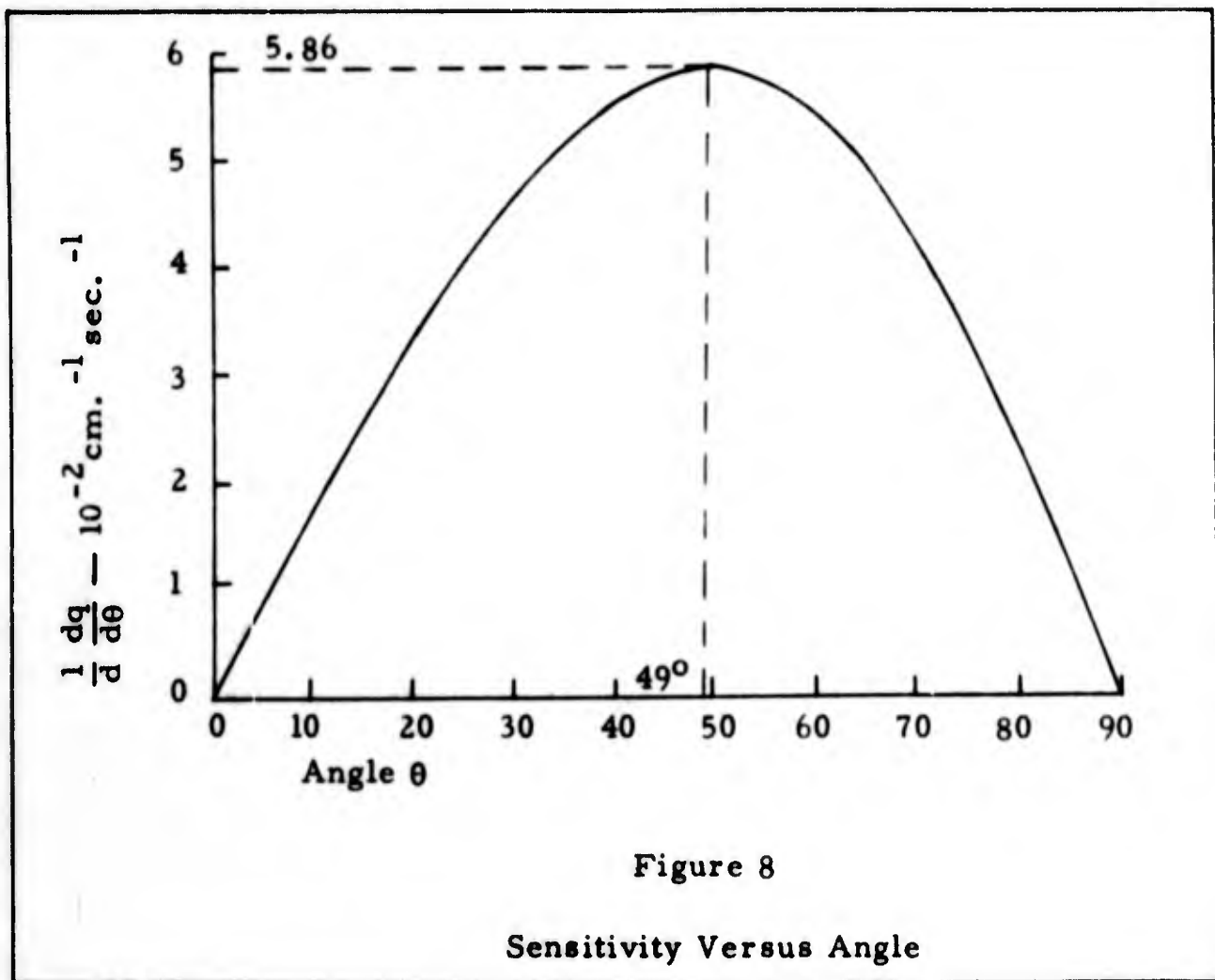
As  $\lambda_0$  decreases the sensitivity increases so that low wavelength light is desirable. Although lower wavelength lasers have been demonstrated the He-Ne laser was the only laser available for this thesis project. Thus, the wavelength can be considered fixed at  $6328 \text{ \AA}$ .

The indices of refraction of glass or other transparent materials, such as fused quartz, which might be used to construct the interferometer, are in the neighborhood of 1.5. From Equation (16) it is obvious that the lower the index of refraction, the higher the sensitivity. Most glasses have indices above 1.5 while fused quartz has indices both above and below 1.5 depending on wavelength. At  $6328 \text{ \AA}$  the index of refraction of fused quartz is 1.457. Thus fused quartz is a likely material to use.

The two remaining parameters are  $d$  and  $\theta$  both of which result in increasing sensitivity with increasing magnitude. The sensitivity increases continuously with increasing  $d$ . However, there exists an angle  $\theta$  at which the sensitivity is maximum. The equation giving this angle is derived in Appendix B and is

$$\sin \theta_m = \left[ \frac{n_g^2}{n_a^2} - \frac{n_g}{n_a} \sqrt{\frac{n_g^2}{n_a^2} - 1} \right]^{\frac{1}{2}} \quad (17)$$

A plot of  $\frac{1}{d} \frac{dq}{d\theta}$  versus  $\theta$  is shown in Figure 8. The calculations were based on  $n_g = 1.5$  and  $n_a = 1.0$ . This graph shows a maximum sensitivity of  $(0.0586 d)$  fringes per arc sec. at an angle of  $49^\circ$ .

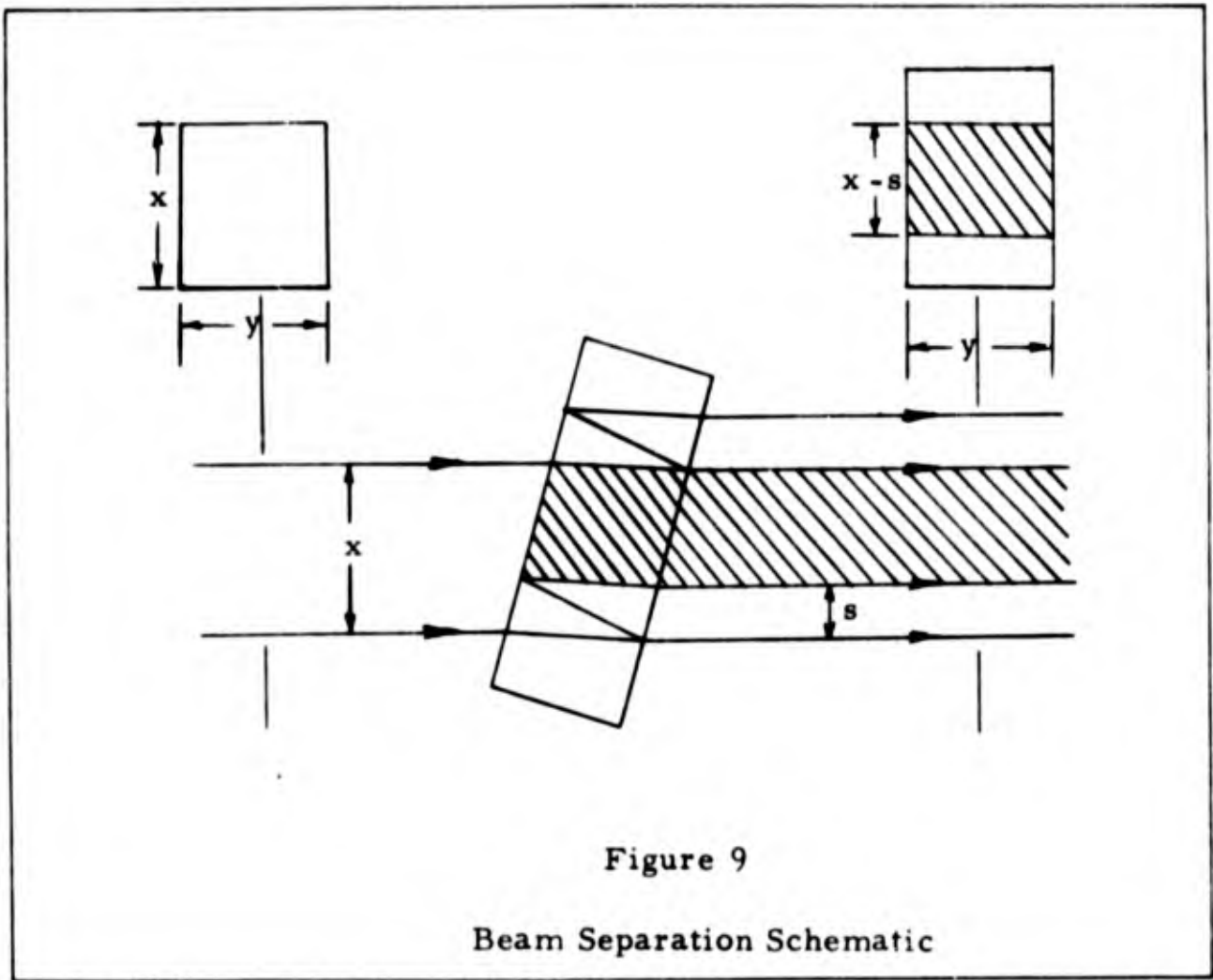


The selection of  $d$  and  $\theta$  cannot be made independently, but must be based on the considerations of the separation between the straight-through and twice reflected rays for practical reasons. The problem of beam separation will be discussed next.

### Beam Separation

Consider a beam of light rectangular in cross-section with dimensions  $x$  and  $y$ , passing through the interferometer. This is shown schematically in Figure 9. The two split beams emerge separated by a distance  $s$  and overlapping by a distance  $x - s$ , provided  $x > s$ . The area of overlap will be given by

$$A_o = \frac{x - s}{x} A \quad (18)$$

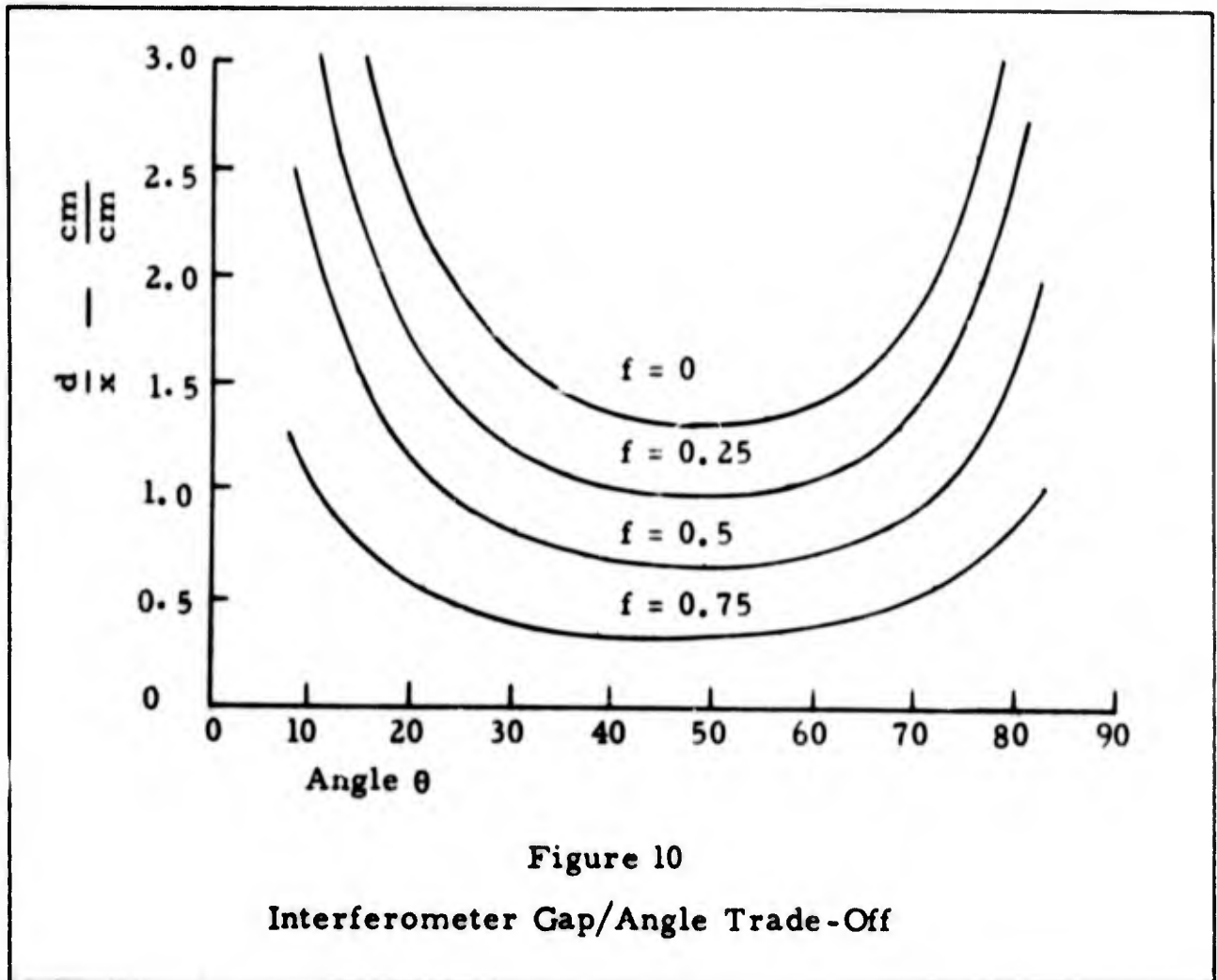


From Equation (18) it is obvious that the larger the ratio of  $s$  to  $x$ , the smaller the area of interference and the smaller the contrast between a maximum and minimum intensity condition. Increasing either  $\theta$  or  $d$  results in increasing  $s$ . Thus, there must be a trade-off between  $\theta$  and  $d$  to achieve a given separation.

The expression for  $s$  is developed in Appendix B and is

$$s = n_a d \sin 2\theta \left[ n_g^2 - n_a^2 \sin^2 \theta \right]^{-\frac{1}{2}} \quad (19)$$

It should be noted that Equation (19) is of the same form as the sensitivity equation (Equation (16)). Thus,  $s$  will be maximum at  $\theta = \theta_m$ . A plot of  $\frac{s}{d}$  versus  $\theta$  will be of the same form as the plot in Figure 8. At maximum separation,  $\frac{s}{d} = .765$ .



The ratio of the overlap area to the beam area,  $f$ , can by use of Equation (19) be written

$$f = 1 - \frac{n_a d \sin 2\theta}{x} \left[ n_g^2 - n_a^2 \sin^2 \theta \right]^{-\frac{1}{2}} \quad (20)$$

For a given fraction  $f$  and dimension  $x$  the trade-off between  $d$  and  $\theta$  is governed by

$$d = \frac{x(1-f)}{n_a} \frac{\sqrt{n_g^2 - n_a^2 \sin^2 \theta}}{\sin 2\theta} \quad (21)$$

A plot of  $\frac{d}{x}$  versus  $\theta$  for various values of  $f$  is shown in Figure 10 based on  $n_g = 1.5$  and  $n_a = 1$ . Thus, for example, at  $\theta = 49^\circ$  and for  $f = 0.5$  the ratio of  $\frac{d}{x}$  should be about 0.654.

Beam Reflection and Transmission

The partially reflective surfaces of the interferometer can be either thin metallic coatings or multi-layer dielectric coatings. The metallic coating differs from a dielectric in that the electrons in a dielectric are generally bound to the atoms and are free only to oscillate about centers of force. For metals there are many free electrons and it is these which are chiefly responsible for the high reflecting power as well as the high absorption of metals.

In general, the reflectance of metallic films is different on the two sides when the bounding regions are of different refractive index. Phase changes occur at reflection and transmission and these phase changes are a function of the thickness of the layer, the angle of incidence, the polarization, the wavelength, and the preparation of the surface. It is almost impossible to obtain specific information on their values except by experimental observation of a particular sample. Detailed discussion of reflection and transmission in thin films is presented in Reference 4.

The reflectance, transmittance, and phase are generally not strong functions of angle for angles less than  $50^\circ$ . At larger angles the variations in these parameters with angle become much more rapid. For small angle variations about some angle less than  $50^\circ$  these parameters can probably be considered constant for any given sample.

Dielectric coatings can also be used to achieve any desired ratio of reflected to transmitted intensity. The principle utilized in these dielectric coatings is that of interference. By properly selecting the indices of refraction and thicknesses, the interference effect within the coatings can be utilized to suppress or enhance the reflected intensity.

The phase shifts caused by reflection from dielectric surfaces are either  $0$  or  $\pi$ . The phase shift depends on the polarization of the light with respect to the plane of incidence, on the angle of incidence and on whether the reflection is taking place in the less dense or more dense medium. Light polarized normal to the plane of incidence is shifted by  $\pi$  radians at reflections in the less dense medium. Parallel polarized light experiences no phase shifts up to the polarizing angle and thereafter is shifted  $\pi$  radians. For reflections in the more dense medium the phase shifts are exactly reversed for both polarizations. No phase shifts accompany transmissions.

For a beam entering a dense medium, the rays will be refracted and the cross-sectional area of the beam will be increased. If the reflectance and transmittance are denoted by  $r$  and  $t$ , respectively, and are defined as the ratios of the energy reflected or transmitted, then

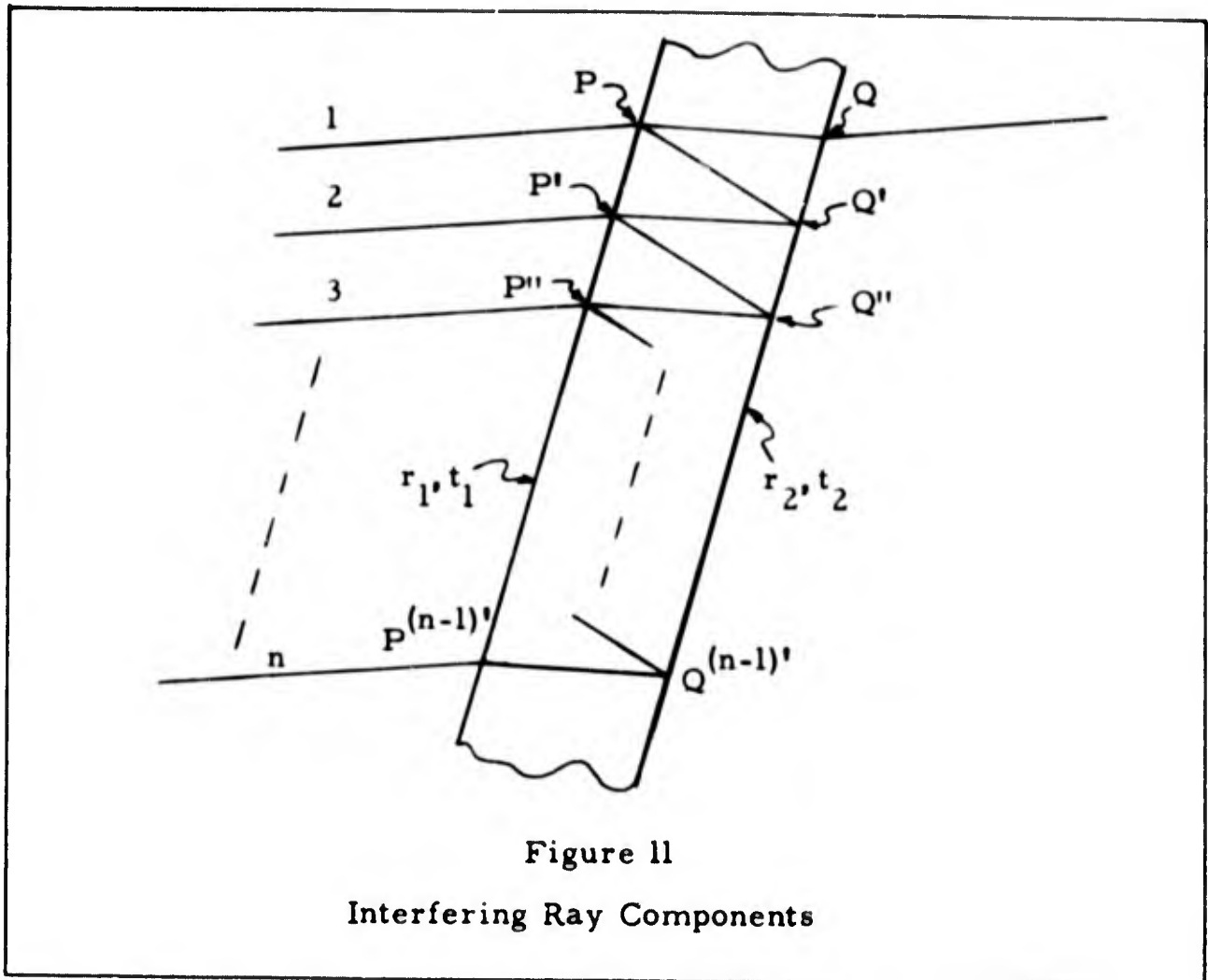
$$\left. \begin{aligned} I \text{ (reflected)} &= r I \text{ (incident)} \\ I \text{ (transmitted)} &= t \frac{\cos \theta}{\cos \theta'} I \text{ (incident)} \end{aligned} \right\} \quad (22)$$

where  $\frac{\cos \theta}{\cos \theta'}$  is the ratio of the beam cross section in the less dense medium to the cross section in the more dense medium. In the case of the beam entering the less dense medium,  $\theta$  and  $\theta'$  must be interchanged in Equation (22). The relationship between  $r$  and  $t$  neglecting absorption is

$$r + t = 1 \quad (23)$$

### Interference Intensity

The interference effect involves the electric field vector addition of two or more waves of the same frequency and polarization.



The resultant wave has an intensity that is given by the following equation developed in detail in Appendix C.

$$I = \sum_{i=1}^n I_i + 2 \sum_{i=1}^n \sum_{p=i+1}^n \sqrt{I_i I_p} \cos(a_i - a_p) \quad (24)$$

where the  $I_i$ 's and the  $I_p$ 's represent the intensities of each interfering wave,  $n$  represents the number of interfering waves and the  $a_i$ 's and  $a_p$ 's represent the relative phases. The  $I$ 's and  $a$ 's will of course depend on the reflectance and transmittance properties of the interferometer.

Figure 11 shows  $n$  incident rays which have some component of intensity at point  $Q$ . Only the resultant ray passing through point  $Q$

is shown emerging from the interferometer. This ray represents a typical ray in the interference field.

Each of the  $n$  incident rays passing through point  $Q$  must be specified by a magnitude and a phase angle. In the general case phase shifts accompany transmissions and reflections. We will denote phase shifts which occur on transmission through surfaces 1 and 2 as  $\gamma_1$  and  $\gamma_2$  and shifts which occur on reflection at surfaces 1 and 2 as  $\beta$ . In general  $\gamma_1 \neq \gamma_2$ , since at surface 1 the ray is passing from a less dense to a more dense medium while at surface 2 the opposite is true. Since all reflections of interest occur in the medium between surfaces 1 and 2,  $\beta_1 = \beta_2 = \beta$ . Phase differences due to optical path differences must also be accounted for. The optical path difference between any two successive rays of the  $n$  rays is equal to the optical path difference between any other two successive rays. The corresponding phase difference between successive rays will be designated  $2\pi m$  where  $m$  is given by Equation (9).

All rays passing through point  $Q$  can now be listed.

$$\begin{array}{l}
 I_1 = I_o t_1 t_2 \frac{\angle \gamma_1 + \gamma_2}{\phantom{\angle \gamma_1 + \gamma_2}} \\
 I_2 = I_o t_1 t_2 r_1 r_2 \frac{\angle \gamma_1 + \gamma_2 + 2\beta + 2\pi m}{\phantom{\angle \gamma_1 + \gamma_2 + 2\beta + 2\pi m}} \\
 I_3 = I_o t_1 t_2 (r_1 r_2)^2 \frac{\angle \gamma_1 + \gamma_2 + 4\beta + 2(2\pi m)}{\phantom{\angle \gamma_1 + \gamma_2 + 4\beta + 2(2\pi m)}} \\
 \vdots \\
 I_n = I_o t_1 t_2 (r_1 r_2)^{n-1} \frac{\angle \gamma_1 + \gamma_2 + (n-1)2\beta + (n-1) 2\pi m}{\phantom{\angle \gamma_1 + \gamma_2 + (n-1)2\beta + (n-1) 2\pi m}}
 \end{array} \quad (25)$$

The number of rays which must be taken into account depends on the size of the interferometer aperture, the distance between reflective surfaces, and the angle of incidence. The smaller the aperture, the smaller  $n$ . The smaller the distance  $d$  and the angle  $\theta$ , the larger  $n$ . The value of  $(r_1 r_2)^i$  drops rapidly as  $i$  increases. For a typical value of  $r$  of 0.5,  $(r_1 r_2)^2$  equals 0.0625 and  $(r_1 r_2)^3$  equals 0.0156. Therefore, only a small number of rays may be significant.

For any case where the number of multiply reflected interfering rays given by Equation (25) can be taken as infinite, the interference intensity given by Equation (24) is of course finite due to the convergent nature of the series. One example of such a case is when the angle of incidence between the light rays and the interferometer is zero. The interference intensity is then given by

$$\frac{I}{I_0} = \frac{E}{1 + F \sin^2 \frac{\delta}{2}} \quad (26)$$

where  $E = (1 - r_1)(1 - r_2)(1 - \sqrt{r_1 r_2})^{-2}$ ;  $F = 4\sqrt{r_1 r_2}(1 - \sqrt{r_1 r_2})^{-2}$ ; and  $\delta = 2(\beta + \pi m)$ . The phase  $\delta$  is  $(a_1 - a_2)$  as used in Equation (24). Note that for all the rays listed in Equation (25),  $(\gamma_1 + \gamma_2)$  cancels out when the difference  $(a_1 - a_p)$  is taken.

Equation (26) is derived in Reference 1: 323-324 for the case where  $r_1 = r_2$ . When  $r_1 = r_2 = r$ ,  $E = 1$  and  $F = r / (1-r)^2$ .

The region of overlap discussed thus far has been the region where the straight-through and twice reflected beams overlap. Since there will be many multiple reflections in the interferometer, there

will be other regions where the multiply reflected beams overlap with the straight-through, twice reflected, or other multiply reflected beams. The procedure for determining the interference intensity is to sum the rays in each region according to Equation (24). This can be a long and tedious process if the number of rays to be summed is very large. For some special cases simplifying approximations can be made which allow simple solutions by this procedure. It should be noted that the phase differences between all possible pairs of rays listed by Equation (25), may enter into the solution. In every case the phase constants  $\gamma_1$  and  $\gamma_2$  cancel out and the resulting phase differences will be multiples of ( $2\beta$  and  $2\pi m$ ).

For the case of dielectric surfaces or dielectric coatings on dielectric surfaces, phase shifts which occur on reflections are either 0 or  $\pi$  depending on the polarization and whether the light is being reflected in the less dense or more dense medium. Thus,  $2\beta$  will always be 0 or  $2\pi$  which in either case has no effect and can be dropped from the equation. On the other hand for metallic coated surfaces  $\beta$  will have some value other than 0 or  $\pi$  and thus cannot be neglected.

#### Maximum Range Considerations

The intensity incident at a point within the beam located at a distance R from the laser, is governed by factors such as absorption, scattering and beam divergence. In atmospheric conditions where high thermal gradients and gusts prevail, additional factors such as reflection and refraction must be considered. These factors require investigation at the Holloman track.

In general, the scattering effect may be considered negligible in clear, dry air. The only information available on atmospheric absorption of  $6328\text{\AA}$  light is derived from experiments performed within a long pipe (Ref 2: 1361). The estimated loss per 330 ft. of transmission was considerably less than 0.5%. Assuming a loss of 0.1% per 330 ft., the overall absorption loss over a distance of 35 kft. will be about 19%. Beam divergence losses will be much greater over the same distance.

Neglecting all of the above factors except beam divergence allows fairly straightforward upper limit calculations on the expected range of systems involving transmission of light beams.

The intensity of a light beam of divergence  $\rho$  and radiant flux  $F_0$  at a distance  $R$  is given by

$$I(R) \cong \frac{4F_0}{\pi(\rho R)^2} \quad (27)$$

A plot of  $I(R)/F_0$  versus  $R$  for  $\rho = 10$  arc sec. and  $\rho = 80$  arc sec. is shown in Figure 12. This curve shows that over the range from 1000 to 35000 feet the intensity falls off by about 3 orders of magnitude for each divergence. However, the level of the more parallel beam is in general 2 orders of magnitude higher. Thus from the maximum range standpoint as from the interference pattern quality standpoint, collimation of the beam is highly desirable.

The limiting range for the interferometer system will depend on the minimum peak-to-peak signal resolvable by the sensor and associated electronics. This minimum resolvable signal will in turn depend on the noise present in the system. Sources of noise are ambient light, atmospheric induced noise in the laser beam and electronic noise. Ambient noise can be effectively eliminated by

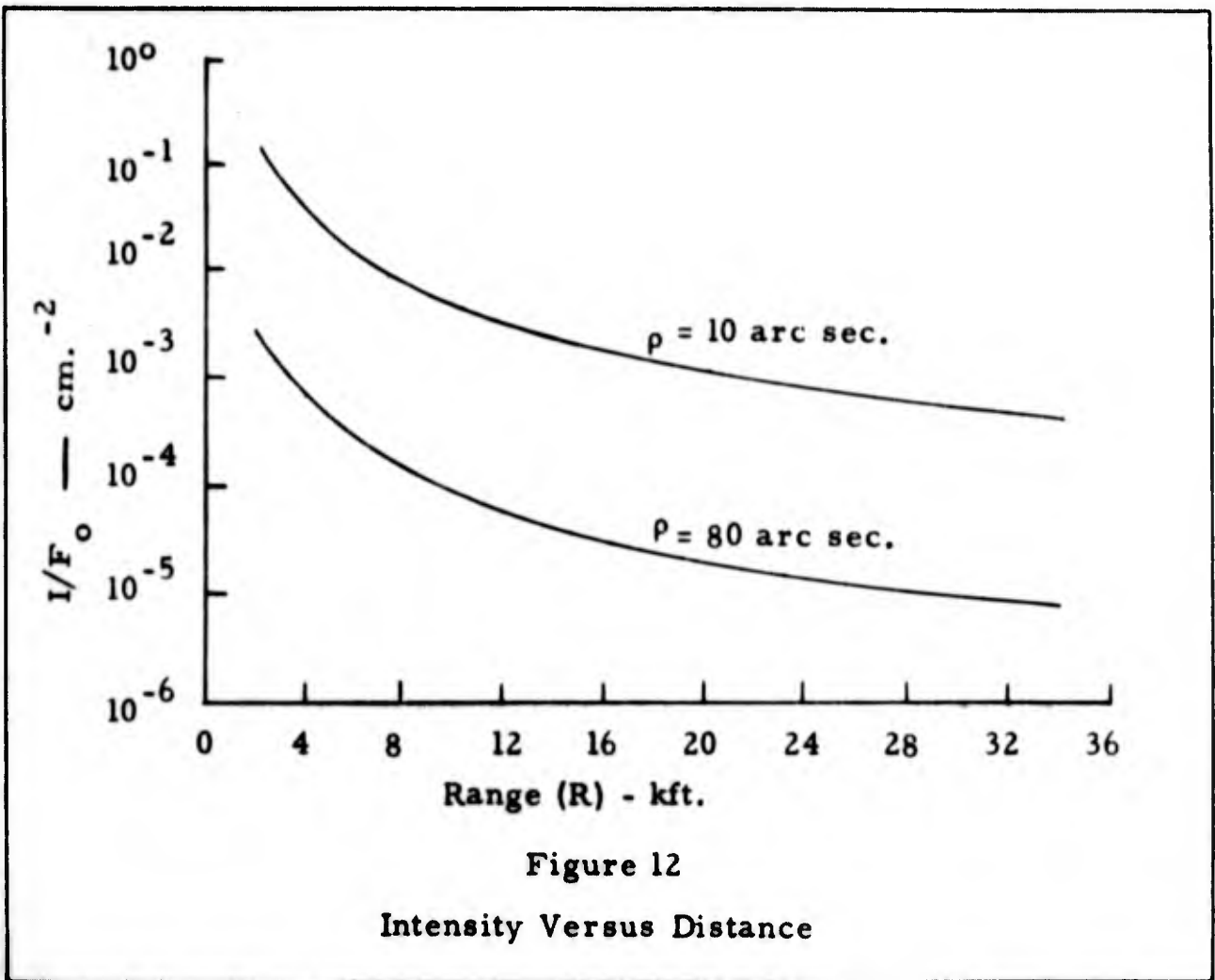


Figure 12  
Intensity Versus Distance

shielding and optical filtering. The noise in the laser beam itself can be monitored before entering the interferometer and subsequently correlated out of the signal emerging from the interferometer. The electronic noise may therefore be the predominating noise source.

If the peak-to-peak intensity signal at a given range,  $I'(\theta, R)$ , is detected by a photo sensor of current sensitivity  $k$ , area  $A$ , and load resistance  $R_L$ , then the peak-to-peak voltage signal is given by

$$V = k R_L A I'(\theta, R) \tag{28}$$

If the sensor is a photomultiplier of gain  $G$ , and quantum efficiency  $q$ , then  $k$  is given by

$$k = \frac{eqG}{h\nu} \tag{29}$$

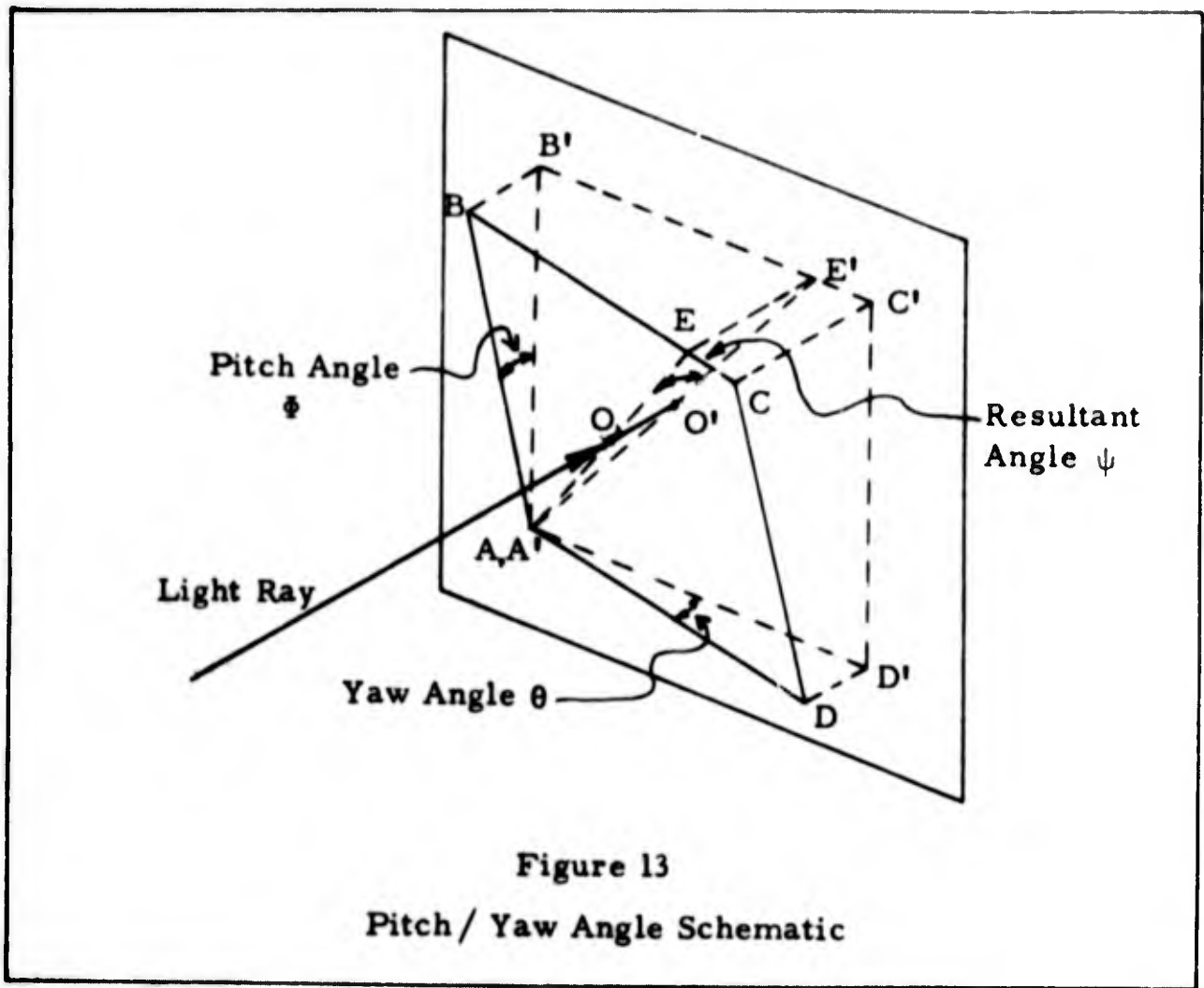
where  $e$  is the charge of an electron,  $h$  is the Planck's constant and  $\nu$  is the frequency of the light. The peak-to-peak intensity signal is calculated in terms of the incident intensity  $I(R)$  by use of Equation (24).

The upper limit range can be determined by the following procedure. Set  $V$  in Equation (28) equal to the minimum detectable signal and substitute the calculated peak-to-peak intensity signal ( in terms of  $I(R)$  ) in Equation (28). Solve for  $I(R)$  and divided  $I(R)$  by  $F_0$  for the particular light source. Equation (27) can then be used to calculate the maximum value of  $R$ . The actual range will be less than the value obtained due to the absorption and scattering effects of the atmosphere.

#### Combined Pitch and Yaw Effects

If both pitch and yaw occur simultaneously, the interferometer senses the resultant angle of its surfaces with respect to the light beam. The angle indicated by the interferometer system will not be either the pitch or yaw angle but a combination of both. Figure 13 illustrates the relation of these angles.

Figure 13 shows positions of two planes, one normal to the incident ray and the other (ABCD) representing the tilted surface of the interferometer. Plane  $A'B'C'D'$  is the projection of plane ABCD onto the normal plane. Plane ABCD is so chosen that A is coincident with  $A'$  and BD is normal to the incident ray. For any given tilt angle such a plane can be found provided the proper ratio of AD to AB is chosen. The pitch and yaw angle are those shown as  $\phi$  and  $\theta$  respectively. Line AE is a line in the plane ABCD passing



through point A and the intersection of the light ray with plane ABCD. This ray is so chosen that line AE is normal to line BD. Line A'E' is the projection of line AE onto the normal plane.

The angle between any two planes is the angle between the lines of intersection of each plane with a third plane normal to both planes. Plane AEE' satisfies this condition and lines AE and AE' are the intersections between the planes. Thus, angle EAE' is the angle between the planes and this angle will be designated  $\psi$ . It is  $\psi$  which the interferometer senses.

From the diagram it is obvious that

$$\left. \begin{aligned} \tan^2 \phi &= \left( \frac{BB'}{A'B'} \right)^2 \\ \tan^2 \theta &= \left( \frac{DD'}{A'D'} \right)^2 = \left( \frac{BB'}{A'D'} \right)^2 \\ \tan^2 \psi &= \left( \frac{OO'}{A'O'} \right)^2 = \left( \frac{BB'}{A'O'} \right)^2 \end{aligned} \right\} \quad (30)$$

Referring to triangle A'B'D', its area is given by

$$A = \frac{1}{2} (A'B') (A'D') = \frac{1}{2} (B'D') (A'O') \quad (31)$$

Also

$$(B'D')^2 = (A'B')^2 + (A'D')^2 \quad (32)$$

Squaring Equation (31), eliminating B'D' between the resulting equation and Equation (32), and solving for  $\frac{1}{(A'O')^2}$  gives

$$\frac{1}{(A'O')^2} = \frac{1}{(A'B')^2} + \frac{1}{(A'D')^2} \quad (33)$$

Substituting Equation (33) into the third Equation (30) gives

$$\tan^2 \psi = \left( \frac{BB'}{A'B'} \right)^2 + \left( \frac{BB'}{A'D'} \right)^2 \quad (34)$$

or

$$\tan^2 \psi = \tan^2 \phi + \tan^2 \theta \quad (35)$$

Equation (35) indicates that it is impossible to determine  $\phi$  or  $\theta$  uniquely with only one interferometer. However, if the angular variations are small, the interferometer can be biased so that it is much more sensitive to one or the other angle and the angle indicated by the fringe count can be made to approximate the angle toward which the interferometer is biased. This biasing is accomplished simply by setting the interferometer at an initial pitch or yaw angle with respect to the reference attitude.

The approximate angle measurement obtained in this manner will not be accurate enough for this attitude monitoring application. By properly using two angle sensing interferometers, one biased in pitch, the other in yaw, the two orthogonal angles can be determined mathematically from the two measured angles. Effectively, one interferometer per axis is required.

If one interferometer is set at an initial yaw angle  $\theta_0$ , and the other at an initial pitch angle  $\phi_0$ , then the angles  $\psi$  and  $\psi'$  measured by each interferometer will be related to the pitch and yaw angle by

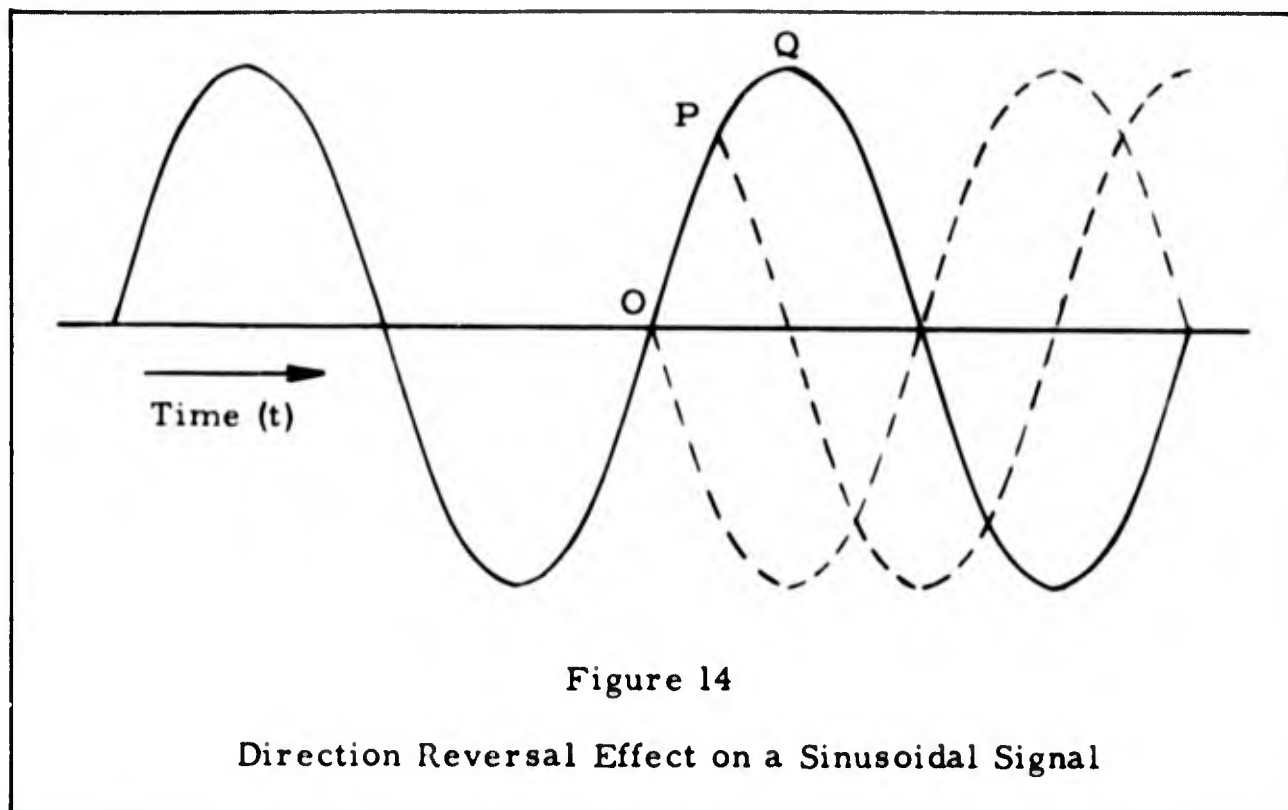
$$\begin{aligned}\tan^2 (\theta_0 + \psi) &= \tan^2 \phi + \tan^2 (\theta_0 + \theta) \\ \tan^2 (\phi_0 + \psi') &= \tan^2 (\phi_0 + \phi) + \tan^2 \theta\end{aligned}\tag{36}$$

The solution of these two equations for  $\phi$  and  $\theta$  can undoubtedly be handled by computer data processing techniques.

### Direction Sensing

For any angle measuring application where the angle variation is periodic, there will be periodic reversals in direction of angular rotation. Counting fringes is therefore not only an addition process, but must also involve subtraction whenever angular direction is reversed. Any automatic counter system which may be utilized in conjunction with the interferometer angle sensing device must be triggered to reverse the counting process each time the angular direction reverses.

Graphically the effect of rotation reversal is illustrated in Figure 14. This figure shows a sinusoidally varying intensity as a function of time or total angular movement. Reversal of direction



at any particular point will cause the intensity-time curve to retrace exactly what has preceded the reversal. Thus, if reversals occur at points such as O and P, there will be fairly sharp discontinuities in the slope of the curves. This is equivalent to a phase shift and this phase shift is effectively equal to minus twice the instantaneous phase. However, if a rotation reversal takes place at a peak or valley, such as point Q, then the phase shift is effectively zero or some multiple of  $2\pi$  and there is no way to distinguish that a rotation reversal has taken place.

Now consider the phase between two such waves which initially have a relative phase of  $\frac{\pi}{2}$  with respect to each other. Signifying the phase of one wave at the instant of rotation reversal as  $\beta$ , the phase of the second will be  $\beta + \frac{\pi}{2}$ . At reversal the phase shift of the first wave is  $-2\beta$  and of the second is  $-2\beta - \pi$ . The phases of the waves are now  $-\beta$  and  $-\beta - \frac{\pi}{2}$ , respectively, and the phase

difference is  $-\frac{\pi}{2}$ . Rotation reversal has effectively shifted the phase between the two waves from a positive to a negative value.

The next question that arises is how does one obtain two interference intensities  $90^\circ$  out of phase with each other. Basically, one portion of an interference field must have an optical path difference of  $1/4$  of a wavelength less than or greater than the other portion of the interference field. One method of achieving this is to insert in the path of one of a pair of beams which interfere, an optical plate whose thickness is such that the optical path across it is  $1/4$  of a wavelength greater than the same path in air. The possibility of using such a scheme as this depends on the ray path geometry in any particular interferometer. This will be discussed for a given interferometer geometry in the following section.

If the signals resulting from two such fields are equal in magnitude and are fed into the two sweep channels of a cathode ray tube, the resulting pattern swept by the electron beam will be a circle. If the signals are not equal in magnitude the pattern will be an ellipse. In either case the direction of rotation of the electron beam will reverse each time the phase relation changes sign or each time the angular rotation of the interferometer reverses.

Thus, the basic information to detect the direction of rotation can be obtained. The actual technique of utilizing this information in electronic counting circuits has not been investigated. Undoubtedly logic circuits can be designed to handle this problem.

### Angle Sensing Interferometer Design

A number of the theoretical aspects of the interferometer angle sensing device have been discussed thus far, some in more detail

than others. At this point the various equations can be employed to analyze a prospective angle sensing interferometer design.

Basically, the interferometer should be a rigid structure and should not require any delicate adjustments which cannot be maintained under the accelerations and vibrations of a typical sled run. Thus, the interferometer might consist of a solid optical material, such as glass or quartz, with two surfaces ground flat and parallel to each other and properly coated for the desired reflective characteristics. Low index of refraction is desired since the sensitivity varies inversely with the index. The indices of refraction of most glasses and quartz are on the order of 1.5. The index of refraction of air is very close to 1. These values will be used for subsequent calculations, although fused quartz with a refractive index of 1.457 would probably be used since it has one of the lower indices.

Consider the interferometer geometry shown in Figure 15. This geometry was chosen for maximum utilization of incident intensity. The angle  $\theta$  is chosen at  $49^\circ$  for maximum sensitivity as indicated in Figure 8. Consider the incident beam and interferometer as rectangular in cross-section. The dimensions of the beam are  $x$  and  $y$ , where  $y$  is the dimension normal to the plane of the figure.

Surface A is coated with a dielectric coating for 50% reflectivity at  $6328\text{\AA}$  over the upper part of its surface down to the line where the center rays of the beam intersect the surface. Similarly, surface B is coated with a dielectric coating for nominally 100% reflectivity over the lower portion up to the line where the refracted



of  $3 d \tan \theta'$  or 5.34 cm. This represents 60% of each surface.

Equation (16) gives a sensitivity of .1758 fringes per arc sec. or 5.72 arc sec. per fringe. With a capability of resolving one part in ten of one fringe shift, the resolution will be 0.572 arc sec. and the accuracy will be + 0.285 arc sec.

Beam separation considerations do not apply to this geometry since the situation is effectively reversed with two separate beams incident, and two fully overlapping beams transmitted. This is primarily the effect of utilizing the 100% reflective coating on a portion of surface B.

Dielectric coatings are used to reduce absorption losses and also to take advantage of the fact that dielectric reflections introduce only 0 or  $\pi$  phase shifts on reflection. If the laser polarization is oriented so that it is parallel to the plane of incidence, the transmission through the uncoated surface is almost 100%. This is because the angle of incidence of  $49^\circ$  is fairly close to the polarizing angle of  $57^\circ$ . For parallel polarization the phase shifts on reflection from the fully and partially reflective surfaces will be  $\pi$  in the dense medium and 0 in the rarer medium.

Besides the rays transmitted through the interferometer there are an equivalent set of rays reflected back from the interferometer which exhibit the interference effect at the same rate. However, this interference is  $\pi$  radians out of phase, since one less reflection in the dense medium is involved. These rays are shown incident on photomultiplier A in Figure 15 and will subsequently be referred to as the back rays. Similarly, rays incident on photomultiplier B will be referred to as the forward rays.

The intensities and phases of each of the components of the back and forward rays can now be listed.

$$\left. \begin{aligned} I_1 &= (1-r)I_0 \quad \angle 0 \\ I_2 &= rI_0 \quad \angle 2\pi + 2\pi m \end{aligned} \right\} \text{(forward rays) (37)}$$

$$\left. \begin{aligned} I_1 &= rI_0 \quad \angle 0 \\ I_2 &= (1-r)I_0 \quad \angle \pi + 2\pi m \end{aligned} \right\} \text{(back rays) (38)}$$

Using Equation (24), the resultant interference intensities of these two interference fields will be

$$\left. \begin{aligned} I \text{ (forward rays)} &= I_0 r (1-r) + 2I_0 \sqrt{r(1-r)} \cos 2\pi m \\ I \text{ (back rays)} &= I_0 r (1-r) + 2I_0 \sqrt{r(1-r)} \cos (\pi + 2\pi m) \end{aligned} \right\} \text{(39)}$$

If the two signals from photomultiplier A and B are subtracted, the resulting effective intensity signal is

$$I = 4I_0 \sqrt{r(1-r)} \cos 2\pi m \quad (40)$$

For  $r$  equal to 0.5

$$I = 2I_0 \cos 2\pi m \quad (41)$$

The DC component of the interference intensity has been effectively eliminated and the peak-to-peak interference signal is  $4I_0$ .

Instantaneously, the frequency at which  $m$  varies, provided  $\theta$  varies at an angular rate  $\omega$ , is given by  $\left| \frac{dm}{dt} \right|$  which is

$$\left| \frac{dm}{dt} \right| = \frac{1}{\lambda_0} \omega d n_a^2 \left| \sin 2\theta \left[ n_g^2 - n_a^2 \sin^2 \theta \right]^{-\frac{1}{2}} \right| \quad (42)$$

Under actual inertial platform testing, the maximum rate of change of angle for any periodic vibration depends on the amplitude and frequency of the vibration. The separate limits on each of these are 5 arc min. and 200 cps. Although these maximum conditions do not occur together, an upper limit calculation can be made by assuming that they do. The vibration can then be described by  $5 \sin 400 \pi t$  for small angles. Maximum rate of change of angle occurs when  $t = 0$  and is given by  $2000 \pi \cos 400 \pi t$ . The maximum rate of change of angle is calculated to be 6280 arc min. per sec or 1.83 rad per sec. Substituting  $\omega = 1.83$  and all the other given values into Equation (42) gives a maximum frequency of 66.2 kc. The light sensor must therefore have a frequency response of at least 66.2 kc. Photomultipliers easily exceed this frequency response.

In reality the interference fields are not stationary with respect to the photomultipliers since everything mounted on the inertial platform will rotate. The transmitted and the reflected rays move across each photomultiplier in opposite directions. Since the angles vary over a small range ( $\pm 5$  arc min.) and since the photomultipliers can be stationed quite close to the interferometer, the motion of the field should cause no difficulty. For a 10 arc min. swing and a distance of 5 cm. from the interferometer to photomultiplier, the field moves only 0.007 cm.

In order to calculate an upper limit on the range, let us assume that the photo sensors are photomultipliers of gain  $G = 10^5$ , quantum efficiency  $q = 7 \times 10^{-2}$  at  $6328 \text{ \AA}$ , load  $R_L = 10 \text{ K}\Omega$  and area  $A = 4 \text{ cm}^2$ . Using Equation (29) a radiant sensitivity of 3550 ma/mw is calculated. The equivalent peak-to-peak intensity signal was shown to be 4 times the incident intensity. Therefore,  $I'(\theta, R)$

in Equation (28) is equal to  $4I(R)$ . As a conservative estimate, assume the minimum detectable signal is equal to 1 mv. Using Equation (28),  $I(R)$  is calculated to be  $1.76 \times 10^{-9}$  mw/cm<sup>2</sup>. For a 6 mw output laser,  $I(R)/F_0 = 0.29 \times 10^{-9}$  cm<sup>-2</sup>. Referring to Figure 12 we see that in both divergence cases the maximum range far exceeds 35 kft. The range in actuality may be appreciably less than the above numbers indicate when absorption, scattering and other deleterious effects of the atmosphere are considered.

For direction sensing two interference signal  $\frac{\pi}{2}$  out of phase must be obtained. One possible method of obtaining two such signals in the design being discussed is to insert a quarter wave retarding plate in one quadrant of the incident beam.

Figure 16 shows the placement of such a plate. The interference signal detected by photomultiplier 1 will be  $\frac{\pi}{2}$ . The effective thickness of the plate will vary slightly as the angle of incidence varies. Since it varies proportionally to the cosine and the rate of change of the cosine is very low for small angles, this effect will not be significant. With the placement of the two photomultipliers indicated in Figure 16, a convenient value for  $y$  is  $y = x$ .

The results of all the foregoing design calculations are tabulated in Table I. These values show that all specifications for the inertial platform testing application can be met.

**BLANK PAGE**

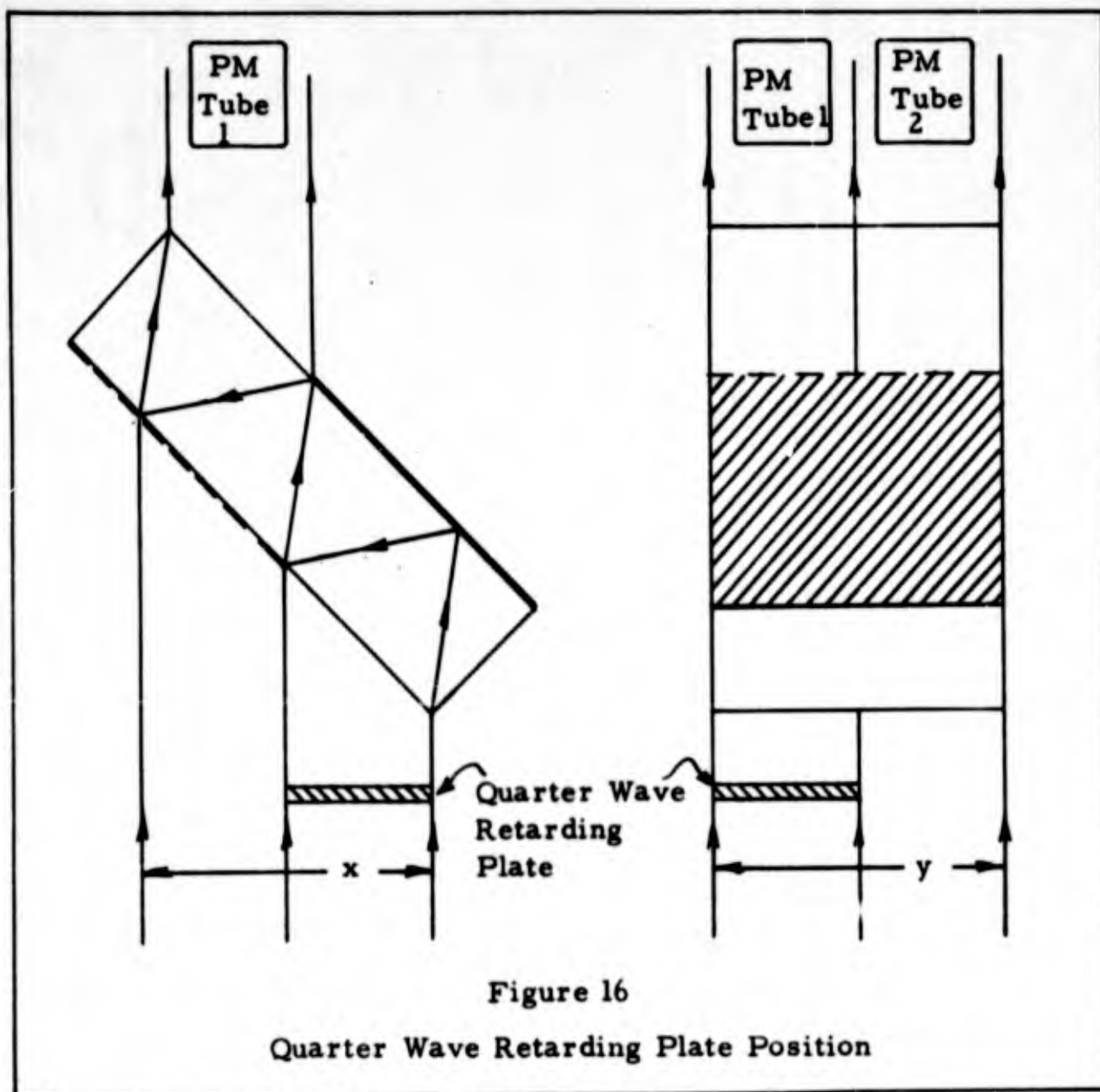


Figure 16

Quarter Wave Retarding Plate Position

TABLE I

## Interferometer Design Specifications

Interferometer Optical Material	Quartz
Index of Refraction at 6328A°	1.457
Interferometer Gap Dimension	3 cm
Angle of Null Position	49°
Sensitivity	5.72 arc sec. per fringe
Estimated Accuracy	$\pm 0.285$ arc sec.
Effective Peak-to-Peak Interference Signal	$2I_0$ ( per PM tube)
Angular Range	exceeds $\pm 5^\circ$
Maximum Signal Frequency	Less than 66.2 kc
Nominal Reflectance of Partially Coated Surfaces	front surface - 50% back surface - 100%
Aperture or Beam Dimensions ( normal to beam)	4.59 x 4.59 cm;
Interferometer Dimensions	8.75 x 4.59 x 3 cm.
Flatness and Parallelism	$\frac{1}{10} \lambda$ ; < 0.5 arc sec.

#### IV. Experimental Investigation of an Angle Sensing Interferometer

The primary purpose of the experimental portion of this study was to set up and operate an interferometer angle sensing system in the laboratory, and measure fringe count and sensitivity as a function of angle in order to compare the results with the values indicated by theory. Other objectives were to observe the nature of the interference pattern in order to determine the degree of beam collimation and interferometer surface flatness and parallelism required to obtain full field interference.

##### Experimental Approach

The interferometer to be tested is placed on a rotatable table and in the beam of the laser. Interferometer adjustments when necessary are made according to the interpretation of the interference pattern. The angle of incidence between the light beam and the interferometer can be accurately measured with an autocollimating telescope. The interference is detected with an optical sensor and the signal fed to a strip chart recorder. The intensity variations can be observed and the fringes counted by observing the resulting trace. The fringe count is considered the independent variable and angle readings are taken at various intervals of fringe count as the interferometer is rotated.

##### Description of Apparatus

Laser Light Source. The laser light source used was a Perkin-Elmer /Spectra-Physics continuous wave gas laser emitting in the visible at  $6328\text{\AA}$  (Figure 17). The laser is designated as Model 115



Figure 17

Helium - Neon Laser

and is of the Helium-Neon type. The laser system consists of two units, one containing the plasma tube, mounting frame, resonator reflectors and the reflector adjusting mechanism, the other containing the DC power supply and the radio frequency oscillator. Nominal resonator length is 100 cm.

Maximum power output for single mode operation is about 6 milliwatts. The output of the laser is plane polarized due to the Brewster angle window constructed at each end of the plasma tube to reduce transmission losses.

The laser can be operated with two flat mirrors, two confocal spherical mirrors, or one flat and one spherical mirror. Least beam divergence results when the flat mirrors are used but adjustment is more critical and less stable. The hemispherical configuration (one flat, one spherical) results in a beam divergence of approximately 80 arc sec., but is not as critical in adjustment. The laser used was in the hemispherical configuration. Frequency stability is specified as  $6328\text{Å}^{\circ}$  with  $\pm 0.02\text{Å}^{\circ}$  and the beam diameter at the end of the resonator is approximately  $1/2$  cm.

Rotation Platform. As a matter of convenience a spectrometer manufactured by the Wild Instrument Co. and shown in Figure 18, was available and has several features which were used in the experiments. One of these features is that it has a small (about 5" diameter) circular table which can be adjusted to a level position by three screws and rotated about a vertical axis, either freely by hand or by a driving screw. A swing of  $3^{\circ}$  is possible with screw rotation. After this degree of rotation the screw can either be rotated in the opposite direction so that the table retraces its rotation, or the driving screw can be disengaged and reset by

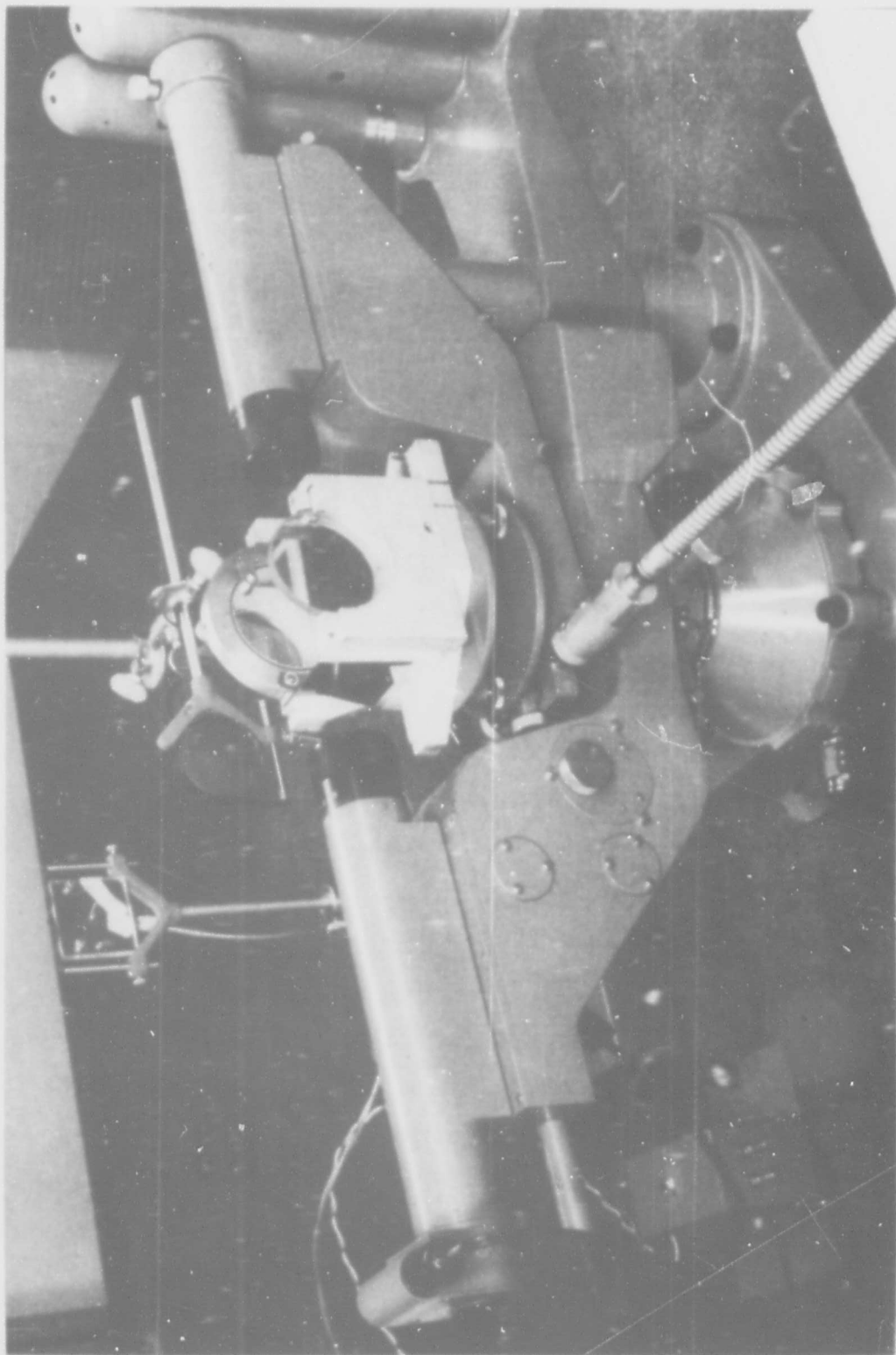


Figure 18  
Spectrometer Rotation Table and Autocollimating Telescope

**BLANK PAGE**

rotation in the opposite direction without any further rotation of the table. By engaging the drive screw again, the rotation of the table can be continued for another  $3^{\circ}$ . While the screw is disengaged the table can be rotated to any position. This rotating table made a convenient platform for the interferometer so that alignment and rotation operations could be conveniently accomplished.

Autocollimating Telescope. A second feature of the Wild Spectrometer is that it has an autocollimating telescope which can be aligned normal to any reflective surface mounted on the platform. This telescope is mounted so that it can rotate about the same axis as the platform. The angle this normal makes to any other reference normal can then be directly read from a scale. The alignment of the telescope is accomplished by rotation of the telescope until a fixed hairline coincides with an image of the same hairline projected out of the telescope and reflected back into the telescope by any convenient flat mirror stationed on the platform.

The accuracy of this device is theoretically 0.2 arc sec. However, the accuracy is certainly a function of operator technique and the average accuracy is probably more like 0.5 arc sec.

The autocollimating telescope is located in the left-hand arm of the spectrometer shown in Figure 18.

Interferometers. Initially, the objective was to test the two basic interferometer configurations described below. However, final testing and data were obtained for only one of these configurations due to time limitations resulting from the fact that the time required for preliminary qualitative experimentation and development of experimental technique ran higher than expected. Both basic

interferometer configurations will be described since preliminary experimentation was done with both configurations.

The configuration which was tested and for which final data was obtained, consists of a solid piece of optical material with two surfaces ground flat and parallel to each other. These surfaces are made partially reflective so that they act as beam splitters. Since the two surfaces are fixed with respect to each other, the structure is rigid and there is no need for parallel adjustment making this configuration particularly applicable to the inertial platform testing application. This configuration will subsequently be referred to as the solid gap interferometer.

The optical flat utilized was made of fused quartz with both surfaces flat to  $1/20$ th of a wavelength over the diameter and parallel to less than one arc sec. The flat has a nominal diameter of 5 cm. and a nominal thickness of 1.25 cm. Since the thickness determines the sensitivity of the device it must be known quite exactly for the specific optical flat used. The measured value of this thickness was 1.2345 cm.

The optical flat was mounted in a holder which could be clamped to the rotation table of the spectrometer. The flat, holder and table are shown in Figure 19. The holder is made of aluminum and consists of a base and a vertical mount for the optical flat. The vertical mount is bolted to the base with two bolts. This base can then be clamped to the table with the bar clamp visible in Figure 19.

The vertical holder for the flat has a circular hole with an internal flange so that the circular flat can fit loosely in the hole up to the flange. Felt rings are used to cushion the flat against

**BLANK PAGE**

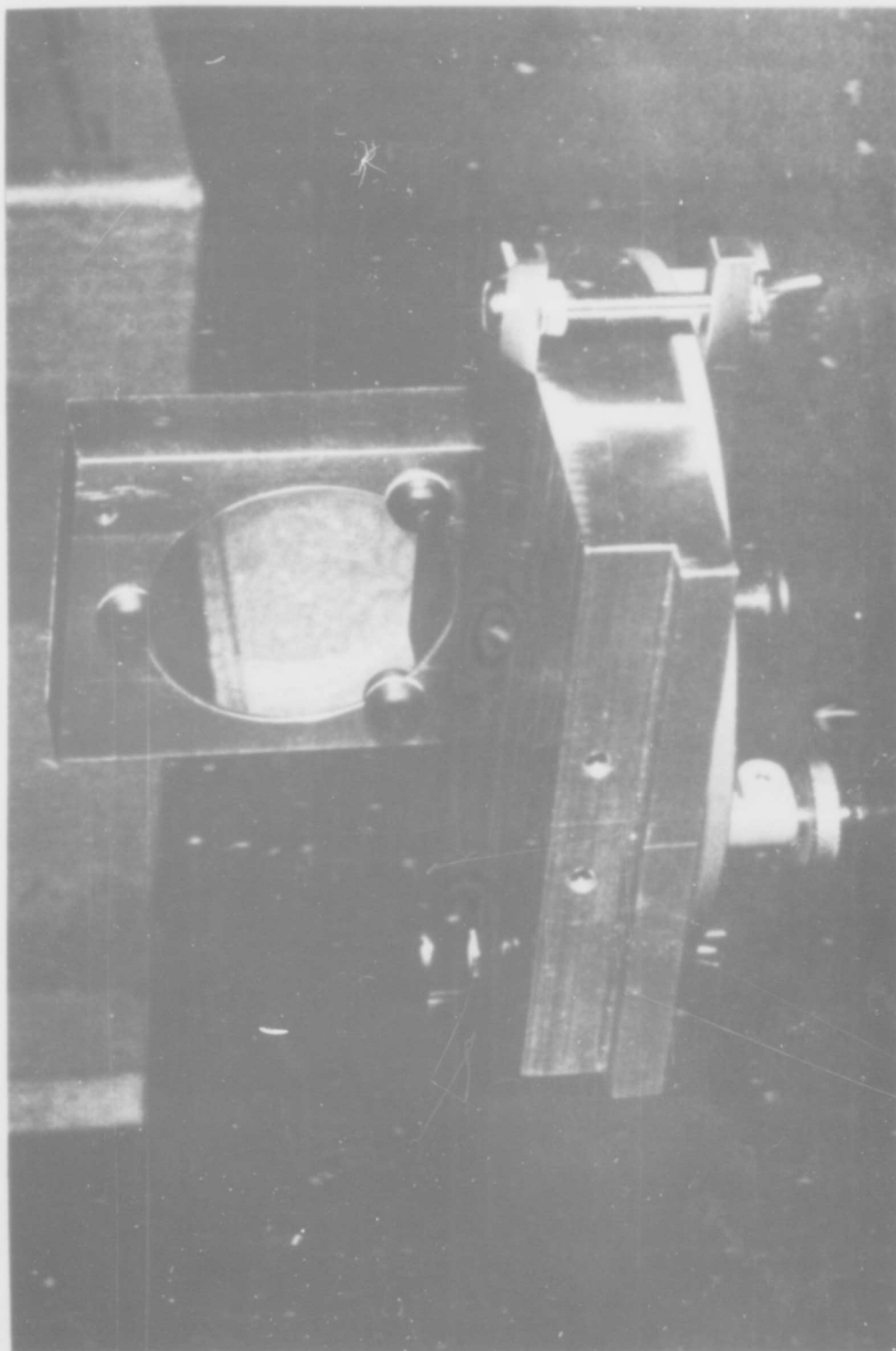


Figure 19  
Solid Gap Interferometer

the flange. The flat is held in the holder and against the flange by three rubber washers fastened with screws to the vertical mount and pressing against the edge of the flat. The flat has one surface coated to 60% reflectivity and the other surface uncoated.

The flat described above was one of a set of two identical flats which made up the second interferometer configuration. This configuration only required one surface of each flat to be coated. One of these flats was to be used in both configurations and its second surface was to be coated if necessary for the solid gap interferometer. However, sufficient interference intensity was observed with the second surface uncoated for the purpose of laboratory experimentation. This uncoated surface has a reflectivity of about 4%.

The second interferometer configuration consists of two optical flats with one surface of each coated with a thin aluminum reflective coating. These flats are situated so that the coated surfaces face each other, and so that they can be adjusted parallel to each other. The space between the reflective surfaces is occupied by the atmosphere. This configuration will subsequently be referred to as the air gap interferometer.

Two air gap interferometers were actually constructed. They are both basically the same except that in one case the base and optical flat holders were constructed of hardwood while in the other case the material was aluminum. The wooden model is shown in Figure 20 and will not be described any further since it did not prove satisfactory from the standpoint of rigidity.

The aluminum model is shown in Figure 21. It is essentially the solid gap interferometer with an additional vertical holder and optical flat. The second optical flat is identical to the optical flat described above. The second vertical holder is of special

**BLANK PAGE**

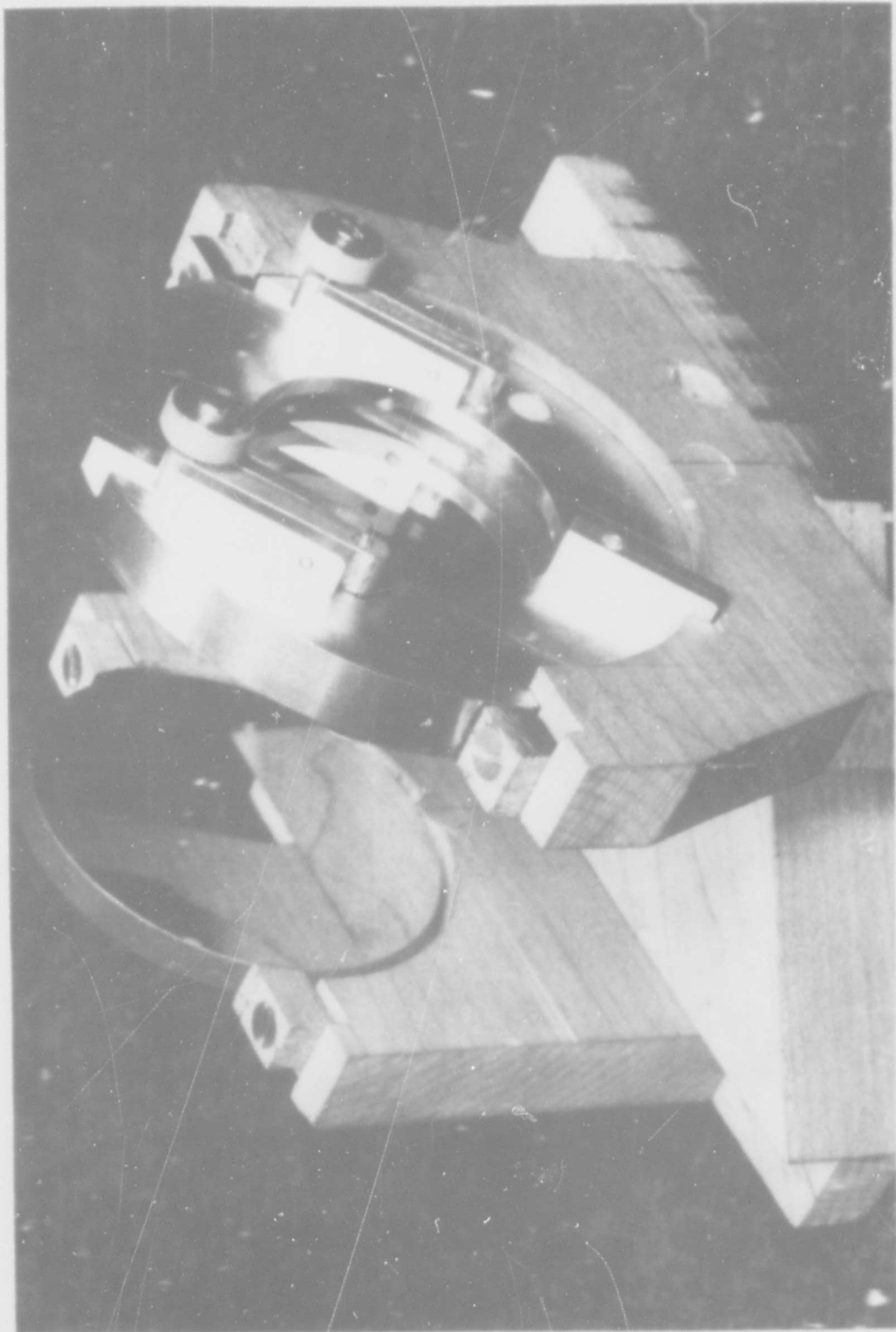


Figure 20  
Air Gap Interferometer (Wood Construction)

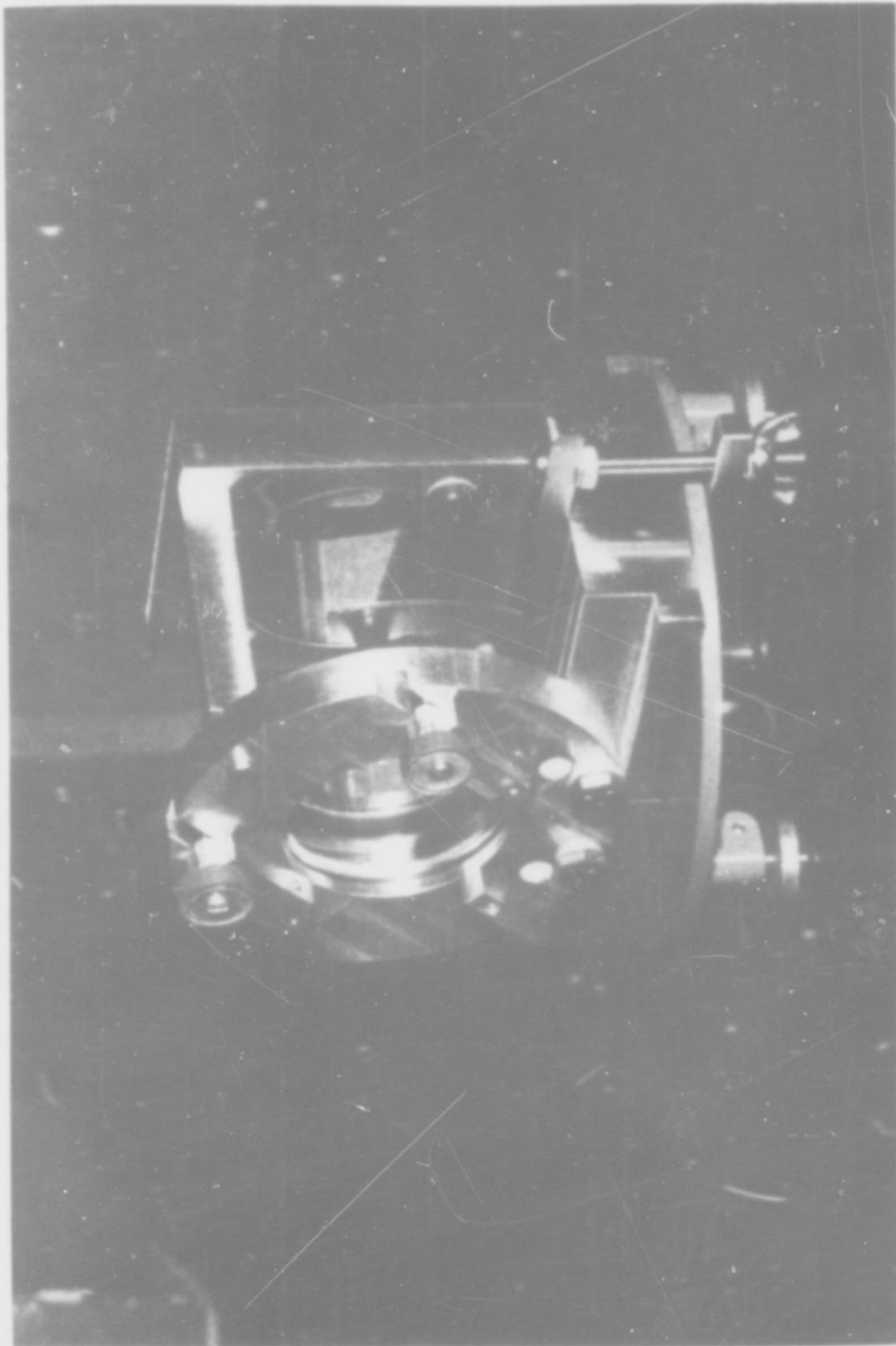


Figure 21  
Air Gap Interferometer (Aluminum Construction)

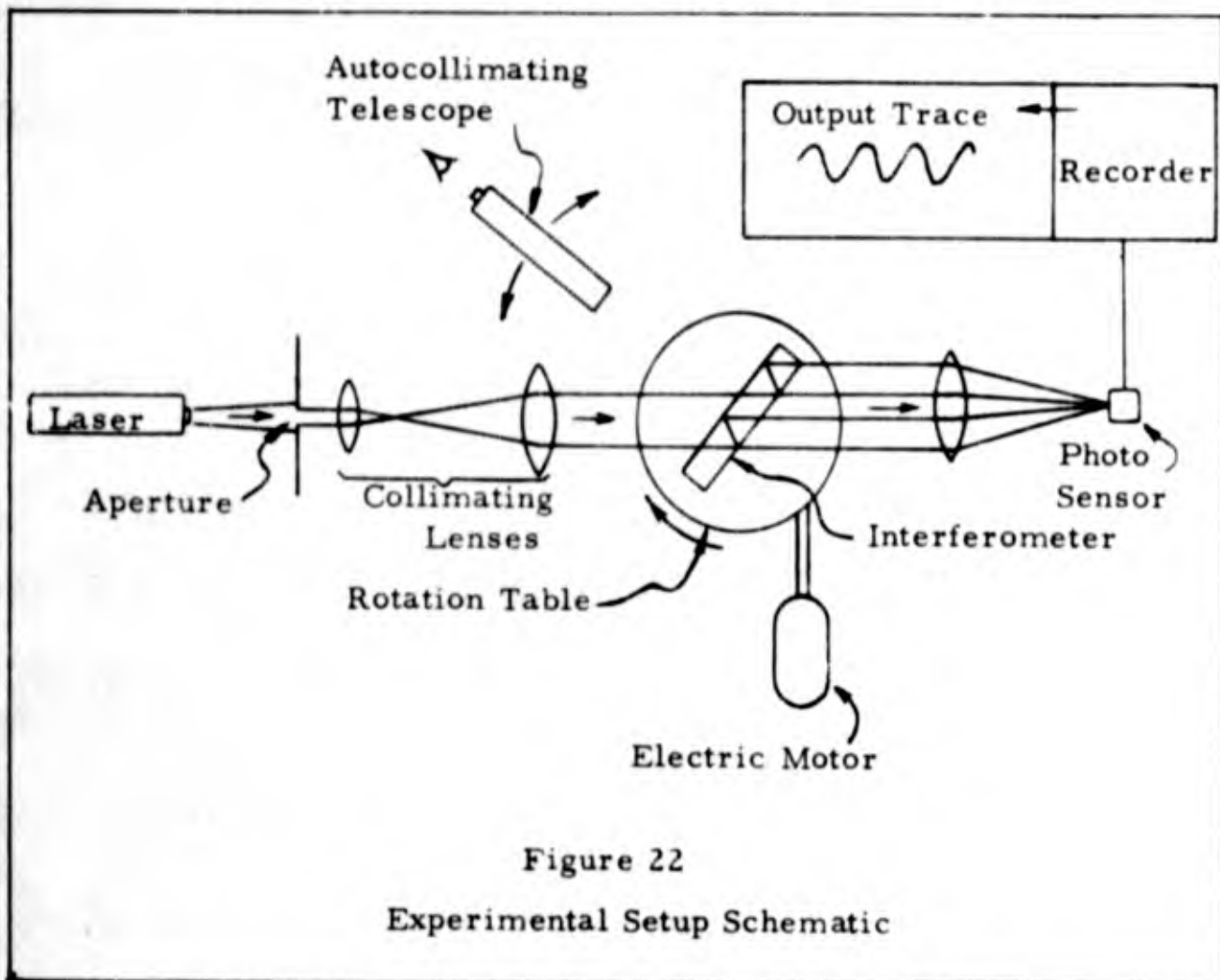
**BLANK PAGE**

design to provide for precise adjustment of the tilt of the optical flat. Like the first vertical holder, it is bolted to the base with two bolts. In addition, a horizontal bar brace has been added to bridge the gap between the top of the two holders for extra rigidity.

The adjustable holder was originally designed for an optical flat of larger diameter and smaller thickness than those finally used. Therefore, an adaptor ring was designed for the optical flat primarily to increase its diameter. This adaptor ring is not visible in Figure 21. The adjustable holder is circular in shape and has a circular hole with an inner flange to hold the optical flat/adaptor ring assembly.

The optical flat/adaptor ring assembly is held in place by six small teflon hemispherical knobs, three on each face of the adaptor ring. These knobs press against the adaptor ring under spring tension at locations exactly opposite each other on both sides of the flat. They are located in quadrature near the outer circumference of the adaptor ring in three out of the four quadrants of the circle. One opposing set of knobs is fixed while one of each of the other two opposing sets is attached to a small level arm which is actuated by finely threaded screws. Rotation of the screw tilts the lever and the optical flat. The two levers provide very finely controlled pitch and yaw tilt of the optical flat. The screws and level arms are visible in Figure 20 and 21.

Optical Sensor. A Texas Instrument LS-400 , NPN Silicon Planar Photo Device was utilized to detect the interference intensity variations. Its spectral response peaks at 0.9 microns and it has a relative response of 42% at 0.6328 microns. The rise and fall times



are specified as 1.5 and 15  $\mu\text{sec.}$ , respectively. At  $9 \text{ mw/cm}^2$  incident intensity at .7 to 1.0  $\mu$ , the light current is typically 3 ma.

### Experimental Setup

Figure 22 shows a schematic of the experimental setup. The view of the setup is from the top.

For initial experiments the laser was mounted on a tripod stand with azimuth and elevation adjustment capability. The stand was positioned approximately 35 feet from the interferometer. Laser, stand and RF exciter unit are shown in Figure 17.

The laser was adjusted so that its beam was parallel to and centered above the two guide rails of an optical bench. On the end of the optical bench toward the laser, two lenses and an aperture

were set up to collimate the beam. A 1/16 inch aperture was used to select the central rays of the beam.

The interferometer itself is mounted on the rotation table of the Wild spectrometer which rests on a micro-flat table located at the other end of the optical bench. The spectrometer in this setup is at the proper height with respect to the optical bench guide rails for convenient alignment.

Behind the interferometer a lens was set up so that the laser beam could be collected and focused on an LS-400 light sensor. The LS-400 was biased with approximately 16 volts and the output fed through a 10 K $\Omega$  load to an Offner strip chart recorder.

Rotation of the spectrometer table was accomplished by rotation of the driving screw with a reversible electric motor. The speed of the motor was controlled by a variable transformer and reduced by means of a reduction gear. A flexible shaft and friction clutch were used to mechanically couple the motor unit to the driving screw. Thus, as the screw reaches its stop, the clutch slips and prevents jamming of the screw at the stop. Figure 23 is a photograph which shows the drive unit, variable transformer, spectrometer, interferometer, lens, sensor, and recorder. The sensor itself is barely visible in its phenolic plastic holder which is located just above the right portion of the spectrometer and aligned with the front right edge of the recorder cabinet. An overall view of the setup is shown in Figure 24 with the laser in the far left background.

The setup used to obtain the final data was basically as described above. The laser stand did not prove to be a rigid enough support for the laser due to the loose fit of various screws and linkages used to provide elevation and azimuth control. The laser

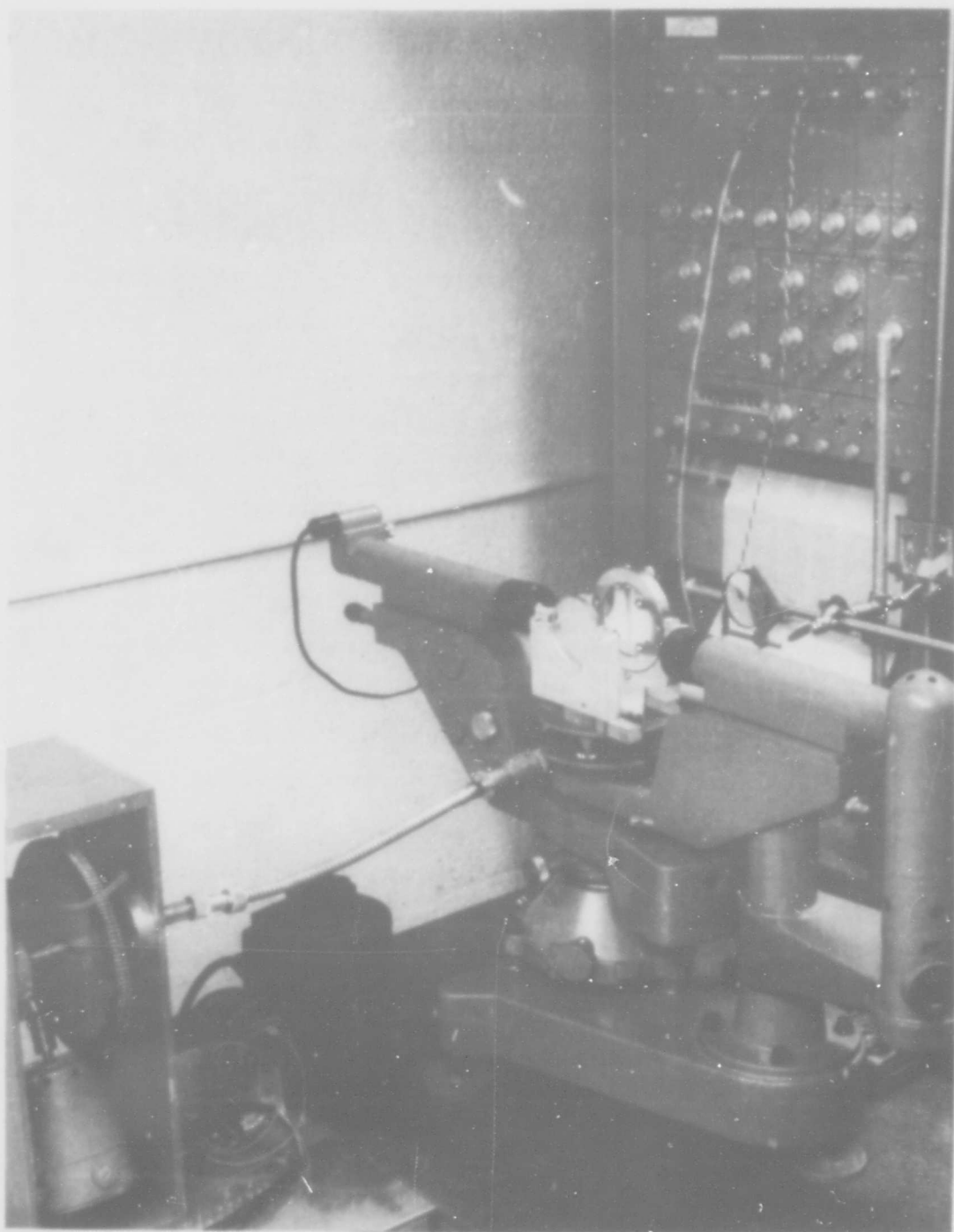


Figure 23  
Test Apparatus

**BLANK PAGE**

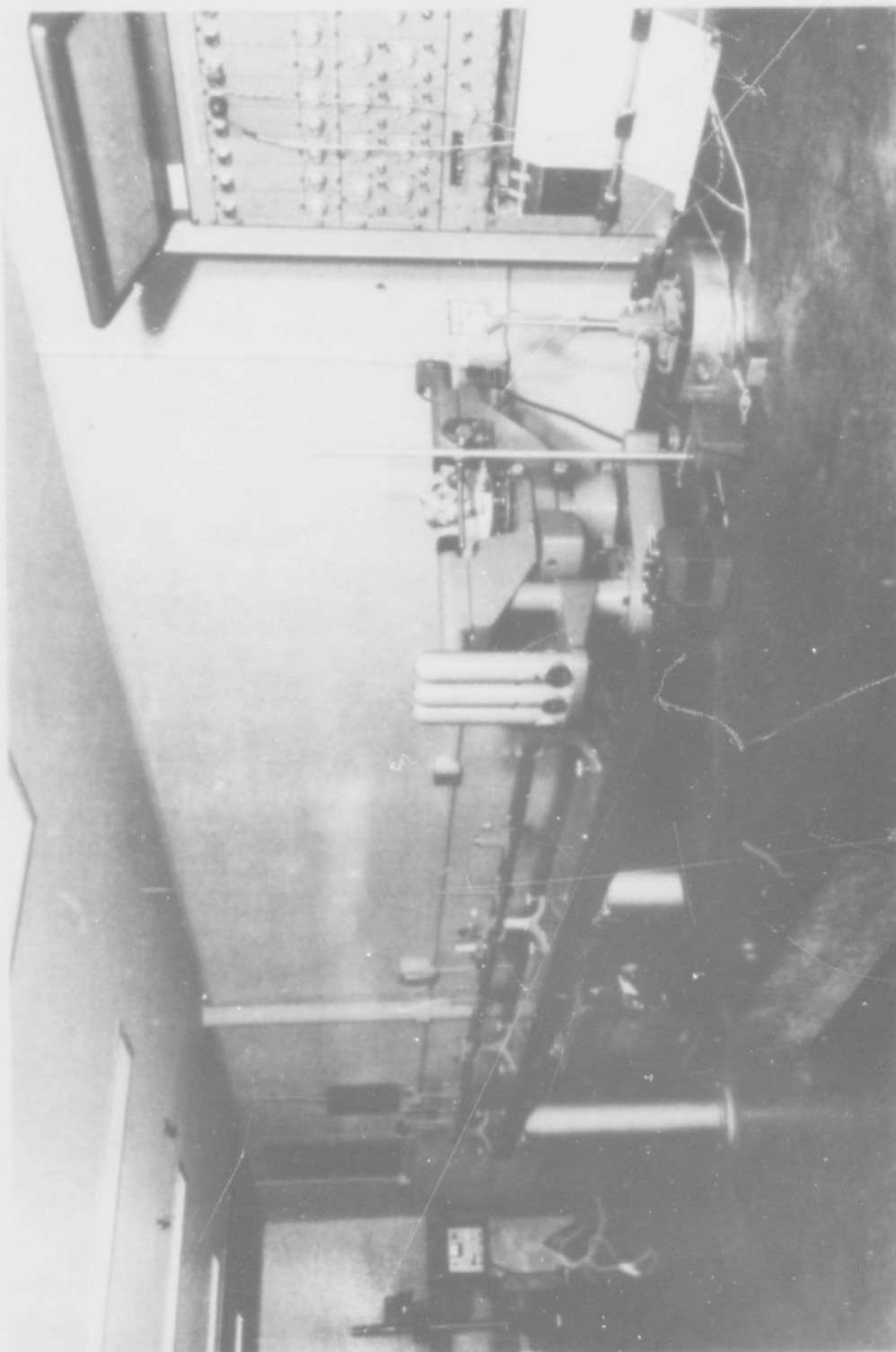


Figure 24  
Overall View of Experimental Setup

was subsequently mounted on the optical bench at a position about 12 ft. from the interferometer.

Other minor changes included the positioning of the motor unit on the opposite side of the spectrometer. (The drive screw which rotates the table can be driven at either end.) The collecting lens and sensor were also subsequently mounted on optical bench guide rails set up on the micro-flat table. This allowed more convenient alignment of lens and sensor.

### Experimental Technique

Initial experimentation involved checking out the tilting mechanism for parallel adjustment of the air gap interferometer flats, and observation of the effects of beam parallelism and interferometer parallelism on the interference pattern. The techniques employed for this early experimentation are straightforward. The interferometer is inserted in the beam and the parallel adjustment screws turned to adjust the flats in and out of parallelism. The resulting interference pattern is observed on some convenient target.

The divergence of the laser beam is decreased by passing the beam through two lenses (one of short focal length and the other of long focal length) stationed a distance apart equal to the sum of the focal lengths. The divergence of a beam passing through these lenses from the side of the shorter focal length lens, will be decreased by the ratio of the small to the large focal lengths which was about 1 : 6. The diameter of the beam will be increased by the reciprocal of this ratio.

Two techniques were considered for obtaining fringe count versus angle data with the setup described in detail in the previous section and shown schematically in Figure 22.

The first technique consists of the following. The interferometer is aligned normal to the laser beam by rotating the table and adjusting the level of the table until the beam is reflected directly back into the laser. This procedure results in normal alignment to within about  $\pm 20$  arc sec.

The adjustable flat is then adjusted in tilt so that the two reflective surfaces are parallel. (The solid gap interferometer does not require this adjustment.) This adjustment is made by observing the multiply reflected beams emerging from the interferometer and the interference pattern. Rough adjustment is first obtained by aligning the multiply reflected beams. Fine adjustment is then made by observing the interference pattern. Horizontal line fringes indicate additional vertical adjustment is required. Vertical line fringes indicate additional horizontal adjustment is required. The wider the spacing between these fringes the less adjustment required. Parallelism is finally obtained when the beam spot is uniform in intensity provided the beam is parallel. If the beam is not sufficiently parallel a few circular fringes will be observed and the interferometer parallelism adjustment is reached when these rings are made concentric with the beam cross section. Lack of a high degree of flatness on the reflective surfaces will cause distortion of the interference patterns.

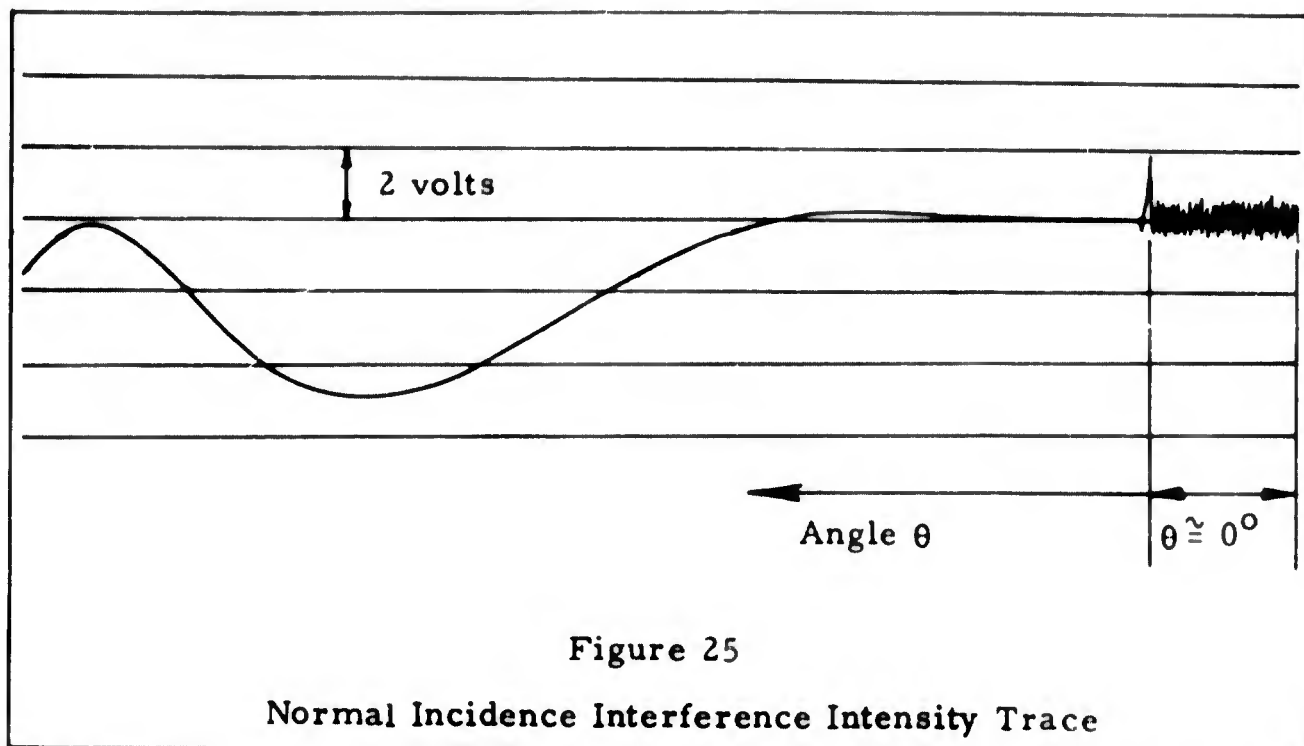
The beam emerging from the interferometer is collected and focused by a lens onto the sensor whose output is fed to the recorder.

The scale of the autocollimating telescope is set so that a reading of zero is obtained when the interferometer is normal to the laser beam. The interferometer is rotated to some small negative angle and the telescope is left at the zero reading position. At this point the run can commence.

The table and interferometer are now rotated slowly by the motor and the recorder begins to record the intensity variations. As the table reaches the normal position again the telescope hairlines approach each other. At the instant they cross a shorting switch is momentarily triggered so that the strip chart recording is marked with an abrupt discontinuity. This shorting switch can be connected directly across the sensor output or across any convenient voltage fed to an adjacent channel of the recorder. As the table continues to rotate the telescope is realigned at some angle increment from its previous position. The hairlines once again cross and the recorder is marked. This procedure is repeated as rotation continues and results in a recording of intensity variations marked at each predetermined angular position.

The process described above can only proceed for an angular swing of  $3^{\circ}$ . When this point is reached the table rotation must be stopped and the driving screw reset. The table is then aligned to the last angular position of the telescope and the run is continued for another  $3^{\circ}$ .

The basic difference between the above technique and the second technique to be described is the manner of conducting the run and taking data. The identical procedure is followed up until the point of setting the interferometer at some small negative angle. Whereas



the above technique sets the angle as the independent variable, the technique to be described sets the fringe count as the independent variable.

Before proceeding on to describe this second technique, a brief discussion of the interference intensity trace at normal incidence is in order since one property of this trace will be utilized.

As the interferometer rotates the interference intensity trace has a sinusoidal shape. The frequency of this trace decreases as the normal position is reached. Close to the normal the trace levels off to some level on or between the maximum and minimum levels. This essentially means that the frequency of the trace is decreasing to zero and instantaneously must be zero at the normal position. At angles past the normal position the trace is a mirror image of the preceding trace. However, at the normal position the trace exhibits a sudden jump or spike of intensity. A sketch of the trace and spike is shown in Figure 25.

The spike can probably be attributed to the fact that additional reflections from the laser end mirrors are cast on the sensor when the beam is reflected directly back from the interferometer to the laser . If the interferometer is stopped at the normal position, the interference intensity trace fluctuates fairly rapidly about the level reached. The cause of this fluctuation is not known at this time but is probably a result of the interaction of the reflected beam with the laser resonance. The observation of this intensity spike as the interferometer passes through the normal position can be used as an indication of the normal alignment of the interferometer.

The second technique commences with table rotation from the negative angle position. The trace is observed and the rotation stopped when the spike occurs. The angular position is then measured and recorded. This reading corresponds to a zero reading which must be subtracted or added to all subsequent readings. The table is rotated again and the fringes counted by observing the recorder trace. At some predetermined increment of fringe count the rotation is stopped and the angle read and recorded. This procedure is then repeated to cover any angular range desired. As before, the driving screw must be reset every  $3^{\circ}$ .

The technique for measuring sensitivity results in an average sensitivity determination . This average is taken over some small number of fringes. The procedure is to set the table at some angular position near the angle at which the sensitivity is to be measured and at a minimum or maximum intensity level. A reading is then taken and the table is rotated. After the predetermined fringe count the rotation is stopped and another reading taken. The sensitivity is then calculated as the ratio of the number of fringes counted to the difference in the two angle readings.

### Experimental Results

Initially, the objective was to test and collect data on both the air gap and solid gap interferometers. As the preliminary experimentation proceeded it became obvious that only one configuration could be tested within the time limitation. Since the solid gap configuration is more applicable to the inertial guidance system testing problem the solid gap interferometer was tested. Five runs were completed in which the fringe count and angle were recorded over a range of  $0^{\circ}$  to approximately  $20^{\circ}$  utilizing the technique wherein the fringe count is the independent variable and angular readings are taken under static conditions.

The procedure of marking a recording as a pair of hairlines come into coincidence requires the operator to estimate the exact moment of this coincidence, and to press the shorting switch to mark the recorder. These two operations are sources of error since the moment of coincidence is fleeting and reaction time delays are involved in actuating the shorting switch.

The procedure of stopping the rotation and then taking an angle reading allows the operator to take as much time as desired to align the hairlines and subsequently to analyze the trace and determine the fringe count. A series of trials were made taking repeated readings of the same angle by both methods. The spread of the readings using the static hairline alignment procedure was 0.4 arc sec. while the spread using the dynamic hairline coincidence method was several arc sec. Thus, the static alignment procedure was found to be more accurate.

The device tested was not an optimum design from the standpoint of ray path geometry, dimensions and reflective coating. A more

nearly optimum design was developed theoretically in Section III. The interferometer tested was chosen primarily from the standpoint of availability (the optical flat utilized was an off-the-shelf item).

Interference Pattern. The beam entering the interferometer was about 1/2 inch in diameter after having gone through the two collimating lenses. The interference pattern observed at normal incidence was visually quite uniform in intensity. This indicated that the beam collimation, optical flat parallelness and flatness were within the requirements for full field interference at the normal incidence position. At larger angles of about  $20^\circ$ , the interference region showed several fringes of irregular shape indicating that a higher degree of flatness and beam collimation is desirable for larger angles. The operation of the interferometer was satisfactory at these angles in terms of providing a fairly strong peak-to-peak signal.

Interference Intensity Signal. Typical traces are shown in Figure 26. Figures 26 a, b, and c are traces in the neighborhood of  $0^\circ$ ,  $10^\circ$ , and  $20^\circ$ , respectively. The traces show that the slope is initially zero which means zero sensitivity at  $0^\circ$  as expected. As angle increases, the trace gradually begins to fluctuate between a maximum and a minimum in a sinusoidal manner. The frequency of the signal gradually increases with angle indicating an increase in sensitivity. This continually increasing frequency is illustrated qualitatively by the three traces of Figure 26. The number of cycles per unit run of the strip chart is not necessarily proportional to the frequency of the interference signal since the rate of rotation of the interferometer table had to be gradually reduced as the frequency increased.

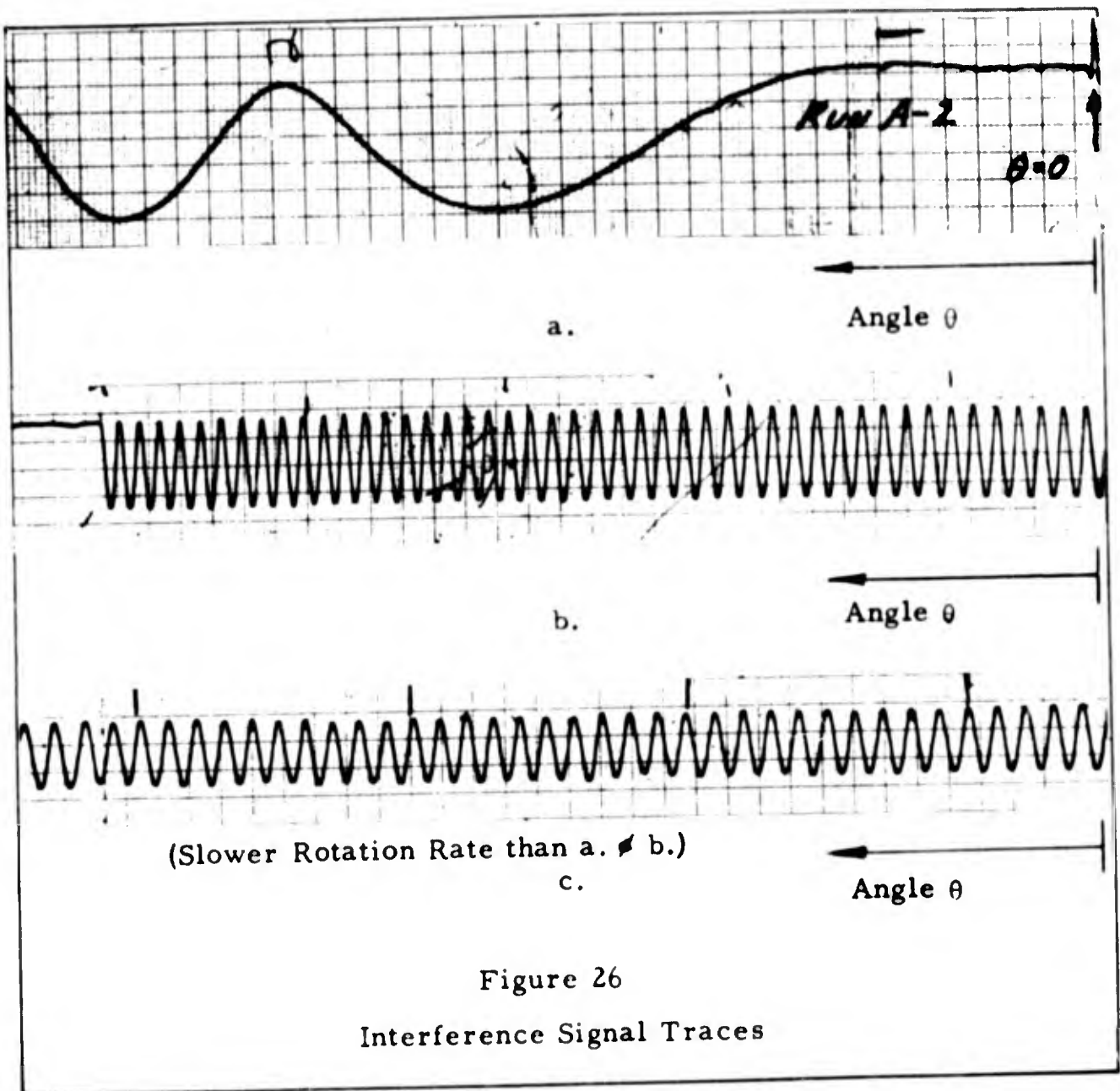


Figure 26  
Interference Signal Traces

The laser output power was typically 1.0 mw for each of the five runs. The peak-to-peak voltage recorded varied slightly from run to run. This was probably due to variations in the alignment of the collecting lens and sensor. A typical run gave a signal of 5.8 volts at normal incidence, 3.2 volts at 20° and 1.4 volts at 45° (the signal in the neighborhood of 45° was recorded only to observe the quality of the signal). This gives a signal reduction ratio of 55% at 20° and 24% at 45°.

The signal reduction with angle is primarily due to beam separation with accompanying decrease in beam overlap area.

Fringe Shift Effect. One effect was observed during the course of the five runs which was not anticipated. The normal incidence interference intensity was observed to slowly shift relative to the maximum and minimum intensity levels.

With an interferometer consisting of a single optical flat with two fixed parallel surfaces, the stability of the interference pattern was expected to be quite high. This does not mean the shifts due to laser output shifts should not occur, but these shifts equally affect the maximum and minimum levels and thus cannot affect relative levels.

The effect discussed can best be demonstrated by the actual traces obtained near normal incidence for each run. These are shown in Figure 27. For the last three runs normal incidence traces were taken before and after each run. Differences in peak-to-peak amplitudes, DC levels, and rate of signal changes from trace to trace are not significant since they are due to laser output shifts, sensor alignment shifts or rate of rotation shifts. What is significant is that the normal incidence levels marked by the spikes do not always fall at the same relative level between the maximum and minimum. The first two traces show little relative shift and the normal incidence level is near the maximum level. The third trace shows the normal incidence level adjacent to a minimum and half-way between a maximum and a minimum before the run, and at almost the same level after the run but adjacent to a maximum. The fourth trace likewise shows a relative shift before and after the run and with respect to the other traces. The fifth trace shows

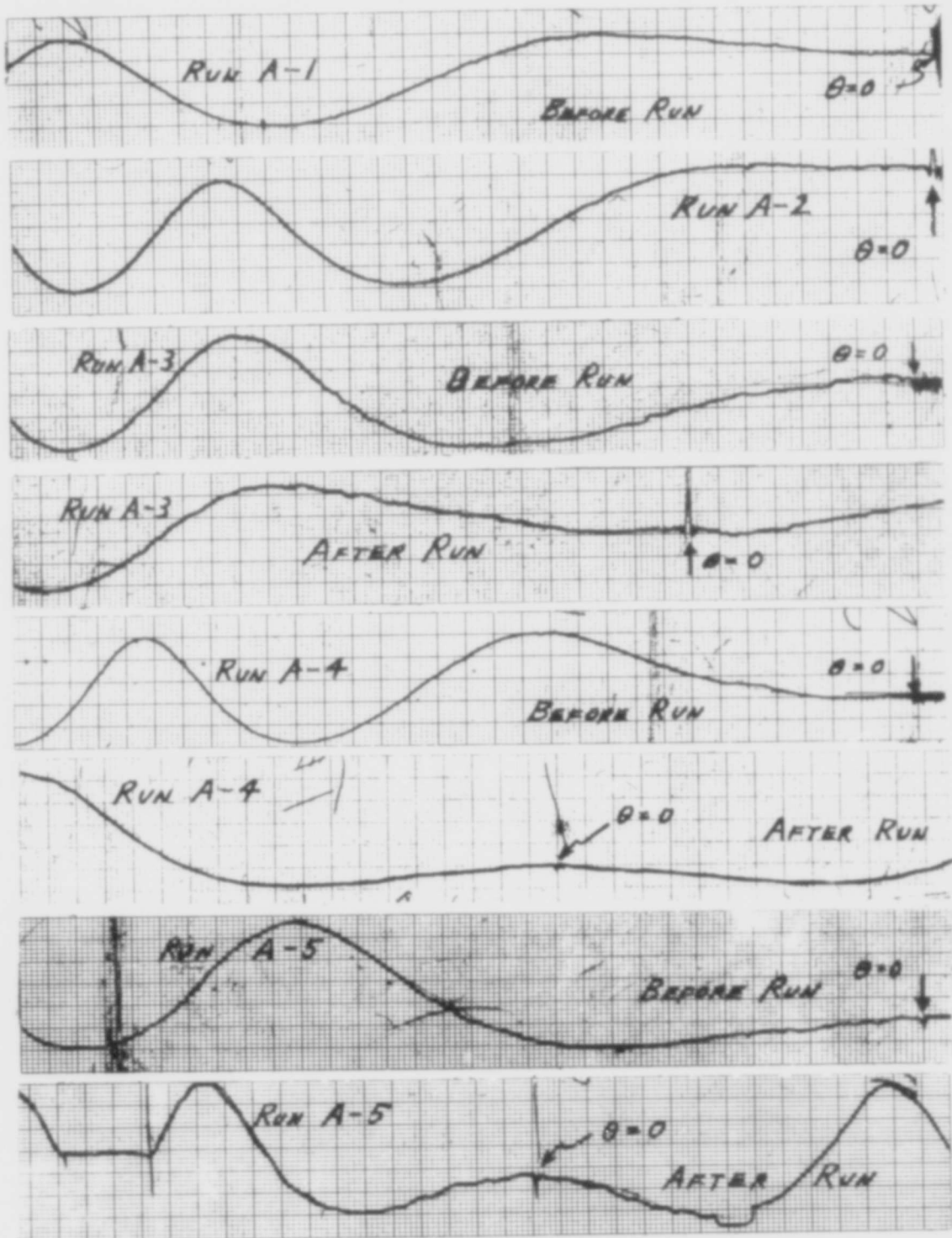


Figure 27

Near Normal Incidence Traces

an insignificant shift from before the run to after the run, but shows a relative shift with respect to the other traces. These shifts can be described as phase difference shifts between the interfering rays.

The traces of Figure 27 show an overall phase difference shift of at least  $1.4\pi$  radians or 0.7 wavelengths. These phase difference shifts were observed to occur fairly slowly. The duration of a typical run was about 2 hours. No significant shifts were observed over durations of about one-half hour during several observations.

The intensity level of the interference region for truly normal incidence is determined by the following factors.

1. The intensity incident on the interferometer.
2. The distance between the reflective surfaces.
3. Phase shifts introduced on reflection.
4. The wavelength of the radiation in the atmosphere adjacent to the interferometer.

As discussed above the incident intensity level affects all points in the near normal trace proportionally, and therefore cannot account for the effect observed.

The distance between the reflective surfaces is fixed except for temperature effects of expansion and contraction. Fused quartz has a very low coefficient of expansion ( $0.4 \times 10^{-6}$  cm cm<sup>0</sup>C). Temperature of the room in which the experiments were performed was monitored with a Brown 24 hour temperature recorder. Subsequent examination of the 24 hour record indicated maximum temperature changes of 4° F at about 70° F. With such a temperature variation the thermal expansion effect can only account for  $0.14\pi$  phase shift.

The phase shifts introduced on reflections inside the interferometer should be constant at normal incidence for any given interferometer.

Thus the effect can only be a constant effect and cannot account for the shifts observed.

The wavelength in the medium in which the interferometer is immersed will of course affect the ratio of the optical path difference to the wavelength. It is this ratio which determines the relative level of the normal incidence interference intensity. The wavelength in the medium depends upon two factors, the vacuum wavelength of the radiation and the index of refraction of the medium. The index of refraction of air is very closely equal to unity but is slightly dependent on the relative humidity and density of the air. The relative humidity at Holloman AFB is normally quite low so that we can probably assume dry air. The density then is a function of temperature and pressure. Maximum pressure variations during the times of the runs were about 0.45 in.Hg. An empirical equation relating the index of refraction of air to the pressure and temperature is (Ref 3: 13-2)

$$n_a = 1 + 10^{-6} \frac{P}{T} \left( 77.6 + \frac{.584}{\lambda_o^2} \right) \quad (41)$$

Where P is in millibars, T is in degrees Kelvin and  $\lambda_o$  is in microns. Referring to Equation (9),  $n_a^2$  appears as a multiplier of  $\sin^2 \theta$ , and the fringe count or phase index is proportional to  $n_g^2 - n_a^2 \sin^2 \theta$ . At exactly normal incidence  $\sin \theta = 0$ , and therefore,  $n_a$  has no effect. At  $\theta$  equal to a small angle (such as 20 arc sec. which is the alignment accuracy)  $n_g^2$  is very much greater than  $n_a^2 \sin^2 \theta$  and therefore,  $n_a$  has negligible effect on the phase index m. The variation of  $n_a$  seems a highly unlikely cause of the observed fringe shift.

The vacuum wavelength changes if the laser shifts in frequency. A laser stability of less than  $\pm .02 \text{ \AA}^0$  is specified for the laser used.

This amount of a wavelength shift could account for a normal incidence phase shift of  $.75 \pi$ . The combined effect of temperature expansion and frequency shift in the worst case can account for up to  $.84 \pi$ .

There are other possible effects on the normal incidence phase that will be discussed briefly. Considering only the effects already discussed leads to numbers which are at least in the same order of magnitude. Thus, the possibility of temperature expansion effects and frequency shifts resulting in the fringe shifts observed cannot be eliminated.

Other possibilities include those effects which can enter in if the incidence was not truly normal and if the degree of normality varied from run to run. It is possible that such variations could take place since the interferometer was aligned prior to each run. It is more difficult to reason that the normality might vary during a run when no changes in alignment are made. However, it is plausible that temperature changes and vibrations could cause alignment shifts during a run.

In the worst case we might expect the interferometer to be misaligned in pitch angle by about 20 arc sec. Such a misalignment has a negligible effect on the normal incidence phase.

If the interferometer is slightly off the normal position, the straight-through and twice reflected beams have a slight separation. It is unlikely that true normal incidence was achieved at any time due to slight misalignments, environmental effects, and non-perfect surface qualities such as flatness and parallelism. The interference must then take place between two rays originating from slightly different positions in the laser beam cross section. The light is then required to be coherent to produce interference in a non-focused beam.

Coherency is a relative term and not even the laser is perfectly coherent. One way of describing perfect coherence is to state that two rays are coherent, if there exists a fixed phase relationship, independent of time, between any two spatially separated points in the two rays. The degree to which this phase relationship is dependent on time is a measure of the incoherency of the rays. Thus, it may well be that the phase relationship of the laser rays shifts with time and these shifts account for the interference phase shifts observed. This aspect has not been investigated quantitatively to determine the possible order of magnitude of this effect.

Calibration Results. The results of the five calibrations runs in which fringe count versus angle data were taken are tabulated in Table II. The actual fringe count values were not integer values, but were values close to the integer values listed. The fringe count could not be set exactly at integers because of the non-integral normal incidence phase, and because it is almost impossible to stop the interferometer rotation at exactly the same phase each time.

In order to make any conclusions about the results obtained it was first necessary to reduce the data to some common base. This was accomplished by correcting each angle reading to an integer fringe count by taking the difference between the integer fringe count and the actual fringe count, and dividing by the sensitivity,  $\frac{dq}{d\theta}$ . The sensitivity used was that value predicted by theory since the sensitivities were not measured at each of the calibration points. The validity of this approach is based on the fact that the actual measured sensitivities agreed very well with theory, and did not seem to be affected by the phase shifts observed at normal incidence.

TABLE II

Calibration Results

Fringe Count	Theoretical			Experimental Runs				
	Deg.	Min.	Sec.	A-1	A-2	A-3	A-4	A-5
10	1	33	57.4	+16.9	+35.5	+ 0.8	-17.7	+22.8
20	2	12	53.2	+ 8.5	+37.7	+ 3.6	-15.7	+11.6
50	3	30	9.6	+ 3.0	+15.4	+ 3.3	- 7.3	+ 9.8
100	4	57	20.0	-----	+26.9	+ 9.2	+ 1.0	+12.2
150	6	4	18.3	- 3.2	+25.9	+ 1.1	- 2.1	+12.1
200	7	0	50.1	- 4.9	+21.2	+ 0.9	+ 0.6	+10.1
250	7	50	41.0	- 2.7	+20.0	+ 2.2	+ 1.8	+11.7
300	8	35	50.1	- 6.2	+27.8	+ 5.3	- 2.2	+14.0
350	9	17	23.6	- 5.5	+17.5	+ 3.1	+ 3.1	+16.2
400	9	55	67.4	- 7.8	+19.7	+ 0.4	+ 0.5	+11.2
450	10	32	32.7	- 4.7	+19.3	+ 4.1	+ 0.7	+13.0
500	11	6	62.2	- 4.0	+17.7	- 0.8	- 1.7	+ 9.0
600	12	11	18.5	- 5.4	+19.3	+ 3.7	+ 1.2	+ 9.5
700	13	10	33.7	- 3.6	+17.7	+ 3.3	+ 0.0	+ 7.5
800	14	5	51.3	- 5.1	+16.8	+ 3.0	- 1.0	+ 8.8
900	14	57	55.2	- 11.5	+15.5	+ 6.0	- 4.0	+ 8.3
1000	15	47	17.6	-10.4	+13.9	+ 3.7	- 0.4	+ 7.3
1100	16	34	22.6	- 7.3	+15.9	+ 5.8	- 0.1	+ 8.2
1200	17	19	29.0	- 6.4	+16.6	+ 3.6	+ 2.2	+ 9.2
1300	18	2	51.6	-----	+12.7	+ 6.1	+ 1.2	+ 5.5
1400	18	44	42.8	- 9.0	+13.5	+ 3.2	- 1.8	+ 7.7
1500	19	25	12.3	-----	-10.3	+13.1	- 4.8	+ 4.9
1600	20	4	28.4	-----	- 8.1	+ 4.0	- 0.3	+ 8.2

In Table II the theoretically predicted values are shown in degrees, arc min. and arc sec. Only the differences in arc sec. between the measured and predicted values are tabulated.

Best agreement is obtained with run A-4 except at low fringe count and low angle. All runs except A-3 indicate poor agreement at low angles. Whereas run A-4 deviates from the theoretical values both positively and negatively, the other runs are fairly uniformly positive or negative. Not counting several of the initial readings which are blocked off in Table II, average values of the deviation of experimental results from theoretical values were computed for each run. The results were that A-1 was on the average 6 arc sec. lower than theoretical, A-2 was 16 arc sec. higher, A-3 was 3 arc sec. higher, A-4 was 0.3 arc sec. lower and A-5 was 10 arc sec. higher.

The fact that most of the runs were fairly uniformly low or high indicates the possibility of a constant error. One possible source of this error is in the procedure where the table is set at the normal position by stopping the table rotation at the occurrence of the spike in the normal incidence trace. The zero reading is taken at this point. It was estimated by observing the width of the spike that the interferometer could be set to the normal position to within about 20 arc sec. The range of the average deviations calculated above turns out to be 22 arc sec. Thus, errors in normal alignment may well account for the average deviations of the results.

The larger deviations at low angles can possibly be accounted for by the fact that the sensitivity in this range is very low, and an error in the estimation of the fraction of a fringe at which the rotation has been stopped will introduce larger errors at low angles than at high angles.

The results tabulated in Table III were obtained by subtracting the average deviations of runs A-1, A-2, A-3 and A-5 from each of the measured values. These values show a better distribution of deviations. The magnitude of these deviations are still too large to be accounted for by the estimated experimental accuracy. Experimental procedure errors alone should give agreement to less than one arc sec.

One possible and probable cause of these errors is the normal incidence fringe shift already discussed. The fringe shift is of course present at all angles but was specifically observed at normal incidence. Such fringe shifts occurring during a run can account for several arc sec. of error. For example, a fringe shift of  $\frac{\pi}{2}$  at  $20^\circ$  will result in a 6 arc sec. error. At lower angles a corresponding shift will cause greater errors.

Sensitivity Results. Sensitivity data were taken at every  $5^\circ$  of angle from  $5^\circ$  to  $45^\circ$ . Only one complete sensitivity run was accomplished although the sensitivity was checked several times at various angles. These several checks agreed with the results tabulated in Table IV.

The sensitivity measurements are actually measurements of the average sensitivities over a small angular range. The experimental results were obtained by setting the interferometer at each of the angular positions listed and then rotating the interferometer for approximately five fringe counts for angles  $5^\circ$ ,  $10^\circ$ , and  $15^\circ$  and ten fringe counts for the remaining angles. The angular position of the interferometer was then read. The sensitivity was then calculated for comparative purposes.

TABLE III								
Corrected Calibration Results								
Fringe Count	Theoretical			Experimental Runs				
	Deg.	Min	Sec.	A-1	A-2	A-3	A-4	A-5
10	1	33	57.4	+22.9	+19.5	-3.2	-17.7	+12.8
20	2	12	53.2	+14.5	+21.7	-0.4	-15.7	+ 1.6
50	3	30	9.6	+ 9.0	- 0.6	-0.7	- 7.3	- 0.2
100	4	57	20.0	-----	+10.9	+5.2	+ 1.0	+ 2.2
150	6	4	18.3	+ 2.8	+ 9.9	-2.9	- 2.1	+ 2.1
200	7	0	50.1	+ 1.1	+ 5.2	-3.1	+ 0.6	+ 0.1
250	7	50	41.0	+ 3.3	+ 4.0	-1.8	+ 1.8	+ 1.7
300	8	35	50.1	- 0.2	+11.8	+1.3	- 2.2	+ 4.0
350	9	17	23.6	+ 0.5	+ 1.5	-0.9	+ 3.1	+ 6.2
400	9	55	67.4	- 1.8	+ 3.7	-3.6	+ 0.5	+ 1.2
450	10	32	32.7	+ 1.3	+ 3.3	+0.1	+ 0.7	+ 3.0
500	11	6	62.2	+ 2.0	+ 1.7	-4.8	- 1.7	- 1.0
600	12	11	18.5	+ 0.6	+ 3.3	-0.3	+ 1.2	- 0.5
700	13	10	33.7	+ 2.4	+ 1.7	-0.7	+ 0.0	- 2.5
800	14	5	51.3	+ 0.9	+ 0.8	-1.0	- 1.0	- 1.2
900	14	57	55.2	- 5.5	- 0.5	+2.0	- 4.0	- 1.7
1000	15	47	17.6	- 4.4	- 2.1	-0.3	- 0.4	- 2.7
1100	16	34	22.6	- 1.3	- 0.1	+1.8	- 0.1	- 1.8
1200	17	19	29.0	- 0.4	+ 0.6	-0.4	+ 2.2	- 0.8
1300	18	2	51.6	-----	- 3.3	+2.1	+ 1.2	- 4.5
1400	18	44	42.8	- 3.0	- 2.5	-0.8	- 1.8	- 2.3
1500	19	25	12.3	-----	-26.3	+9.1	- 4.8	- 5.1
1600	20	4	28.4	-----	-24.1	+0.0	- 0.3	- 1.8

TABLE IV				
Sensitivity Results				
Angle $\theta$	Theoretical Sensitivity		Experimental Sensitivity	
	$\frac{\text{fringes}}{\text{arc sec.}}$	$\frac{\text{arc sec.}}{\text{fringe}}$	$\frac{\text{fringes}}{\text{arc sec.}}$	$\frac{\text{arc sec.}}{\text{fringe}}$
5°	0.01135	88.1	0.01125	88.9
10°	0.02236	44.7	0.0225	44.4
15°	0.0331	30.2	0.0328	30.5
20°	0.0431	23.2	0.0428	23.35
25°	0.0524	19.1	0.051	19.6
30°	0.0599	16.7	0.0584	17.13
35°	0.0665	15.05	0.067	14.93
40°	0.0712	14.04	0.0704	14.2
45°	0.0745	13.43	0.0722	13.85

All measured values agree quite well to within the estimated accuracy of the experiment except for perhaps the 5° value. However, at small angles the probable error is greater due to the fact that a given error in estimating the fringe count from the strip chart recording in this range will correspond to a greater angular error.

## V. Summary of Results and Conclusions

The availability of a monochromatic, coherent and directional light beam such as the laser beam has opened up interesting possibilities in the utilization of the interference effect for sensing angular position. The coherence of the light eliminates the necessity of devising closed light path loops to split and rejoin the two interfering rays. A simple angle sensing device can consist of a thick optical flat with reflective surfaces and a light sensor to detect the interference intensity variations with angle. Such a device can be made quite small and can be easily mounted on an inertial platform undergoing acceleration tests.

Various theoretical aspects, such as the variation of fringe count, sensitivity, beam separation and interference intensity with angle, have been investigated in Section II. Other theoretical aspects touched on include reflection and transmission, maximum range, direction sensing and combined pitch and yaw effects.

Design calculations were then made for a prospective angle sensing interferometer. These calculations exposed no serious problems which might affect the feasibility of the system and showed that an angle sensing system could be designed meeting all requirements for the inertial platform attitude monitoring application.

In particular, an interferometer of solid fused quartz, 3 cm. thick (Figure 15) was designed to give a sensitivity of 0.175 fringes per arc sec. or 5.72 arc sec. per fringe with an estimated accuracy of  $\pm 0.285$  arc sec. The angular range of measurement can be made to far exceed the required range of  $\pm 5$  arc min. Table I gives a complete tabulation of the results of the design calculations.

Also considered briefly was the problem of direction sensing. It was shown that the relative phase between two interference fields could be utilized to sense direction. If one of these two fields is initially  $\frac{\pi}{2}$  out of phase with the other, rotation reversal results in a phase shift to  $-\frac{\pi}{2}$  or  $\frac{3\pi}{2}$ . Based on the above results, it is concluded that the interferometer angle sensing device is theoretically feasible.

The experimental phase of this study consisted of calibration and sensitivity tests on an interferometer consisting of a fused quartz optical flat of roughly 2 inch diameter and 1/2 inch thickness. The two surfaces of this optical flat were flat to 1/20 th of a wavelength and parallel to less than one arc sec. The laser beam was collimated down to less than 20 arc sec.

The interference pattern was a quite uniform full field pattern at normal incidence. At larger angles a few irregular shaped fringes began to appear indicating a requirement for flatter surfaces and higher beam collimation. However, good signal strength was obtained at these angles. The beam collimation can probably be reduced to less than 10 arc sec. and flats to within 1/50 or 1/100 of a wavelength and less than 0.5 arc sec. can undoubtedly be obtained on special order.

The basic calibration results indicated the presence of constant plus random errors. The range of the constant errors was 22 arc sec. which can be accounted for as normal incidence alignment errors. The calibrations results corrected for possible constant normal alignment errors, show higher deviations from the theoretical results than can be credited to experimental technique errors. The most probable cause is the observed phase shifts. The magnitudes of

these phase shifts were large enough to account for the deviations.

Possible causes of these phase shifts are the following:

1. Temperature effects on the thickness of the optical flat  
( cannot alone account for the magnitude of the phase shifts).
2. Frequency shifts in the laser oscillation  
( this effect may be the primary cause).
3. Coherence shifts or phase shifts in the laser beam between  
two separate rays which interfere in the interferometer  
( this effect may also be a primary cause).

Sensitivity results showed agreement with the predicted values to within the experimental accuracy limitations of the equipment.

The operation of the angle sensing interferometer was highly satisfactory from the standpoint of interference pattern, signal, and sensitivity. The phase shift effect must of course be further investigated in order to determine the source of these shifts and their effect on the feasibility of achieving desired accuracies with the system.

It is also concluded that higher accuracy experimental techniques are required especially in the normal incidence alignment procedure. Other than the unknown consequences of the phase shift effect, the interferometer angle sensing device has not shown any effect which might prove the system infeasible.

V. Recommendations for Continued Research

One of the results of any theoretical and experimental investigation is the confrontation of the researcher with new or additional questions which require answers. In the case of this investigation some of these questions have been discussed briefly in the preceding text. The purpose of this section is to present several of these questions in the form of topics for additional research. Listed below are four such topics.

1. Investigation of the effects of the atmosphere on the transmission of a laser beam parallel and in close proximity to the earth ( in particular along the Holloman AFB sled track).
2. Investigation of the cause of the phase shift observed at normal incidence and of methods of compensation of this effect.
3. Investigation of the effect of the transmission of a laser beam through the atmosphere on the coherence of the light.
4. Construction and testing of the theoretical interferometer angle sensing design presented in this paper for sensitivity and accuracy.

Bibliography

1. Born, M., and E. Wolf. Principles of Optics. New York: Pergamon Press, 1959.
2. Delange, O. E. "Long Distance Light Propagation." Proc. IEEE, 50, 1361 (1962).
3. Handbook of Geophysics (United States Air Force). New York: The Macmillan Co., 1960.
4. Heavens, O. S. Optical Properties of Thin Solid Films. London: Butterworths Scientific Publications, 1955.
5. Jenkins, F. A., and H. E. White. Fundamentals of Optics (Third Edition). New York: McGraw-Hill Co., Inc., 1957.
6. Lengyel, B. A. Lasers: Generation of Light by Stimulation Emission. New York: John Wiley and Sons, Inc., 1962.
7. Stickley, C. M. Applications, notes from a seminar-course on Lasers/Masers, New York, N. Y., (December 1963).

## Appendix A

Derivation of Refractosyn Equations

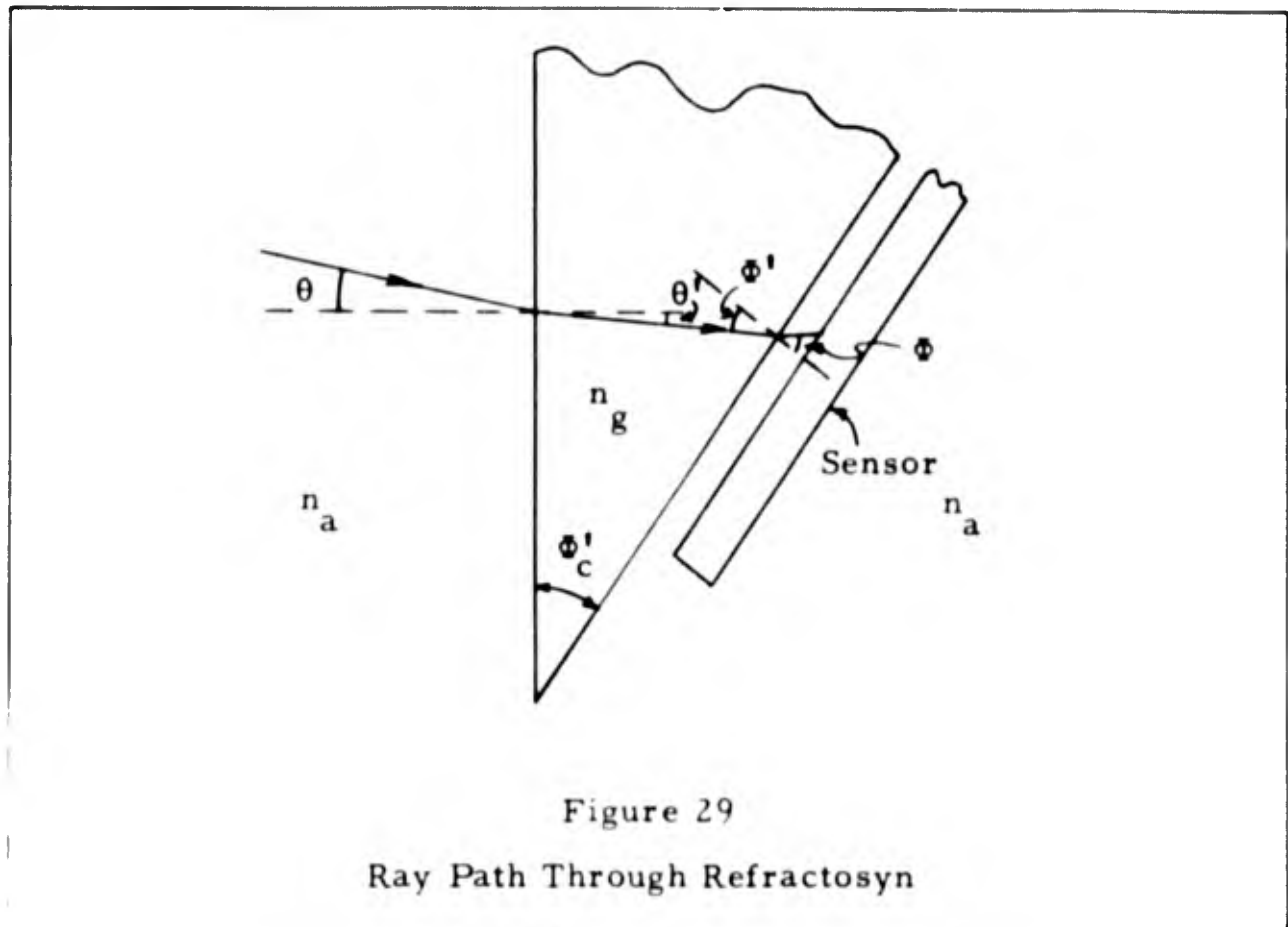
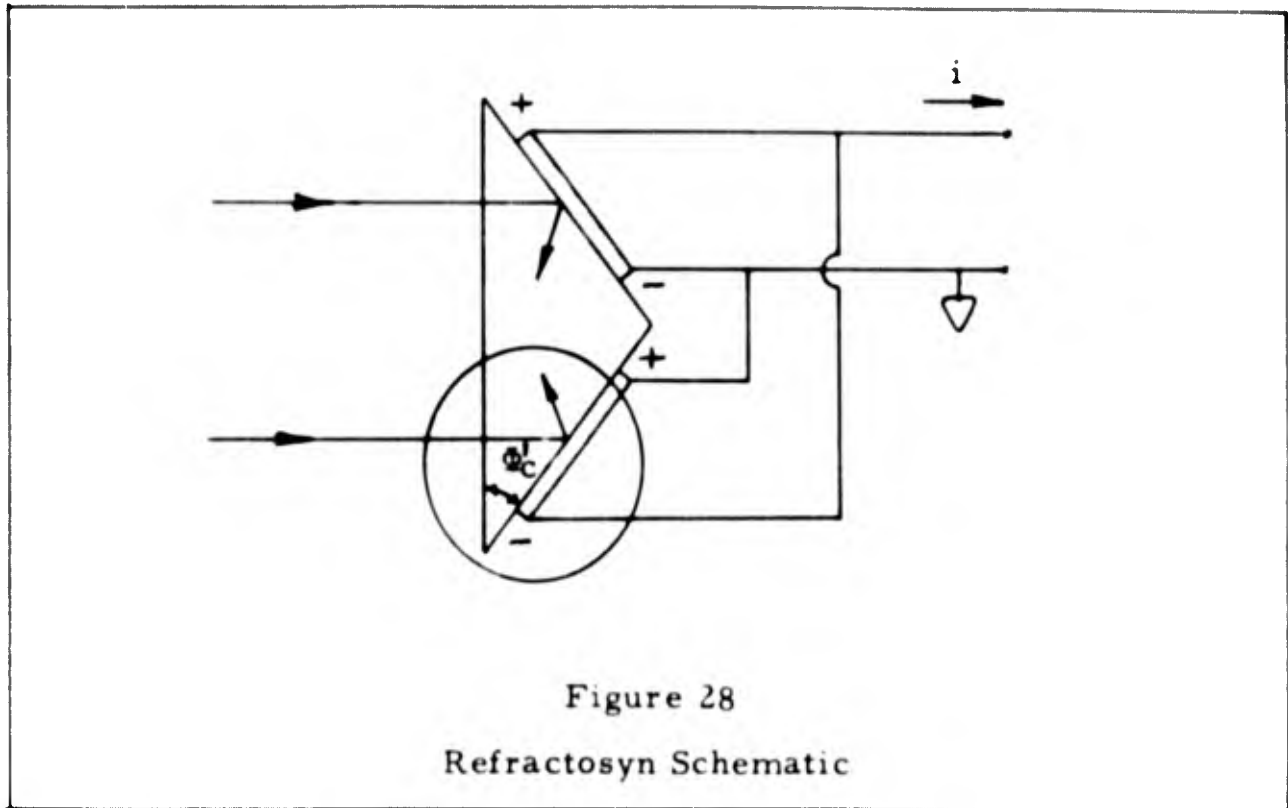
The Refractosyn sensor consists of two photocells and an isosceles prism cut at the critical angle for a specific wavelength. At null position when incident light rays are normal to the base of the isosceles prism the rays are totally reflected and the current at the output is essentially zero. Rotation of the Refractosyn to the left or right about an axis normal to the triangular sides of the prism causes abrupt refraction of light onto one or the other two opposing photocells.

A schematic representation of the Refractosyn angle sensor oriented at the null position is shown in Figure 28. Figure 29 shows an enlarged view of the area circled in Figure 28 with the sensor oriented slightly off the null position and the refraction angle exaggerated.

Neglecting absorption and reflection losses, as a beam passes through the prism the effective intensity falling on a photocell will be reduced in proportion to the projected area of the sensor normal to the incident beam. Mathematically the above statement becomes

$$I = I_0 \cos \phi \quad (43)$$

where  $I_0$  is the intensity incident on the prism and  $\phi$  is the angle of incidence with respect to the base of the isosceles prism. The angle  $\phi$  is related to the angle  $\theta$  by the law of refraction applied to the two interfaces. These relationships are



$$\left. \begin{aligned} n_s \sin \phi &= n_g \sin \phi' \\ \phi' &= \phi'_c - \theta' \\ n_g \sin \theta' &= n_a \sin \theta \end{aligned} \right\} \quad (44)$$

Using Equations (44) and assuming  $n_a$  (index of refraction for air) equals unity, the following expression can be derived.

$$\sin \phi = \sin \phi'_c \sqrt{n_g^2 - \sin^2 \theta} - \cos \phi'_c \sin \theta \quad (45)$$

Since  $\cos^2 \phi = 1 - \sin^2 \phi$ ,

$$\begin{aligned} \cos^2 \phi &= 1 - \sin^2 \phi'_c (n_g^2 - \sin^2 \theta) \\ &\quad - \cos^2 \phi'_c \sin^2 \theta + \sin 2\phi'_c \sin \theta \sqrt{n_g^2 - \sin^2 \theta} \end{aligned} \quad (46)$$

Reordering yields,

$$\begin{aligned} \cos^2 \phi &= (1 - n_g^2 \sin^2 \phi'_c) + \sin^2 \theta (\sin^2 \phi'_c - \cos^2 \phi'_c) \\ &\quad + \sin 2\phi'_c \sin \theta \sqrt{n_g^2 - \sin^2 \theta} \end{aligned} \quad (47)$$

Referring to the first of Equations (44) when  $\phi = 90^\circ$ ,  $\phi' = \phi'_c$ . Thus,

$$\sin \phi'_c = \frac{1}{n_g} \quad (48)$$

Using Equation (48) and trigonometric identities, the following relationships result.

$$\left. \begin{aligned}
 1 - n_g^2 \sin^2 \phi_c' &= 0 \\
 \sin^2 \phi_c' - \cos^2 \phi_c' &= \frac{2 - n_g^2}{n_g^2} \\
 \sin 2\phi_c' &= \frac{2}{n_g^2} \sqrt{n_g^2 - 1}
 \end{aligned} \right\} \quad (49)$$

Using Equations (49), Equation (47) becomes

$$\cos^2 \phi = \frac{2 - n_g^2}{n_g^2} \sin^2 \theta + \frac{2}{n_g^2} \sqrt{n_g^2 - 1} \sin \theta \sqrt{n_g^2 - \sin^2 \theta} \quad (50)$$

By use of Equation (50), the expression for I becomes

$$I = I_o \left[ A \sin^2 \theta + B \sin \theta \sqrt{n_g^2 - \sin^2 \theta} \right]^{\frac{1}{2}} \quad (51)$$

where

$$A = \frac{2 - n_g^2}{n_g^2}$$

and

$$B = \frac{2}{n_g^2} \sqrt{n_g^2 - 1}$$

The derivative,  $\frac{dI}{d\theta}$ , is

$$\frac{dI}{d\theta} = \frac{I_o \cos \theta \left[ 2A \sin \theta + \frac{B \sin^2 \theta}{\sqrt{n_g^2 - \sin^2 \theta}} + B \sqrt{n_g^2 - \sin^2 \theta} \right]}{2\sqrt{\sin \theta} \left[ A \sin \theta + B \sqrt{n_g^2 - \sin^2 \theta} \right]^{\frac{1}{2}}} \quad (52)$$

At this point we have two complex expressions, Equations (51) and (52) for  $I$  and  $\frac{dI}{d\theta}$ , respectively. However, several simplifying approximations can now be introduced.

For various glasses,  $n_g$  is on the order of 1.5. Since the angular range limits are  $\pm 5$  arc min., we can state that  $n_g^2$  will be very much greater than  $\sin^2\theta$ . For example, at 5 arc min. the ratio  $n_g^2 / \sin^2\theta$  is equal to about  $10^6$ . Thus Equations (51) and (52) can be written

$$I \cong I_o (B n_g \sin \theta)^{\frac{1}{2}} \left( 1 + \frac{A}{B n_g} \sin \theta \right)^{\frac{1}{2}} \quad (53)$$

and

$$\frac{dI}{d\theta} \cong \frac{I_o \cos \theta}{2} \left[ \frac{B n_g}{\sin \theta} \right]^{\frac{1}{2}} \frac{\left[ 1 + \frac{2A}{B n_g} \sin \theta + \frac{\sin^2 \theta}{n_g^2} \right]}{\left[ 1 + \frac{A}{B n_g} \sin \theta \right]^{\frac{1}{2}}} \quad (54)$$

In Equation (54) we observe that  $1 \gg \sin^2 \theta / n_g^2$ . The coefficient  $2A/B n_g$  is on the order of -0.15 for  $n_g$  equal to 1.5. Thus, for small  $\theta$ , we can say that  $1 \gg \frac{2A}{B n_g} \sin \theta > \frac{A}{B n_g} \sin \theta$ . At 5 arc min. the ratio of 1 to  $(2A/B n_g) \sin \theta$  is about  $-4.5 \times 10^3$ . Equations (53) and (54) can thus be written,

$$I \cong I_o (B n_g \sin \theta)^{\frac{1}{2}} \quad (55)$$

and

$$\frac{dI}{d\theta} \cong \frac{I_o \cos \theta}{2} \left[ \frac{B n_g}{\sin \theta} \right]^{\frac{1}{2}} \quad (56)$$

## Appendix B

## Derivation of Interferometer Equations

Consider a Fabry-Perot type interferometer consisting of two plane-parallel reflective surfaces formed by grinding, polishing, and coating two surfaces on a transparent material such as glass. Light rays on passing through such an interferometer will be split into many parallel reflected and transmitted rays whose intensities decrease with each subsequent reflection. If a transmitted and twice reflected ray are brought together by a lens, they will interfere with each other due to the fact that the reflected ray has traveled a greater optical path than the transmitted ray.

Using a coherent light beam eliminates the need for a focusing lens to bring the rays together. Figure 30 shows the geometric paths of two selected rays incident on the interferometer. Ray A'' which is separated from ray A' by the distance  $s$  is coincident with ray B' which is also a distance  $s$  from ray A'. Thus ray B' and A'' will interfere if ray A and B are coherent with respect to each other as they are for laser light. Of course the cross-sectional dimension of the light beam must be larger than  $s$  so that there exists a ray, B, in the beam a distance  $s$  from ray A.

However, whether a lens is utilized or not the subsequent equations will apply in both cases. This can be demonstrated by referring to Figure 30. If no lens were used the two rays would join at point O and the difference in optical path,  $\Delta$ , is the difference

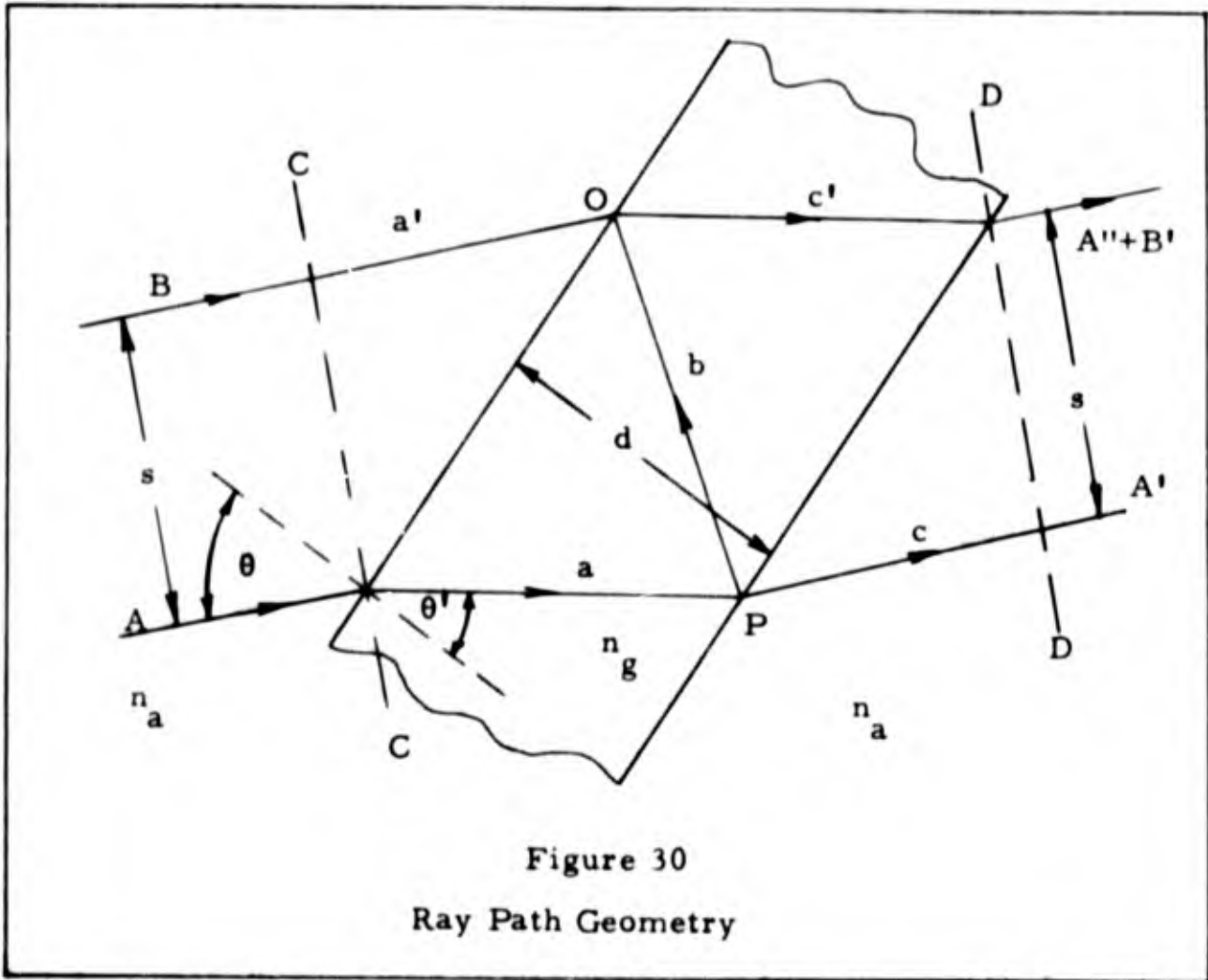


Figure 30  
Ray Path Geometry

in the paths from the wavefront CC to point 0. This is given by

$$\Delta_1 = n_g (a + b) - n_a a' \quad (57)$$

Since  $a = b$ ,

$$\Delta_1 = 2n_g a - n_a a' \quad (58)$$

For the case where a lens is used the rays split at point P and travel different paths up to the wavefront DD. Subsequently they traverse identical optical paths. Thus,

$$\Delta_2 = n_g (b + c') - n_a c \quad (59)$$

Here again,  $a = b = c'$  and by inspection of the geometry it is obvious that  $c = a'$ . Thus,

$$\Delta_2 = 2n_g a - n_a a' = \Delta_1 \quad (60)$$

Referring to Figure 30, the following relationship can be noted.

$$a' = 2a \sin \theta' \sin \theta \quad (61)$$

Thus,

$$\Delta = 2a (n_g - n_a \sin \theta' \sin \theta) \quad (62)$$

Since

$$a = d / \cos \theta' \quad (63)$$

and

$$n_a \sin \theta = n_g \sin \theta' \quad (64)$$

Equation (62) becomes

$$\Delta = \frac{2d}{n_g \cos \theta'} (n_g^2 - n_a^2 \sin^2 \theta) \quad (65)$$

From Equation (64) it can be shown that

$$n_g \cos \theta' = \sqrt{n_g^2 - n_a^2 \sin^2 \theta} \quad (66)$$

Thus, Equation (65) can be written,

$$\Delta = 2d \sqrt{n_g^2 - n_a^2 \sin^2 \theta} \quad (67)$$

The optical path difference in wavelengths is

$$m = \frac{\Delta}{\lambda_o} = \frac{2d}{\lambda_o} \sqrt{n_g^2 - n_a^2 \sin^2 \theta} \quad (68)$$

If  $m$  is an integer, the intensity will be maximum. If  $m$  is an integer plus one-half, the intensity is a minimum.

The sensitivity of this interferometer is related to the rate of change of  $m$  with respect to  $\theta$ .

$$\frac{dm}{d\theta} = - \frac{dn_a^2 \sin 2\theta}{\lambda_o} \left[ n_g^2 - n_a^2 \sin^2 \theta \right]^{-\frac{1}{2}} \quad (69)$$

When  $\left| \frac{dm}{d\theta} \right|$  is maximum the sensitivity is maximum. Since  $\left| \frac{dm}{d\theta} \right|$  is always positive, and is equal to zero at  $\theta = 0^\circ$ , and  $\theta = 90^\circ$ , and exceeds zero for  $\theta$  between  $0^\circ$  and  $90^\circ$ , there must exist at least one maximum for  $0^\circ < \theta < 90^\circ$ . If there exists only one solution to  $\frac{d^2m}{d\theta^2} = 0$  for  $0^\circ < \theta < 90^\circ$ , then that solution must correspond to a maximum. Thus,

$$\frac{d^2r_1}{d\theta^2} = \frac{-dn_a^2}{\lambda_o} \left[ \frac{\cos 2\theta_m (n_g^2 - n_a^2 \sin^2 \theta_m) + n_a^2 \sin^2 \theta_m \cos^2 \theta_m}{(n_g^2 - n_a^2 \sin^2 \theta_m)^{3/2}} \right] = 0 \quad (70)$$

Since,

$$\frac{dn_a^2}{\lambda} > 0$$

and

$$n_g^2 - n_a^2 \sin^2 \theta_m > 0$$

it follows from Equation (70) that,

$$(n_g^2 - n_a^2 \sin^2 \theta_m) \cos 2\theta_m + n_a^2 \sin^2 \theta_m \cos^2 \theta_m = 0 \quad (71)$$

By use of appropriate trigonometric identities Equation (71) can be written

$$\sin^4 \theta_m - 2 \left[ \frac{n_g}{n_a} \right]^2 \sin^2 \theta_m = - \left[ \frac{n_g}{n_a} \right]^2 \quad (72)$$

Completing the square of the left side of the equation gives,

$$\left[ \sin^2 \theta_m - \left( \frac{n_g}{n_a} \right)^2 \right]^2 = \left( \frac{n_g}{n_a} \right)^2 \left[ \left( \frac{n_g}{n_a} \right)^2 - 1 \right] \quad (73)$$

Taking the square root of both sides,

$$\sin^2 \theta_m - \left( \frac{n_g}{n_a} \right)^2 = \pm \frac{n_g}{n_a} \sqrt{\left( \frac{n_g}{n_a} \right)^2 - 1} \quad (74)$$

Since  $\left(\frac{n_g}{n_a}\right)^2 > \sin^2 \theta_m$ , the negative sign must prevail. Solving for  $\sin \theta_m$ ,

$$\sin \theta_m = \left[ \left(\frac{n_g}{n_a}\right)^2 - \frac{n_g}{n_a} \sqrt{\left(\frac{n_g}{n_a}\right)^2 - 1} \right]^{\frac{1}{2}} \quad (75)$$

Since this is a unique solution in the range  $0^\circ < \theta < 90^\circ$ , it must correspond to a maximum as assumed.

The separation,  $s$ , between a straight-through ray and a twice reflected ray is of interest since it determines the amount of beam overlap. Referring to Figure 30,

$$s = 2d \tan \theta' \cos \theta \quad (76)$$

By use of the proper relationships between  $\theta'$  and  $\theta$ , Equation (76) becomes,

$$s = n_a d \sin 2\theta \left[ n_g^2 - n_a^2 \sin^2 \theta \right]^{-\frac{1}{2}} \quad (77)$$

Since Equations (69) and (77) are of the same form, maximum separation occurs at  $\theta_m$  given by Equation (75).

## Appendix C

## Derivation of Interference Intensity Equations

Interference involves the vector addition of the electric fields of two or more coherent waves which vibrate with the same polarization and which have been made to coincide at some point or points in space. Consider therefore the addition of  $n$  waves of the same frequency whose electric fields are given by

$$\left. \begin{aligned} e_1 &= E_1 \sin(\omega t + a_1) \\ e_2 &= E_2 \sin(\omega t + a_2) \\ &\vdots \\ e_n &= E_n \sin(\omega t + a_n) \end{aligned} \right\} \quad (78)$$

where  $n$  is a finite integer. Using the expression for the sine of the sum of two angles, the sum of  $e_i$  is

$$e = \sum_{i=1}^n E_i (\sin \omega t \cos a_i + \cos \omega t \sin a_i) \quad (79)$$

This can be rewritten as

$$e = \left[ \sin \omega t \sum_{i=1}^n E_i \cos a_i \right] + \left[ \cos \omega t \sum_{i=1}^n E_i \sin a_i \right] \quad (80)$$

Since  $E_i$  and  $a_i$  are constants we can set

$$\sum_{i=1}^n E_i \cos a_i = R \cos \theta \quad (81)$$

and

$$\sum_{i=1}^n E_i \sin a_i = R \sin \theta \quad (82)$$

provided constants  $R$  and  $\theta$  can be found which satisfy Equations (81) and (82). Squaring and adding Equations (81) and (82), we have

$$R^2 \sin^2 \theta + R^2 \cos^2 \theta = \left[ \sum_{i=1}^n E_i \sin a_i \right]^2 + \left[ \sum_{i=1}^n E_i \cos a_i \right]^2 \quad (83)$$

or

$$R^2 = \left[ \sum_{i=1}^n E_i \sin a_i \right]^2 + \left[ \sum_{i=1}^n E_i \cos a_i \right]^2 \quad (84)$$

Dividing Equation (82) by Equation (81) yields

$$\tan \theta = \frac{\sum_{i=1}^n E_i \sin a_i}{\sum_{i=1}^n E_i \cos a_i} \quad (85)$$

Equations (84) and (85) show that values of  $R$  and  $\theta$  exist which satisfy Equations (81) and (82). Equation (80) may now be rewritten

$$e = R \sin \theta \cos \omega t + R \cos \theta \sin \omega t \quad (86)$$

This equation has the form of the sine of the sum of two angles.

Therefore,

$$e = R \sin (\omega t + \theta) \quad (87)$$

The intensity of the resulting wave is proportional to the square of the amplitude

$$I = k R^2 \quad (88)$$

Using Equation (84), Equation (88) can be written

$$I = \left[ \sum_{i=1}^n \sqrt{k} E_i \sin a_i \right]^2 + \left[ \sum_{i=1}^n \sqrt{k} E_i \cos a_i \right]^2 \quad (89)$$

It can now be observed that  $\sqrt{k} E_i$  is the square root of the intensities of the individual waves. Thus,

$$I = \left[ \sum_{i=1}^n \sqrt{I_i} \sin a_i \right]^2 + \left[ \sum_{i=1}^n \sqrt{I_i} \cos a_i \right]^2 \quad (90)$$

For  $n = 2$ ,

$$I \Big|_{n=2} = I_1 + I_2 + 2\sqrt{I_1 I_2} \cos(a_1 - a_2) \quad (91)$$

For  $n = 3$ ,

$$I \Big|_{n=3} = I_1 + I_2 + I_3 + 2\sqrt{I_1 I_2} \cos(a_1 - a_2) \\ + 2\sqrt{I_1 I_3} \cos(a_1 - a_3) + 2\sqrt{I_2 I_3} \cos(a_2 - a_3) \quad (92)$$

In general, it can be shown that

$$I = \sum_{i=1}^n I_i + 2 \sum_{i=1}^{n-1} \sum_{p=i+1}^n \sqrt{I_i I_p} \cos(a_i - a_p) \quad (93)$$

Vita

Capt. Henry A. Olender, son of John and Anna Olender, was born on [REDACTED] in [REDACTED]. He received a Bachelor of Science degree in Aeronautical Engineering from New York University in 1957. At N. Y. U. he completed the Air Force Reserve Officer's Training Corps program and was the recipient of the Distinguished Military Graduate Award. On graduation, he was commissioned a Second Lieutenant in the United States Air Force.

Prior to entering active service in the Air Force, he was employed by North American Aviation in Los Angeles where he worked on aerodynamic problems and participated in the preparation of the F-100 D Performance Report.

Capt. Olender entered active duty in the Air Force in January 1958. In the Air Force, he has worked in the nuclear weapon effects area and participated in the planning and management of engineering analysis programs related to nuclear weapon effects on re-entry and space vehicles. Currently he is assigned to the Office of Research Analyses, OAR, at Holloman A. F. B., New Mexico where he participates in operations and systems analyses activities.

From June 1961 to December 1962 he attended the Air Force Institute of Technology at Wright-Patterson A. F. B., Ohio for graduate course work in Electrical Engineering. At A. F. I. T. he was a member of the Eta Kappa Nu honorary society of Electrical Engineers.

Capt. Olender's current permanent address is

[REDACTED]  
[REDACTED].

Pat Friel